Faculty of Engineering, Science and Mathematics
School of Engineering Sciences

Micromagnetic simulations of magnetic exchange spring systems

A thesis submitted in partial satisfaction
of the requirements for the degree of
Doctor of Philosophy

Jürgen P. Zimmermann

Computational Engineering and Design Group
School of Engineering Sciences
University of Southampton
United Kingdom

Supervisors: Dr. Hans Fangohr, Prof. Peter A. J. de Groot

30th November 2007

UNIVERSITY OF SOUTHAMPTON

ABSTRACT

FACULTY OF ENGINEERING, SCIENCE AND MATHEMATICS
SCHOOL OF ENGINEERING SCIENCES

Doctor of Philosophy

MICROMAGNETIC SIMULATIONS OF MAGNETIC EXCHANGE SPRING SYSTEMS

Jürgen Peter Zimmermann

Magnetic exchange spring systems are multi-layers or composites of magnetically hard and soft materials that are exchange-coupled across their interfaces. In recent years, research into exchange spring systems has flourished, with potential for application in high-performance permanent magnets, GMR spin devices, magnetic MEMS technology, and in magnetic data storage.

We investigate the magnetic properties of MBE grown superlattices with alternating layers of magnetically hard rare earth-iron ($DyFe_2$, $ErFe_2$) and soft yttrium-iron (YFe_2) compounds. They are ideal model systems to study exchange spring phenomena. We develop numerical models of the investigated systems and apply micromagnetic simulations. The simulation code OOMMF is extended and used to solve Landau-Lifshitz-Gilbert and Brown's equations. This allows us to determine the microscopic configuration of the magnetisation that is not directly accessible by experiment.

Magnetic field-sweep measurements of a multilayered $DyFe_2/YFe_2$ system show an unexpected triple switching of the magnetically hard $DyFe_2$ layers. The magnetisation of the hard magnetic layers reverse before the soft magnetic layers. We reproduce the experimental hysteresis loops of the net and compound-specific magnetisation by means of simulations and explain the switching behaviour.

Using similar numerical methods, we interpret experimental data on $ErFe_2/YFe_2$ multilayers. At sufficiently high fields, applied perpendicular to the multilayer film plane, the energy is minimised by a multilayer spin flop. This is a particular spin configuration where the magnetisation aligns with a direction perpendicular to the applied field.

Taking the preceding findings further, we investigate multilayers of $ErFe_2/YFe_2/DyFe_2/YFe_2$. We gain insight in the complex spin configurations in systems of different magnetically hard materials, with a pre-strung domain wall in the soft YFe_2 layers. Varying the thickness of the YFe_2 layers, we study the changing mutual interference of the switching patterns in the $ErFe_2$ and $DyFe_2$ layers.

Contents

List of Figures

List of Tables

Declaration of Authorship

I, Jürgen Peter Zimmermann, declare that the thesis entitled *Micromagnetic simulations of magnetic exchange spring systems* and the work presented in the thesis are both my own, and have been generated by me as the result of my own original research. I confirm that:

- this work was done wholly or mainly while in candidature for a research degree at this University;
- where any part of this thesis has previously been submitted for a degree or any other qualification at this University or any other institution, this has been clearly stated;
- where I have consulted the published work of others, this is always clearly attributed;
- where I have quoted from the work of others, the source is always given. With the exception of such quotations, this thesis is entirely my own work;
- I have acknowledged all main sources of help;
- where the thesis is based on work done by myself jointly with others, I have made clear exactly what was done by others and what I have contributed myself;
- parts of this work have been published as:
  - Micromagnetic simulation of the magnetic exchange spring system $DyFe_2/YFe_2$ *Journal of Applied Physics*, 99, pp. 08B904-1–3, April 2006 (with G. Bordignon, R. P. Boardman, T. Fischbacher, H. Fangohr, K. N. Martin, G. J. Bowden, A. A. Zhukov and P. A. J. de Groot)
  - Exchange spring driven spin flop transition in $ErFe_2/YFe_2$ multilayers *Applied Physics Letters*, 89, pp. 132511-1–3, September 2006 (with K. N. Martin, K. Wang, G. J. Bowden, A. A. Zhukov , P. A. J. de Groot, H. Fangohr and R. C. C. Ward)
  - Magnetic anisotropy in the cubic Laves $REFe_2$ intermetallic compounds *Journal of Physics: Condensed Matter*, 18, pp. 459-478, December 2005 (with K. N. Martin, P. A. J. de Groot, B. D. Rainford, K. Wang, G. J. Bowden and H. Fangohr)
  - Magnetic anisotropy terms in [110] MBE-grown $REFe_2$ films involving the strain term ϵ_{xy} *Journal of Physics: Condensed Matter*, 18, pp. 5861-5871, June 2006 (with G. J. Bowden, P. A. J. de Groot, B. D. Rainford, K. Wang, K. N. Martin and H. Fangohr)

– Magnetic switching modes for $ErFe_2/YFe_2/DyFe_2/YFe_2$ exchange-spring systems with competing anisotropies: Experiments and micromagnetic simulations *Physical Review B*, submitted June 2007 (with K. N. Martin, G. Bordignon, M. Franchin, R. C. C. Ward, G. J. Bowden, P. A. J. de Groot, and H. Fangohr)

Signed: _____

Date: _____

Acknowledgements

First and foremost, I would like to express my gratitude to Dr Hans Fangohr and Prof Peter de Groot for their first-class supervision. They have shown great enthusiasm for the subject and provided assistance whenever necessary, preparing the ground for the success of this work. I am particularly appreciative of the School of Engineering Sciences PhD Studentship awarded on Dr Fangohr's endorsement.

Kevin Martin deserves many thanks for his magnetic measurements and discussions about experimental findings. I had many indispensable meetings and e-mail conversations with Prof Graham Bowden on aspects of magnetic anisotropy. I am much obliged to him.

I am extremely grateful to Dr Richard Boardman for his willingness to help on many occasions. Only with his seemingly inexhaustible knowledge could some technical problems be resolved. I appreciate the many fruitful team meetings and conversations with Giuliano Bordignon, Matteo Franchin and Dr Thomas Fischbacher who were a pleasure to work with. Thanks also to Mark Scott and Dr Steven Johnston who helped on a range of issues arising during the work on the thesis.

Meine besondere Dankbarkeit möchte ich meinen Eltern Anna und Heinrich Zimmermann zum Ausdruck bringen. Sie haben mich in der Zeit vor und während der Promotion auf vielfältige Weise unterstützt. In inniger Verbundenheit bedanke ich mich bei meiner Freundin Dr Frauke Otto. Sie hat das Projekt „Promotion in England“ befürwortet, obwohl damit eine mehrjährige räumliche Trennung unvermeidlich war. In kritischen Phasen der Promotion hat sie mir Kraft und Zuversicht gegeben.

Trademarks and copyright information

Maxtor is a trademark of Maxtor Corporation.

IBM is a registered trademark of IBM.

RAMAC is a registered trademark of IBM.

Toshiba is a registered trademark of Toshiba Corporation.

Freescale is a trademark of Freescale Semiconductor, Inc.

Nomenclature

$\mathcal{X}$	Calligraphic capitals generally denote operators
$\hat{\boldsymbol{x}}\hat{\boldsymbol{X}}$	Bold hatted characters generally denote unit vectors, or spinors
$\boldsymbol{x}\boldsymbol{X}$	Bold characters generally denote vector quantities
xX	Normal non-bold characters generally denote scalar quantities
(nmo)	Plane perpendicular to crystal direction [nmo]
$[nmo]$	Crystal direction, e.g. [110] , page 35
$\alpha_{\mathrm{L}}/\alpha_{\mathrm{G}}$	Landau-Lifshitz/Gilbert damping parameter, see equation (2.21), page 13
α_n	Cosine of an angle γ_n enclosed by a vector and the coordinate axis x$_n$, page 31
$\boldsymbol{m}$	Magnetic moment
χ	Spin part of quantum mechanical wave function of an electron, see equation (3.1), page 17
δ	Bloch domain wall width, see equation (5.1), page 57
ϵ	Strain tensor, see equation (3.83), page 36
γ	Gyromagnetic ratio, see equation (2.4), page 10
$\gamma_{\mathrm{L}}/\gamma_{\mathrm{G}}$	Gyromagnetic ratio for Landau-Lifshitz/Gilbert equation, see equation (2.21), page 13
$\hbar$	Reduced Planck's constant; Planck's constant h divided by 2π
$\mathcal{H}$	Hamiltonian operator
$\mathcal{J}$	Quantum mechanical exchange constant, see equation (3.20), page 20
$\|\uparrow\rangle, \|\downarrow\rangle$	Eigenfunctions of the one-electron spin system
μ_0	Magnetic constant, permeability of free space
$\hat{\boldsymbol{M}}$	Unit vector pointing in the direction of the magnetisation

$\boldsymbol{\mathcal{S}}$ Spinor of spin angular momentum

$\boldsymbol{\nabla}$ Napla operator

$\boldsymbol{B}$ Magnetic field (induction)

$\boldsymbol{B}_{\mathrm{app}}$ Applied field (induction)

$\boldsymbol{H}$ Magnetic field (strength)

$\boldsymbol{H}_{\mathrm{app}}$ Applied field (strength) , see equation (2.23), page 14

$\boldsymbol{H}_{\mathrm{d}}$ Dipolar or demagnetising field, see equation (2.23), page 14

$\boldsymbol{J}$ Resulting total angular momentum of a multi-electron system, see equation (2.7), page 11

$\boldsymbol{j}$ Total angular momentum (spin plus orbital momentum), page 11

$\boldsymbol{L}$ Resulting orbital angular momentum of a multi-electron system, see equation (2.7), page 11

$\boldsymbol{l}$ Orbital angular momentum

$\boldsymbol{M}$ Magnetisation vector

$\boldsymbol{r}$ Position vector

$\boldsymbol{S}$ Resulting spin of a multi-electron system, see equation (2.7), page 11

$\boldsymbol{T}$ Torque, see equation (2.9), page 12

∂_{x_i} Partial derivative in the direction of x_i

Φ Potential function, see equation (3.105), page 41

ϕ Spherical coordinate, azimuth angle

$\phi_{i,j}$ Angle enclosed by vectors $\hat{\boldsymbol{e}}_i$ and $\hat{\boldsymbol{e}}_j$, see equation (3.28), page 22

Ψ Quantum mechanical wave function of an electron, see equation (3.1), page 17

ψ Spatial part of quantum mechanical wave function of an electron, see equation (3.1), page 17

θ Spherical coordinate, zenith angle

$\tilde{K}''_{\mathrm{nmo}}$ Second-order coefficients of the multipolar decomposition base functions of the strain energy, see equation (3.85), page 36

$\tilde{K}'_{\mathrm{n}}$ First-order coefficients of the multipolar decomposition base functions of the strain energy, see equation (3.84), page 36

$\tilde{K}_n$ Coefficients of the multipolar decomposition base functions of the cubic anisotropy energy, see equation (3.78), page 34

$\triangle$ Laplace operator

ε_0 Permittivity of free space

ε_a Anisotropy energy density, see equation (2.23), page 14

ε_d Dipolar or demagnetising energy density, see equation (2.23), page 14

ε_ex Exchange energy density, see equation (2.23), page 14

ε_me Magnetoelastic energy density, see equation (3.84), page 36

ε_z Zeeman energy density, see equation (2.23), page 14

A Exchange constant, page 24

a Crystal cell base length

b_2 Magnetoelastic coefficient, see equation (3.83), page 36

C Exchange constant, see equation (3.40), page 24

d_xy, d_{242} Strain terms, page 37

E Total energy of a system

e Electron charge

E_0 Constant energy contribution

E_ex Exchange energy

g Landé factor or general g-factor, see equation (2.3), page 10

h Computational cell base length

H_b Characteristic bending field, see equation (5.4), page 60

J Resulting total angular momentum quantum number of a multi-electron system, see equation (2.7), page 11

k_B Boltzmann constant, see equation (A.2), page 111

K_n Uniaxial or cubic phenomenological anisotropy constants of order n

L Resulting orbital angular momentum quantum number of a multi-electron system, see equation (2.7), page 11

l Orbital angular or azimuthal quantum number, see equation (2.6), page 10

m_e	Electron mass
m_l	Magnetic quantum number, see equation (2.6), page 10
m_s	Spin quantum number, see equation (3.9), page 19
M_s	Saturation magnetisation (also M_sat), page 28
n	Thickness of YFe_2 layer in nm, page 88
r_T	Temperature normalisation of the atomic magnetic moment, page 74
S	Resulting spin quantum number of a multi-electron system, see equation (2.7), page 11
T	Temperature
t	Layer thickness in a multilayer system, see equation (5.1), page 57
HT	High temperature, page 83
LT	Low temperature, page 83
MBE	Molecular beam epitaxy
MC	Magnetocrystalline
MT	Moderate temperature, page 83
RE	Rare earth metals, page 67

Chapter 1

Introduction

1.1 Nanotechnology — a historical context

Nanotechnology is the field of applied science and engineering that deals with the control of matter on length-scales of nanometers, that is 1×10^{-9} m. The word *nano* is derived from the Greek $\nu\acute{\alpha}\nu o\varsigma$, meaning dwarf or tiny.

The hour of birth of nanotechnology arguably is marked by the talk *There's Plenty of Room at the Bottom* Nobel Prize winner Richard P. Feynman held on 26^{th} December 1959 at the American Physical Society meeting at the California Institute of Technology (*Feynman*, 1992). Feynman pondered the question of whether it was possible to write the entire of the 24 volumes of the Encyclopaedia Britannica on the head of a pin. He laid out the problems, and how they possibly could be overcome, *i.e.* by use of electron beams. Going one step further, he envisioned high performance computers built from miniaturised components, mass fabricated by means of myriads of microscopic machines. The machines themselves should be manufactured in a sequence of self-reproduction of iteratively downscaled and multiplied copies of macroscopic originals. An advanced version of this concept is now known as the bottom-up approach of nanotechnology: tiniest mechanical or electromagnetic units like gears or coils are assembled from individual atoms as smallest building blocks, and more complex structures or machines with unprecedented properties are then facilitated from these units.

In the following decades, tremendous progress was made in the field of nanotechnology, manifested *e.g.* in the exponential performance increase of computer processors or hard disk drives. A selection of the most significant milestones that enabled this progress is given subsequently: In the 1970s, *Dehmelt* (1989) invented the Penning trap, a device to confine charged particles in an electric and a magnetic field. This device enabled him to experiment on individual atomic elements at rest (shared Nobel Prize in Physics in 1989). *Binnig and Rohrer* (1982, 1987) (shared Nobel Prize in Physics in 1986) developed the Scanning Tunnelling Microscope (STM) around 1982. A precursor version of the STM was built by *Young et al.* (1972). In

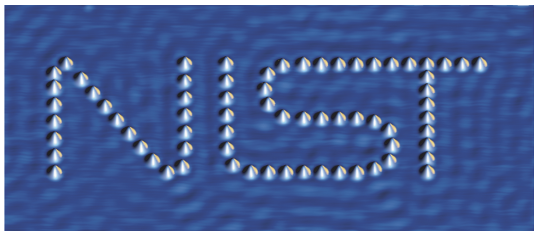

Figure 1.1: Manipulation of individual atoms: cobalt atoms on a copper surface forming the NIST logo. Courtesy of J. Stroscio, R. Celotta/NIST.

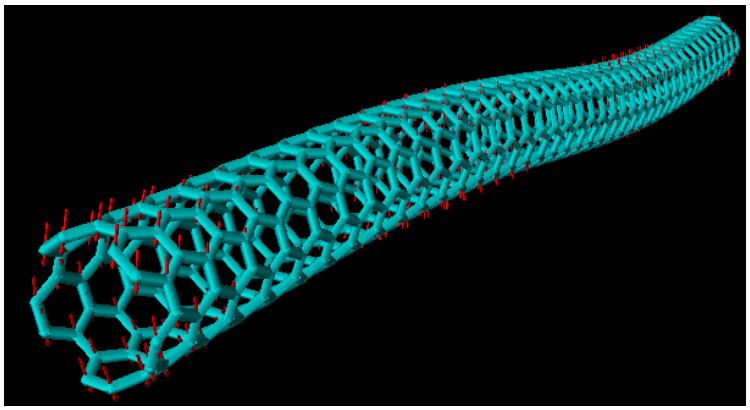

Figure 1.2: Visualisation of a carbon nanotube. The carbon atoms are located at the vertices of the hexagons forming the tube. Courtesy of I. Fernandez Rodriguez, University of Southampton.

an STM, a sharp tip is scanned over the metal surface of a probe. Weak electric tunnelling currents flow from the surface to the tip, highly sensitive to the distance in between. The detected currents are used to obtain an atomic-scale image of the surface. The STM is widely used in both industrial and fundamental research.

In 1989, IBM researchers *Eigler and Schweizer* (1990) managed to write the letters `IBM` on a nickel surface by locating and repositioning 35 individual xenon atoms, proving that atoms —in spite of their quantum mechanical nature— can be bodily manipulated. An image of individually processed cobalt atoms on a copper surface resulting from a similar experiment by National Institute of Standards and Technology (*NIST*) researchers *Stroscio and Celotta* (2004) is shown in figure 1.1.

Fullerenes are a family of carbon allotropes forming molecules of geometric objects like spheres (*Buckminsterfullerenes*, or *Buckyballs*) and cylinders (*Carbon nanotubes*). Their discovery by *Kroto et al.* (1985) (Nobel Prize in Chemistry in 1986) and *Iijima* (1991), respectively, opened up paths to new materials with properties like high tensile strength, high electrical conductivity, high ductility, high resistance to heat, and relative chemical inactivity. With an abundance of potential applications utilising these properties, carbon nanotubes (see figure 1.2 for a visualisation) have become a focal point of popular science.

Generally, the achievements of nanotechnology have already found their way

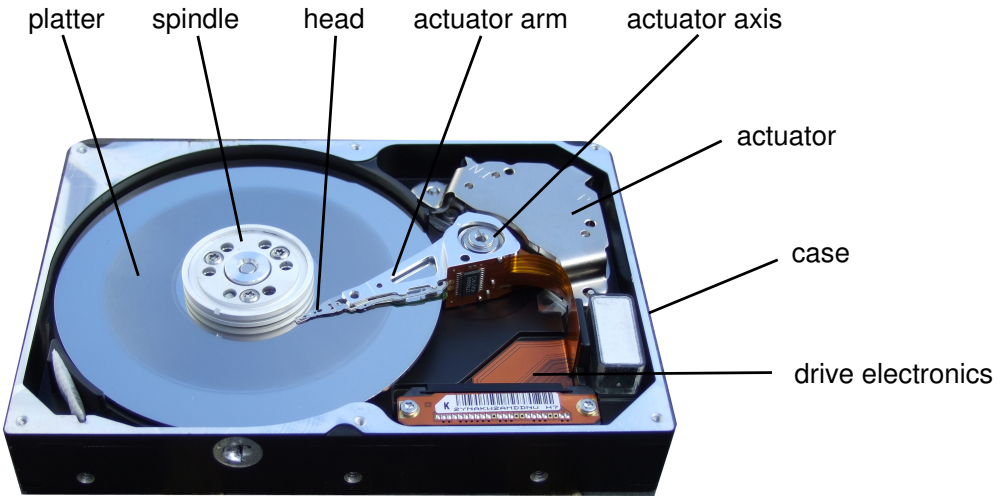

Figure 1.3: Components of a hard disk drive: Maxtor 80 Gbyte 3.5 inch model

into everyday life. To name a few applications existing or close to fruition,

- in automotive industry, car paint is used containing ceramic nano-particles in order to increase resistivity against abrasions from car wash.
- microelectromechanical systems (*MEMS*) are used as accelerometers in airbag deployment systems.
- latest digital cameras feature image stabilisation based on MEMS dual-axes gyroscopes to detect and counteract natural hand jitter.
- with respect to clothing, fabrics are treated with nanotechnology to be water-repellent as well as wrinkle, spill, stain, smell, and wear resistant.
- in medicine, the magnetic properties of nanoparticles are exploited in Magnetic Resonance Imaging (*MRI*), with high contrast efficacy for each particle; diagnostics are enhanced by MEMS laboratory-on-a-chip technology; drug delivery benefits from nano-particles functioning as molecular carriers; tissue engineering can help to reproduce or to repair damaged tissue.

Another important application sector of particular interest in the context of this thesis are magnetic storage media. They are described in more detail in the next section.

1.2 Magnetic storage media

1.2.1 Hard disk drives

The hard disk drive is a magnetic storage device with a long history: the first commercially viable product, the *RAMAC* (Random Access Method of Accounting and

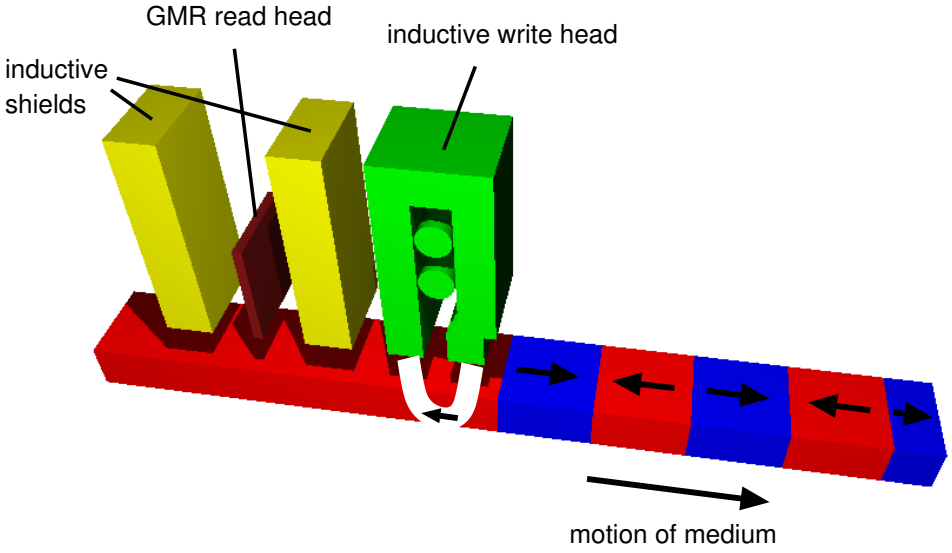

Figure 1.4: Sketch of a GMR read/write head in a hard disk drive while storing information in the magnetic medium layer.

Control) was released 50 years ago in 1956 by IBM as a part of the IBM 305 RAMAC computer (*Albrecht et al.*, 2003). Since then, the basic design has hardly changed. In figure 1.3, the components of a standard hard disk drive are depicted: a single disk, the platter, or a set of platters, rotate around a spindle at high speeds (usually 5,400 to 7,200 rpm). An integrated read/write head flies over the spinning platter surface. It is attached to the tip of an actuator arm, mounted on an actuator axis and controlled by the actual actuator in diametrical opposition. Due to the high rotational speed of the platter in relation to the tiny distance between platter and head, impurities on the platter would result in a fatal head crash. The case seals the interior of the drive and keeps it dust-free. Further hard drive components are the drive electronics and the interface to the computer.

The platters are coated with a magnetic film on which the data are stored. The read/write head follows circular tracks on the spinning platter. Figure 1.4 sketches the read/write head in operation on a section of the track: to record information bitwise, the write head magnetises successive areas along the track to one or the opposite direction by generating a strong local magnetic field (perpendicular to the film plane, or longitudinal, as in 1.4). The read head later retrieves the stored information by detecting the stray field of a magnetised area. Strictly speaking, modern read/write heads use an encoding method that translates zeros and ones into patterns of magnetic flux reversals, and vice versa.

The magnetic film has a crystalline grain structure, where each grain is effectively a single-domain nanomagnet of a size about 5 to 8 nm. A bit area typically consists of 100 to 1000 grains with mostly homogeneous magnetisation. Fewer grains in a bit area correspond to a worse signal-noise ratio, and a minimum num-

ber of grains per bit area is required.

In spite of the unchanged overall design, progress in magnetic and spintronics research has boosted the storage density. Most effective was the discovery of the giant magnetoresistance (*GMR*) in 1988 by Fert and Grünberg (*Baibich et al.*, 1988, *Binasch et al.*, 1989). A GMR device consists of a pinned and a free ferromagnetic (*FM*) layer, separated by a thin non-ferromagnetic spacer, and an antiferromagnetic (*AFM*) pinning layer, with sidewise contacts. The electrical resistance of a current flowing through the layers strongly depends on the relative orientation of the magnetisation in the two ferromagnetic layers, that is, the magnetisation direction of the free layer. Hence, the device is an extremely sensitive field detector. IBM became the first licensee of GMR in 1995 and launched its first product in 1997.

The development of new hard disk drives with increased storage densities faces the problem of the superparamagnetic limit: with shrinking bit sizes (and, inevitably, shrinking grain sizes because of noise issues), the magnetisation of the grains becomes thermally unstable, with random reversal processes and loss of data. So far, the hard disk manufacturers have been able to push the limits by means of perpendicular recording and other advanced techniques: in September 2007, *Toshiba Corporation* (2007) boosted capacity to a record-breaking 120 Gbyte on a single 1.8-inch platter, taking the storage density to 333 Gbits per square inch. Nonetheless, the superparamagnetic limit ultimately promotes an intensified research towards new approaches.

1.2.2 Magnetoresistive random access memory

Magnetoresistive random access memory (*MRAM*) is a new generation of memory that combines the advantages of conventional dynamic random access memory (*DRAM*) and hard disk drives: information is stored in a non-volatile way — bits stay persisted without requiring an electric current — and is written and retrieved directly without any mechanically moving parts (*Koltsov and Perry*, 2004). This is achieved by exploiting the spin properties of matter rather than the charge, as in the case of DRAMs.

In an MRAM, information is stored bitwise in magnetic tunnelling junctions (*MTJs*), the memory cells (see left side of figure 1.5 on the next page): each cell consists of a FM layer with a magnetisation pinned by an adjacent AFM layer, a thin insulating spacer, and another FM layer that adapts its magnetisation to an external field (the storage layer). The magnetisation direction of the storage layer encodes the information bit. It is written by close-by electric currents that induce a sufficiently high inductive field to adjust the magnetisation direction. The read-out works on the basis of spin-current effects. When a current is directed through the memory cell, the pinned FM layer acts as a spin filter, and the storage layer as a spin detector. The resistance depends on the direction of the magnetisation in the

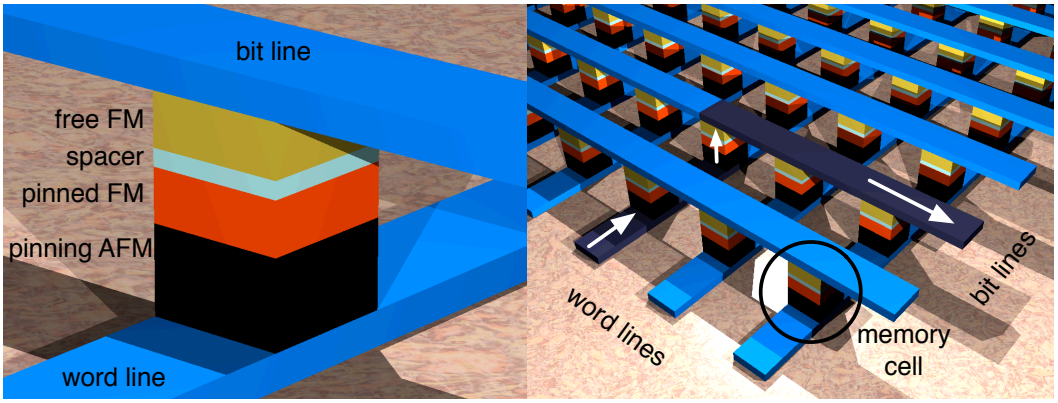

Figure 1.5: MRAM. Left: a single memory cell, consisting of an AFM pinning layer (black), a pinned FM layer (red), a spacer layer (light blue), and a free FM layer (yellow), sandwiched between a word line and a bit line. Right: 2D grid of word lines (running from front left to back right) and bit lines (running from front right to back left), with memory cells at each crosspoint. The circle marks the memory cell depicted in a close-up view to the left. The white arrows indicate the path of the read-out current through a given memory cell.

storage layer. In contrast to the GMR head of subsection 1.2.1, where the current is applied in-plane and the spacer layer is metallic, the current is applied through the layers for an MTJ and the spacer layer is an insulator.

The complete MRAM is a 2D grid of nanowire contacts — the criss-crossing word and bit lines (see right side of figure 1.5), with memory cells at each crosspoint. An individual cell is addressed by use of the corresponding word and bit line (in an xy coordinates fashion).

In July 2006, Freescale, a leading semiconductor company, started selling the first commercial MRAM module, with 4 Mbits of memory. At this stage, it is a niche product. However, it is the first realisation of a spintronics device, and next-level modules are targeted for the coming years.

1.2.3 Magnetic racetrack memory

The magnetic racetrack memory is a third concept of a magnetic storage device. It also utilises magnetic and spin-current effects for non-volatile data storage, but unlike the hard disk drive and the MRAM, the magnetic racetrack memory stores information in a three-dimensional fashion to greatly expand the storage capacity.

The racetrack is a thin U-shaped magnetic nanowire standing on end above the surface of a silicon wafer (see figure 1.6 on the next page). Along the nanowire are magnetic domains, separated by domain walls that effectively encode the information. The domain walls are moved up and down the racetrack by applying pulses of spin-polarised current to either end of the racetrack (1.6a and b). The domain wall motion, also referred to as massless motion, is a consequence of the

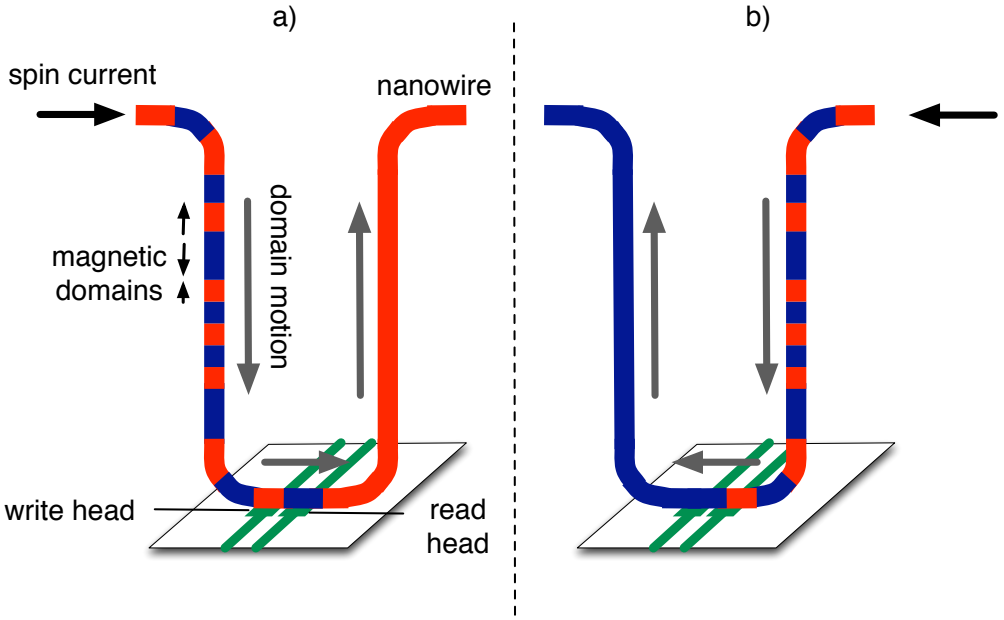

Figure 1.6: Magnetic racetrack memory: U-shaped nanowire (racetrack) on a silicon base with the read and the write head. The blue and red areas on the racetrack relate to magnetic domains magnetised in one or the opposite direction. a) spin current pulses applied from the left — clockwise domain wall motion. b) spin current pulses applied from the right — anticlockwise domain wall motion.

so-called spin-torque effect. Equidistant notches (not visible in 1.6) along the racetrack keep the magnetic domains the same size, and the current pulses move them along from notch to notch. Information is written and read by a read and a write head at the bottom of the race track on the silicon base. The read head is a magnetic tunnel junction that incorporates a small adjacent section of the racetrack as its free FM layer. A current applied through the read head then varies with the magnetic domain in the adjacent racetrack section. Bits are written into the racetrack by a magnetic fringing field from moving domain walls in the write head. The single racetrack is part of an arrangement of numerous interconnected nanowires, forming a 3D storage medium with capacities beyond existing 2D storage devices.

The magnetic racetrack memory was proposed by Dr Stuart Parkin and colleagues at IBM's Almaden Research Center in San Jose, USA, who hold several patents for the technology (*Parkin*, 2004). First prototypes exist, but the project is still in an early development phase, several years away from a commercially viable product.

1.3 Summary

Rapid progress was made in the field of nanotechnology through a succession of landmark discoveries, laying the foundations for the development of variety of nano-products and applications. At the intersection of nanotechnology and magnetism is the development of magnetic storage devices: hard disc drives represent an indispensable element of modern computer systems. Their storage density has substantially increased in the last 50 years, but is gradually approaching a physical upper limit. Alternative concepts are already devised, two of them being the MRAM and the magnetic racetrack memory.

Exchange spring systems have been proposed to enhance the characteristics of magnetic data storage. The objective of this work is the research into multilayered exchange spring systems of compounds of rare earth and transition metals, namely $DyFe_2$, $ErFe_2$, and YFe_2. Below we list the structure of the thesis.

In chapter 2, the quantum mechanical origin of the magnetic moment of atoms is discussed. The equations are recapitulated that determine the quasi-static equilibrium state and the evolution of a magnetic system.

Chapter 3 highlights the concept of micromagnetics and the relevant interactions and energies controlling the magnetic behaviour of matter on a nanometre length-scale. This knowledge is required for the use and understanding of a micromagnetic simulation code, and for the interpretation of results obtained by numerical simulations.

Chapter 4 presents a simulation code for discrete molecular dynamical magnetism, *molesim*, and the standard simulation code used in this thesis, OOMMF. Both codes are applied to a number of test cases, and the results are compared.

In chapter 5, magnetic exchange spring systems are introduced and the relevant key findings are outlined.

Unexpected reversal modes of multilayered $DyFe_2/YFe_2$ systems observed in experiments are unravelled by means of micromagnetic simulations in chapter 6.

Chapter 7 investigates the switching modes of multilayers of $ErFe_2/YFe_2$ by means of measurements and micromagnetic simulations.

In chapter 8, a configurable multilayered system of $ErFe_2/YFe_2/DyFe_2/YFe_2$ with a variable YFe_2 separation layer thickness is considered. Aspects of the separate $ErFe_2$ and $DyFe_2$ systems of the preceding two chapters are taken to a generalised form. A mapping of the switching regimes concludes this chapter.

The overall results are finally summed up in chapter 9, and an outlook for future research is provided.

Chapter 2

Computational micromagnetics

2.1 Introduction

The simulations presented in this thesis are based on a theory called *micromagnetics.* The central idea of micromagnetics is the transition from a discrete atomic structure to a continuous material. Rather than expressing the energy by considering the magnetic interactions of discrete particles inside a lattice with each other and with an external applied field, the magnetisation — and subsequently the energy — is defined on every point inside a domain. Thus, the magnetisation can be taken as a continuous function of space, and numerical methods can be applied (*Aharoni*, 2000, p. 174).

The relevant equations in this context are the equivalent Landau-Lifshitz and Gilbert equations, and Brown's static equations, discussed in sections 2.3 and 2.4, respectively. A proper understanding of the electron magnetic moment is a key issue in the derivation of the equations. For this reason, we first elucidate the quantum mechanic origin of the magnetic moment in section 2.2

2.2 Quantum mechanic origin of the magnetic moment

The classical Bohr consideration of an electron (charge e, mass m_0) orbiting around a nucleus results in an equation defining the relationship between the magnetic moment $\boldsymbol{m}$ and the orbital angular momentum $\boldsymbol{l}$ (*Haken and Wolf*, 1990):

$$\boldsymbol{m} = -\frac{e}{2\,m_0}\,\boldsymbol{l} \quad . \tag{2.1}$$

The magnetic moment can be expressed in terms of the Bohr magneton μ_B, which is defined as the magnetic moment of an electron with an angular momentum $|\boldsymbol{l}|$ equal to the reduced Planck's constant, $\hbar = \frac{h}{2\pi} = 1.054571 \cdot 10^{-34}$ Js. This is the

magnetic moment of an electron on the first Bohr orbit of a hydrogen atom:

$$\mu_{\mathrm{B}} = \frac{e}{2\,m_0}\hbar \approx 9.274078 \cdot 10^{-24}\mathrm{Am}^2 \quad . \tag{2.2}$$

Equation (2.1) can be rewritten in terms of μ_{B}. We allow for arbitrary types of angular momenta (spin or orbital), and replace $\boldsymbol{l}$ by the general orbital momentum $\boldsymbol{j}$:

$$\boldsymbol{m} = -g\,\mu_{\mathrm{B}}\frac{\boldsymbol{j}}{\hbar} \quad . \tag{2.3}$$

This equation contains the so-called general g-factor, or Landé factor, g, which measures the ratio of the magnetic moment (in Bohr magnetons) to the angular momentum (in terms of $\hbar$). The Landé factor reflects the different nature of the types of angular momenta in $\boldsymbol{j}$, and provides the generality of equation (2.3) for spin as well as orbital momenta we permitted earlier. When a specific Landé factor for a given angular momentum is stated, a subscript is used for g: for an orbital angular momentum of an electron, g_{l} is 1, so that equation (2.1) holds.

By introducing the gyromagnetic ratio γ with

$$\gamma = g\frac{\mu_B}{\hbar} \quad , \tag{2.4}$$

equation (2.3) can be rewritten as

$$\boldsymbol{m} = -\gamma\boldsymbol{j} \quad . \tag{2.5}$$

As γ depends on g, it also depends on the type of the angular momentum, *i.e.* spin or orbital.

If an external field is applied (*e.g.* in z direction), then the orbiting electron reacts like a mechanical gyroscope: the angular momentum of the electron starts a precession movement around the direction of the external field (and so does the magnetic moment). The direction of the angular momentum of the electron, as well as the direction of the corresponding magnetic moment, is not arbitrary due to quantum physical effects. Instead, it must be aligned to the reference direction of the external field in a way that for the z component l_{z} of the orbital angular momentum $\boldsymbol{l}$

$$l_{\mathrm{z}} = m_{\mathrm{l}}\hbar \quad \text{with} \;\; m_{\mathrm{l}} = 0, \pm 1, \pm 2 ... \pm l \quad . \tag{2.6}$$

While m_{l} is the magnetic quantum number, l denotes the orbital angular or azimuthal quantum number, which is the maximum l_{z} value of the orbital angular momentum vector with $\boldsymbol{l}^2 = l(l+1)\,\hbar^2$.

For a single electron with spin only, the Landé factor g is ≈ 2. However, usually

one has to consider a mixture of spin and orbital angular momenta, where both momenta couple to a total angular momentum $\boldsymbol{j}$. The method of coupling is determined by the strength of the applied magnetic field. For a comparatively weak field acting on a multi-electron atom, the angular momenta of the electrons show $\boldsymbol{LS}$ coupling: first, the individual electron spins $\boldsymbol{s}_i$ couple to a total spin $\boldsymbol{S}$. The same way, the individual orbital angular momenta $\boldsymbol{l}_i$ couple to a total orbital angular momentum $\boldsymbol{L}$. Finally, $\boldsymbol{S}$ and $\boldsymbol{L}$ couple to an overall total angular momentum $\boldsymbol{J}$. The corresponding quantum numbers, S, L, J are the lengths of the projection of the momenta on a preferred direction z, stated in units of $\hbar$. The specific Landé factor g_j then is

$$g_\mathrm{j} = 1 + \frac{J(J+1) + S(S+1) - L(L+1)}{2J(J+1)} \quad . \tag{2.7}$$

As matter in general is considered in this context, it is not possible to derive the Landé factor by means of quantum physics from quantum numbers. Instead, it is assumed to be a constant whose value is taken from experiments.

2.3 Landau-Lifshitz and Gilbert equations

The Landau-Lifshitz equations (as well as the equivalent Gilbert equations) describe the dynamical behaviour of a magnetisation $\boldsymbol{M}$ which is exposed to an effective field $\boldsymbol{H}_\mathrm{eff}$. The original paper of Landau and Lifshitz (*Landau and Lifshitz*, 1935) presented a theory of the domain wall behaviour. However, their approach was completely general and could be applied to micromagnetics, a concept which did not emerge before 1963, roughly 28 years after the paper of Landau and Lifshitz was published. The approach is to generalise the equilibrium condition of a vanishing torque, $\boldsymbol{T} = \mu_0 \left[\boldsymbol{M} \times \boldsymbol{H}_\mathrm{eff}\right]$, and to introduce a damping term. The resulting equations are (*Kronmüller and Fähnle*, 2003)

$$\frac{\mathrm{d}\boldsymbol{M}}{\mathrm{d}t} = -\mu_0 \gamma_\mathrm{L} \left[\boldsymbol{M} \times \boldsymbol{H}_\mathrm{eff}\right] - \frac{\alpha_\mathrm{L}}{|\boldsymbol{M}|} \left[\boldsymbol{M} \times \left[\boldsymbol{M} \times \boldsymbol{H}_\mathrm{eff}\right]\right] \quad , \tag{2.8}$$

where $\mu_0 = 4\pi \cdot 10^{-7}\ \mathrm{N/A^2}$ denotes the permeability of free space (also known as the magnetic constant), α_L the Landau-Lifshitz damping parameter, and γ_L is the gyromagnetic ratio that fits with the equation. The movement of the magnetisation vector is a precession around the magnetic field direction, with a gradual relaxation of $\boldsymbol{M}$ towards $\boldsymbol{H}_\mathrm{eff}$ as a result of the damping. Given an initial state, the Landau-Lifshitz equations are suitable for a temporal evolution. The remainder of this section derives equation (2.8) and shows the equivalence of Landau-Lifshitz and Gilbert equations.

2.3.1 Derivation of the equations

The torque $\boldsymbol{T}$ acting on a magnetic dipole moment $\boldsymbol{m}$ in an effective field $\boldsymbol{H}_{\mathrm{eff}}$ is given by (*Jackson*, 1999)

$$\boldsymbol{T} = \mu_0 \left[\boldsymbol{m} \times \boldsymbol{H}_{\mathrm{eff}}\right] \quad = \quad \frac{\mathrm{d}\boldsymbol{J}}{\mathrm{d}t} \quad , \tag{2.9}$$

with the magnetic constant μ_0 and a total angular momentum of the system $\boldsymbol{J}$. Recalling that the magnetisation $\boldsymbol{M}$ is defined as the total dipole moment $\boldsymbol{m}$ in a volume V,

$$\boldsymbol{M} = \frac{\boldsymbol{m}}{V} \quad , \tag{2.10}$$

equation (2.9) reads

$$\boldsymbol{T} = \mu_0 \left[\boldsymbol{M} \times \boldsymbol{H}_{\mathrm{eff}}\right] V \quad = \quad \frac{\mathrm{d}\boldsymbol{J}}{\mathrm{d}t} \quad . \tag{2.11}$$

The torque $\boldsymbol{T}$ results in a change of the angular momentum $\boldsymbol{J}$. For an equilibrium condition, one normally demands the torque to vanish. However, for a dynamic view, this is not required. We relate the angular momentum to the magnetisation by the gyromagnetic ratio γ. For one electron, the relation is given by equation (2.5) with an explicit γ. Since we want to keep generality, we write the relation in terms of an arbitrary angular momentum $\boldsymbol{J}$ rather than a specific electron momentum $\boldsymbol{j}$:

$$\begin{aligned} \boldsymbol{m} &= -\gamma \boldsymbol{J} \\ \boldsymbol{J} &= -\frac{1}{\gamma}\boldsymbol{m} = -\frac{1}{\gamma} V \boldsymbol{M} \quad . \end{aligned} \tag{2.12}$$

We define

$$\bar{\gamma} = -\gamma\mu_0 = -g\frac{\mu_B}{\hbar}\mu_0 \approx -1.1051\, g\, 10^5 \ \frac{\mathrm{m}}{\mathrm{As}} \tag{2.13}$$

using equation (2.4) and apply equation (2.12) to (2.11). This results in

$$\frac{\mathrm{d}\boldsymbol{M}}{\mathrm{d}t} \quad = \quad \bar{\gamma}\left[\boldsymbol{M} \times \boldsymbol{H}_{\mathrm{eff}}\right] \quad , \tag{2.14}$$

a precessional movement of the magnetisation around the effective magnetic field. In order to consider damping processes, Landau and Lifshitz introduced a term that is orthogonal to the term $[\boldsymbol{M} \times \boldsymbol{H}_{\mathrm{eff}}]$ and drags $\boldsymbol{M}$ into the direction of the effective field (*Landau and Lifshitz*, 1935). With the damping term, the equation becomes the previously stated Landau-Lifshitz equation (2.8).

In the Landau-Lifshitz formulation (2.8), the relaxation motion of the magnetisation vector is accelerated when the damping parameter α_{L} is increased. Gilbert

found this counterintuitive and proposed an alternative damping term which is orthogonal to the precessional movement of $\boldsymbol{M}$ (*Gilbert*, 1955):

$$\frac{\mathrm{d}\boldsymbol{M}}{\mathrm{d}t} = \gamma_{\mathrm{G}} \left[\boldsymbol{M} \times \boldsymbol{H}_{\mathrm{eff}}\right] - \frac{\alpha_{\mathrm{G}}}{M} \left[\boldsymbol{M} \times \frac{\mathrm{d}\boldsymbol{M}}{\mathrm{d}t}\right] \quad , \tag{2.15}$$

where an alternative damping term $\frac{\alpha_{\mathrm{G}}}{M}$ and gyromagnetic ratio γ_{G} is used. The way how this formulation complies with Gilbert's original intention will be explained at a later stage after deriving equation (2.21).

2.3.2 Equivalence of the equations

We will now prove that the Landau-Lifshitz and the Gilbert equations are consistent despite the use of differing damping terms. For this, we insert the complete equation (2.15) into the term $\frac{\mathrm{d}\boldsymbol{M}}{\mathrm{d}t}$ on the right hand side of the equation (2.15),

$$\begin{aligned} \frac{\mathrm{d}\boldsymbol{M}}{\mathrm{d}t} &= \gamma_{\mathrm{G}} \left[\boldsymbol{M} \times \boldsymbol{H}_{\mathrm{eff}}\right] \\ &\quad -\frac{\alpha_{\mathrm{G}}}{M}\gamma_{\mathrm{G}}\boldsymbol{M} \times \left[\boldsymbol{M} \times \boldsymbol{H}_{\mathrm{eff}}\right] + \frac{{\alpha_{\mathrm{G}}}^2}{M^2}\boldsymbol{M} \times \left[\boldsymbol{M} \times \frac{\mathrm{d}\boldsymbol{M}}{\mathrm{d}t}\right] \quad , \end{aligned} \tag{2.16}$$

applying the linearity properties of the vector product,

$$\boldsymbol{a} \times [\boldsymbol{b} + \boldsymbol{c}] = \boldsymbol{a} \times \boldsymbol{b} + \boldsymbol{a} \times \boldsymbol{c} \quad . \tag{2.17}$$

With Lagrange 's formula

$$\boldsymbol{a} \times [\boldsymbol{b} \times \boldsymbol{c}] = (\boldsymbol{a} \cdot \boldsymbol{c})\, \boldsymbol{b} - (\boldsymbol{a} \cdot \boldsymbol{b})\, \boldsymbol{c} \tag{2.18}$$

we get

$$\begin{aligned} \frac{\mathrm{d}\boldsymbol{M}}{\mathrm{d}t} &= \gamma_{\mathrm{G}} \left[\boldsymbol{M} \times \boldsymbol{H}_{\mathrm{eff}}\right] - \frac{\alpha_{\mathrm{G}}}{M}\gamma_{\mathrm{G}} \left[\boldsymbol{M} \times \left[\boldsymbol{M} \times \boldsymbol{H}_{\mathrm{eff}}\right]\right] \\ &\quad -\frac{{\alpha_{\mathrm{G}}}^2}{M^2} \left[M^2 \frac{\mathrm{d}\boldsymbol{M}}{\mathrm{d}t} - \left(\frac{\mathrm{d}\boldsymbol{M}}{\mathrm{d}t} \cdot \boldsymbol{M}\right) \boldsymbol{M}\right] \quad . \end{aligned} \tag{2.19}$$

As $|\boldsymbol{M}|$ is constant, it follows that $\frac{\mathrm{d}\boldsymbol{M}}{\mathrm{d}t} \perp \boldsymbol{M}$, and the last scalar product vanishes. Finally, $\frac{\mathrm{d}\boldsymbol{M}}{\mathrm{d}t}$ is isolated on the left side of the equation, and the final state is

$$\frac{\mathrm{d}\boldsymbol{M}}{\mathrm{d}t} = \frac{\gamma_{\mathrm{G}}}{1 + {\alpha_{\mathrm{G}}}^2} \left[\boldsymbol{M} \times \boldsymbol{H}_{\mathrm{eff}}\right] - \frac{\alpha_{\mathrm{G}}\gamma_{\mathrm{G}}}{\left(1 + {\alpha_{\mathrm{G}}}^2\right) M} \left[\boldsymbol{M} \times \left[\boldsymbol{M} \times \boldsymbol{H}_{\mathrm{eff}}\right]\right] \quad . \tag{2.20}$$

With the replacements

$$\gamma_{\mathrm{L}} = \frac{\gamma_{\mathrm{G}}}{1 + {\alpha_{\mathrm{G}}}^2} \quad , \quad \alpha_{\mathrm{L}} = \frac{\alpha_{\mathrm{G}}\gamma_{\mathrm{G}}}{1 + {\alpha_{\mathrm{G}}}^2} = \alpha_{\mathrm{G}}\gamma_{\mathrm{L}} \quad , \tag{2.21}$$

the Gilbert equation (2.15) is transformed to the Landau-Lifshitz equation (2.8). From (2.21), we see that Gilbert's original motivation to use a damping term that slows down the relaxation is reflected in the reciprocal relationship of α_{L} and α_{G}.

2.4 Brown's equations

By writing down the magnetic Gibbs free energy, which is composed of a set of energies listed below, Brown derived a set of equations under the assumption of micromagnetics (*Brown*, 1963). In other words, Brown's equations express the energy E as a function of a continuous magnetisation $\boldsymbol{M}(\boldsymbol{r})$ with a constant magnitude $|\boldsymbol{M}|$ (*Aharoni*, 2000, chap. 8.3):

$$E = \int_{\mathrm{V}} \left[\varepsilon_{\mathrm{ex}} + \varepsilon_{\mathrm{a}} + \varepsilon_{\mathrm{z}} + \varepsilon_{\mathrm{d}}\right] \mathrm{d}V \tag{2.22}$$

$$= \int_{\mathrm{V}} \left[\frac{1}{2} \frac{C}{|\boldsymbol{M}|^2} (\boldsymbol{\nabla} \cdot \boldsymbol{M})^2 + \varepsilon_{\mathrm{a}} - \boldsymbol{M} \cdot \boldsymbol{H}_{\mathrm{app}} - \frac{1}{2} \boldsymbol{M} \cdot \boldsymbol{H}_{\mathrm{d}} \right] \mathrm{d}V \tag{2.23}$$

The integral runs over the volume of the ferromagnetic body. The constituent energies will be discussed in detail in chapter 3. They are (from left to right)

- exchange energy (density $\varepsilon_{\mathrm{ex}}$) due to the interaction of the spins of the next neighbours (section 3.2)
- volume anisotropy energy due to the crystal structure with easy/hard axes, with ε_{a} denoting the energy density inside the specimen (section 3.3)
- Zeeman energy (density ε_{z}) due to an applied external field $\boldsymbol{H}_{\mathrm{app}}$ (section 3.4)
- stray field energy or demagnetising energy (density ε_{d}) due to the dipolar nature of the individual magnetic particles that produce the stray field $\boldsymbol{H}_{\mathrm{d}}$ (section 3.4)

The anisotropy energy term ε_{a} can be specified for a given symmetry, i.e. uniaxial or cubic symmetry. This depends on the crystal type of the specimen material. The demagnetising energy is the only long-ranging interaction and is computationally most demanding.

Expression (2.22) determines the energy if $\boldsymbol{M}(\boldsymbol{r})$ is known. However, the objective usually is to find the configuration $\boldsymbol{M}(\boldsymbol{r})$ that minimises the energy and that corresponds to the thermodynamic equilibrium. One approach is to apply variational methods on (2.22). When small variations of the magnetisation are considered, the following equation can be derived (*Aharoni*, 2000, chap. 8.3):

$$\boldsymbol{M} \times \left(\frac{C}{|\boldsymbol{M}|^2} \left(\boldsymbol{\nabla} \cdot \boldsymbol{M} \right)^2 + |\boldsymbol{M}| \left(\boldsymbol{H}_{\mathrm{app}} + \boldsymbol{H}_{\mathrm{d}} \right) - |\boldsymbol{M}| \frac{\partial \varepsilon_{\mathrm{a}}}{\partial \boldsymbol{M}} \right) = 0 \quad . \tag{2.24}$$

Equation (2.24) is known as Brown's differential equation. In an equilibrium state, the magnetisation is parallel to an effective field that points into the direction of the vector term enclosed by the brackets.

Chapter 3

Magnetic interactions

The findings on the anisotropy of MBE-grown rare earth compounds described in sections 3.3.4 and 3.3.6 have been published in *Journal of Physics: Condensed Matter* (*Bowden et al.*, 2006, *Martin et al.*, 2006a). The thesis author's contribution lies in the verification of the calculated anisotropy constants by means of micromagnetic simulations.

3.1 Introduction

In this chapter, we go into details about the different energy constituents of Brown's equation (2.22). Thus, we provide the foundations to program, use, and extend micromagnetic simulation code, and to interpret and understand the results.

First, the exchange energy is considered in section 3.2. An equation is derived from quantum mechanical principles that describes the exchange energy of a pair of electrons (3.2.1). This equation is transformed into a form that is suitable in the context of micromagnetics, where the relevant quantities are continuous functions of space (3.2.2). Next, the energy equation is discretised for application in finite difference simulation codes (3.2.3).

In section 3.3, we explain different types of magnetic anisotropy, uniaxial and cubic (3.3.1 to 3.3.4), and point out the implications for the cubic anisotropy when the magnetic material is grown by molecular beam epitaxy (MBE) with a [110] growth direction (3.3.5). We find that an additional strain term has to be taken into account (3.3.6).

Finally, the relevant equations for the Zeeman and dipolar energies are discussed in section 3.4.

3.2 Exchange energy

The conduction energy band and the energy band of the valence electrons overlap in conductors, so that a fraction of the valence electrons can freely move around

the solid state as conduction electrons (*Kittel*, 1996, chap. 7). The remaining valence electrons are bound to the ions inside the lattice. Their quantum mechanical wave functions extend to a distance of the respective nucleus depending on the orbital they are allocated at. Thus, they overlap with electrons of neighbouring ions, causing an additional energy term that is purely of quantum mechanical nature and that has no classical equivalent.

It will be shown that the exchange interaction favours alignment of neighbouring electron spins. This energy is extremely short-ranged, as the electron wave function decays exponentially. Together with the long-ranged dipolar interaction, the exchange interaction is responsible for the formation of domains, a phenomenon that stretches to almost macroscopic length-scales. In this respect, the observation of domains reveals the quantum mechanical foundation of nature.

3.2.1 Quantum mechanic origin

The fundamental reason for the existence of exchange interaction is the nature of the electrons: electrons are fermions — particles, whose spin is $\left(n + \frac{1}{2}\right)\hbar$, with $\hbar$ being the reduced Planck's constant, and n being a non-negative integer. This implies that the wave function is antisymmetric, and that the Pauli exclusion principle applies. Keeping this in mind, we can now derive the relevant equations for the energy associated with the exchange interaction (*Blundell*, 2001, chap. 4). In the first instance, the interaction of two electrons is considered.

Let us assume $\Psi_{\mathrm{a}}(\boldsymbol{r}_1)$ and $\Psi_{\mathrm{b}}(\boldsymbol{r}_2)$ are the wave functions of separated electrons, being in spin state a, and b, respectively. Each wave function $\Psi(\boldsymbol{r})$ consists of a spatial part $\psi(\boldsymbol{r})$ and a spin part χ,

$$\Psi(\boldsymbol{r}) = \psi(\boldsymbol{r})\chi \quad . \tag{3.1}$$

The normalised wave function of a two-electron system must still be antisymmetric, and thus is either

$$\Psi_{\mathrm{S}}(\boldsymbol{r}_1, \boldsymbol{r}_2) = \frac{1}{\sqrt{2}} \left[\psi_{\mathrm{a}}(\boldsymbol{r}_1)\psi_{\mathrm{b}}(\boldsymbol{r}_2) + \psi_{\mathrm{a}}(\boldsymbol{r}_2)\psi_{\mathrm{b}}(\boldsymbol{r}_1) \right] \chi_{\mathrm{S}} \quad , \tag{3.2}$$

with a symmetric spatial part and an antisymmetric spin part, or

$$\Psi_{\mathrm{T}}(\boldsymbol{r}_1, \boldsymbol{r}_2) = \frac{1}{\sqrt{2}} \left[\psi_{\mathrm{a}}(\boldsymbol{r}_1)\psi_{\mathrm{b}}(\boldsymbol{r}_2) - \psi_{\mathrm{a}}(\boldsymbol{r}_2)\psi_{\mathrm{b}}(\boldsymbol{r}_1) \right] \chi_{\mathrm{T}} \quad , \tag{3.3}$$

with an antisymmetric spatial part and a symmetric spin part. The index S stands for singlet, because an antisymmetric spin part χ_{S} corresponds to a vanishing total spin (total spin quantum number $S = 0$). Accordingly, the index T denotes a triplet state with symmetric spin part χ_{T} and $S = 1$.

Now we want to describe the energy of a two-electron system. The Hamiltonian for the electron pair is

$$\begin{aligned}\mathcal{H}^{\text{pair}} &= -\frac{\hbar^2}{2m_\text{e}}\boldsymbol{\nabla}_1^2 - \frac{\hbar^2}{2m_\text{e}}\boldsymbol{\nabla}_2^2 + V_1 + V_2 + \frac{e^2}{4\pi\varepsilon_0|\boldsymbol{r}_1 - \boldsymbol{r}_2|^2} \\ &= \mathcal{H}^0 + \frac{e^2}{4\pi\varepsilon_0|\boldsymbol{r}_1 - \boldsymbol{r}_2|^2} \\ &= \mathcal{H}^0 + \mathcal{H}^{\text{ex}} \end{aligned} \tag{3.4}$$

with ε_0 being the permittivity of free space, e the electron charge, and m_e the electron mass. The Hamiltonian fragment $\mathcal{H}^0$ contains the kinetic energies as well as the potential energies of the electrons in the electric field of the nuclei - the energies of two isolated electrons. The part of the Hamiltonian representing the electron interaction, $\mathcal{H}^{\text{ex}}$, is the interesting one in this context. It is supposed to be small compared to $\mathcal{H}^0$, and is treated by perturbation methods.

Generally, the energy of a wave function is the expectation value of the Hamilton operator $\mathcal{H}$:

$$E = \int \sum_{\text{spin states}} \Psi^*(\boldsymbol{r})\mathcal{H}\Psi(\boldsymbol{r}) \quad \mathrm{d}\boldsymbol{r} \tag{3.5}$$

When we apply (3.5) on the Hamiltonian $\hat{\mathcal{H}}^{\text{pair}}$, the summation over all the spin states can be isolated, and results in a factor of 1. This is because the Hamiltonian does not act on the spin function, and the spin functions are normalised ($\sum_{\text{states}} \chi^*\chi = 1$). We get

$$E = E_0 + \int \psi^*(\boldsymbol{r})\mathcal{H}^{\text{ex}}\psi(\boldsymbol{r})\,\mathrm{d}\boldsymbol{r} = E_0 + E_{\text{ex}} \quad . \tag{3.6}$$

It is emphasised that the remaining spatial wave function still depends on the spin state (singlet or triplet) because of the symmetry assumptions of (3.2) and (3.3).

In the following, we are only interested in the energy term E_{ex}, as only this term describes the interaction of the two electrons. In order to evaluate this energy term for the given wave functions (3.2) and (3.3), a brief recap of some essentials of spinor theory is necessary.

The spin angular momentum operator $\boldsymbol{\mathcal{S}}$ is defined as a spinor

$$\boldsymbol{\mathcal{S}} = \begin{pmatrix} \mathcal{S}_\text{x} \\ \mathcal{S}_\text{y} \\ \mathcal{S}_\text{z} \end{pmatrix} \tag{3.7}$$

with the components being matrices

$$\mathcal{S}_{\mathrm{x}} = \frac{1}{2}\begin{pmatrix} 0 & 1 \\ 1 & 0 \end{pmatrix}, \quad \mathcal{S}_{\mathrm{y}} = \frac{1}{2}\begin{pmatrix} 0 & -i \\ i & 0 \end{pmatrix}, \quad \mathcal{S}_{\mathrm{z}} = \frac{1}{2}\begin{pmatrix} 1 & 0 \\ 0 & -1 \end{pmatrix} \quad . \tag{3.8}$$

The operator components of $\boldsymbol{\mathcal{S}}$ are used to determine the observables of a spin system, which are the eigenvalues of the operators. For example, the observable m_{s} of a spin pointing along the z direction is

$$m_{\mathrm{s}} = \pm\frac{1}{2} \quad , \tag{3.9}$$

corresponding to the eigenfunctions $|\uparrow\rangle = \begin{pmatrix} 1 \\ 0 \end{pmatrix}$ and $|\downarrow\rangle = \begin{pmatrix} 0 \\ 1 \end{pmatrix}$, because

$$\mathcal{S}_{\mathrm{z}}|\uparrow\rangle = \frac{1}{2}|\uparrow\rangle, \qquad \mathcal{S}_{\mathrm{z}}|\downarrow\rangle = -\frac{1}{2}|\downarrow\rangle \quad . \tag{3.10}$$

In this spinor notation, the Hamiltonian $\mathcal{H}^{\mathrm{spin}}$ of two electrons a and b is given by

$$\mathcal{H}^{\mathrm{spin}} = A\,\boldsymbol{\mathcal{S}}^{\mathrm{a}} \cdot \boldsymbol{\mathcal{S}}^{\mathrm{b}} \quad . \tag{3.11}$$

The constant A of the spin interaction will be substituted later by means of the singlet and triplet state energies. The total spin $\boldsymbol{\mathcal{S}}^{\mathrm{tot}}$ is represented by

$$\boldsymbol{\mathcal{S}}^{\mathrm{tot}} = \boldsymbol{\mathcal{S}}^{\mathrm{a}} + \boldsymbol{\mathcal{S}}^{\mathrm{b}} \quad . \tag{3.12}$$

The square of $\boldsymbol{\mathcal{S}}^{\mathrm{tot}}$ is

$$\left(\boldsymbol{\mathcal{S}}^{\mathrm{tot}}\right)^2 = \left(\boldsymbol{\mathcal{S}}^{\mathrm{a}}\right)^2 + \left(\boldsymbol{\mathcal{S}}^{\mathrm{b}}\right)^2 + 2\boldsymbol{\mathcal{S}}^{\mathrm{a}} \cdot \boldsymbol{\mathcal{S}}^{\mathrm{b}} \quad , \tag{3.13}$$

and the Hamiltonian finally is

$$\mathcal{H}^{\mathrm{spin}} = \frac{A}{2}\Big(\left(\boldsymbol{\mathcal{S}}^{\mathrm{tot}}\right)^2 - \left(\boldsymbol{\mathcal{S}}^{\mathrm{a}}\right)^2 - \left(\boldsymbol{\mathcal{S}}^{\mathrm{b}}\right)^2\Big) \quad . \tag{3.14}$$

In order to find the eigenvalues of this Hamiltonian, we determine the eigenvalues of each constituent of equation (3.14). Since

$$\mathcal{S}_{\mathrm{x}}^2 = \mathcal{S}_{\mathrm{y}}^2 = \mathcal{S}_{\mathrm{z}}^2 = \frac{1}{4}\begin{pmatrix} 1 & 0 \\ 0 & 1 \end{pmatrix} = \frac{1}{4}\mathbb{1} \quad , \tag{3.15}$$

the eigenvalue of $\mathcal{S}_{\mathrm{x}}^2$, $\mathcal{S}_{\mathrm{y}}^2$, $\mathcal{S}_{\mathrm{z}}^2$ is $\frac{1}{4}$, and the eigenvalue of $\boldsymbol{\mathcal{S}}^2 = \mathcal{S}_{\mathrm{x}}^2 + \mathcal{S}_{\mathrm{y}}^2 + \mathcal{S}_{\mathrm{z}}^2$ is $\frac{3}{4}$. The

eigenvalue of $\boldsymbol{\mathcal{S}}^{\mathrm{tot}^2}$ is $S(S+1)$, so that the eigenvalues of $\mathcal{H}^{\mathrm{spin}}$ are

$$E_{\mathrm{spin}} = \frac{A}{2}\left[S(S+1) - \frac{3}{2}\right] \quad . \tag{3.16}$$

This leads to the energy levels for the singlet ($S = 0$) and triplet ($S = 1$):

$$E_{\mathrm{T}} = \frac{1}{4}A, \qquad E_{\mathrm{S}} = -\frac{3}{4}A \quad , \tag{3.17}$$

and the spin Hamiltonian (3.11) can be written in terms of the singlet and triplet energies,

$$\mathcal{H}^{\mathrm{spin}} = (E_{\mathrm{T}} - E_{\mathrm{S}})\, \boldsymbol{\mathcal{S}}^{\mathrm{a}} \cdot \boldsymbol{\mathcal{S}}^{\mathrm{b}} \quad . \tag{3.18}$$

Under the assumption of localised electrons in orthogonal orbitals, it is legitimate to assume that the Hamiltonian $\mathcal{H}^{\mathrm{ex}}$ of weakly interacting electrons (3.4) provides the same eigenvalues as an effective Hamiltonian of the form (3.18) (*Herring*, 1963) with

$$\mathcal{H}^{\mathrm{eff}} = -2\,\mathcal{J}\,\boldsymbol{\mathcal{S}}^{\mathrm{a}} \cdot \boldsymbol{\mathcal{S}}^{\mathrm{b}} \quad , \tag{3.19}$$

where $\mathcal{J}$ is the exchange constant, being defined as one half of the energy difference of singlet and triplet:

$$\mathcal{J} = \frac{E_{\mathrm{S}} - E_{\mathrm{T}}}{2} = -\frac{1}{2}A \quad . \tag{3.20}$$

Now we express $\mathcal{J}$ in terms of the wave functions. Therefore, it is necessary to rewrite the exchange energy of a singlet and triplet by using equations (3.2), (3.3), and (3.6):

$$\begin{aligned} E_{\mathrm{S}}^{\mathrm{ex}} &= \iint \psi_{\mathrm{S}}^{*}(\boldsymbol{r}_1, \boldsymbol{r}_2)\mathcal{H}^{\mathrm{ex}}\psi_{\mathrm{S}}(\boldsymbol{r}_1, \boldsymbol{r}_2)\mathrm{d}\boldsymbol{r}_1\mathrm{d}\boldsymbol{r}_2 \\ &= \frac{1}{2}\iint [\psi_{\mathrm{a}}^{*}(\boldsymbol{r}_1)\psi_{\mathrm{b}}^{*}(\boldsymbol{r}_2)\mathcal{H}^{\mathrm{ex}}\psi_{\mathrm{a}}(\boldsymbol{r}_1)\psi_{\mathrm{b}}(\boldsymbol{r}_2) \\ &\qquad +\psi_{\mathrm{a}}^{*}(\boldsymbol{r}_1)\psi_{\mathrm{b}}^{*}(\boldsymbol{r}_2)\mathcal{H}^{\mathrm{ex}}\psi_{\mathrm{a}}(\boldsymbol{r}_2)\psi_{\mathrm{b}}(\boldsymbol{r}_1) \\ &\qquad +\psi_{\mathrm{a}}^{*}(\boldsymbol{r}_2)\psi_{\mathrm{b}}^{*}(\boldsymbol{r}_1)\mathcal{H}^{\mathrm{ex}}\psi_{\mathrm{a}}(\boldsymbol{r}_1)\psi_{\mathrm{b}}(\boldsymbol{r}_2) \\ &\qquad +\psi_{\mathrm{a}}^{*}(\boldsymbol{r}_2)\psi_{\mathrm{b}}^{*}(\boldsymbol{r}_1)\mathcal{H}^{\mathrm{ex}}\psi_{\mathrm{a}}(\boldsymbol{r}_2)\psi_{\mathrm{b}}(\boldsymbol{r}_1)]\,\mathrm{d}\boldsymbol{r}_1\mathrm{d}\boldsymbol{r}_2 \quad , \end{aligned} \tag{3.21}$$

$$
\begin{aligned}
E_{\mathrm{T}}^{\mathrm{ex}} &= \iint \psi_{\mathrm{T}}^{*}(\boldsymbol{r}_1,\boldsymbol{r}_2)\mathcal{H}^{\mathrm{ex}}\psi_{\mathrm{T}}(\boldsymbol{r}_1,\boldsymbol{r}_2)\mathrm{d}\boldsymbol{r}_1\mathrm{d}\boldsymbol{r}_2 \\
&= \frac{1}{2}\iint [\psi_{\mathrm{a}}^{*}(\boldsymbol{r}_1)\psi_{\mathrm{b}}^{*}(\boldsymbol{r}_2)\mathcal{H}^{\mathrm{ex}}\psi_{\mathrm{a}}(\boldsymbol{r}_1)\psi_{\mathrm{b}}(\boldsymbol{r}_2) \\
&\qquad -\psi_{\mathrm{a}}^{*}(\boldsymbol{r}_1)\psi_{\mathrm{b}}^{*}(\boldsymbol{r}_2)\mathcal{H}^{\mathrm{ex}}\psi_{\mathrm{a}}(\boldsymbol{r}_2)\psi_{\mathrm{b}}(\boldsymbol{r}_1) \\
&\qquad -\psi_{\mathrm{a}}^{*}(\boldsymbol{r}_2)\psi_{\mathrm{b}}^{*}(\boldsymbol{r}_1)\mathcal{H}^{\mathrm{ex}}\psi_{\mathrm{a}}(\boldsymbol{r}_1)\psi_{\mathrm{b}}(\boldsymbol{r}_2) \\
&\qquad +\psi_{\mathrm{a}}^{*}(\boldsymbol{r}_2)\psi_{\mathrm{b}}^{*}(\boldsymbol{r}_1)\mathcal{H}^{\mathrm{ex}}\psi_{\mathrm{a}}(\boldsymbol{r}_2)\psi_{\mathrm{b}}(\boldsymbol{r}_1)]\,\mathrm{d}\boldsymbol{r}_1\mathrm{d}\boldsymbol{r}_2 \quad . \qquad (3.22)
\end{aligned}
$$

Hence the energy difference can be written as

$$
\begin{aligned}
E_{\mathrm{S}}^{\mathrm{ex}} - E_{\mathrm{T}}^{\mathrm{ex}} &= \iint [\psi_{\mathrm{a}}^{*}(\boldsymbol{r}_1)\psi_{\mathrm{b}}^{*}(\boldsymbol{r}_2)\mathcal{H}^{\mathrm{ex}}\psi_{\mathrm{a}}(\boldsymbol{r}_2)\psi_{\mathrm{b}}(\boldsymbol{r}_1) \\
&+ \psi_{\mathrm{a}}^{*}(\boldsymbol{r}_2)\psi_{\mathrm{b}}^{*}(\boldsymbol{r}_1)\mathcal{H}^{\mathrm{ex}}\psi_{\mathrm{a}}(\boldsymbol{r}_1)\psi_{\mathrm{b}}(\boldsymbol{r}_2)]\,\mathrm{d}\boldsymbol{r}_1\mathrm{d}\boldsymbol{r}_2 \quad . \qquad (3.23)
\end{aligned}
$$

As the exchange Hamiltonian (3.4) is symmetric regarding exchange of $\boldsymbol{r}_1$ and $\boldsymbol{r}_2$, we get the energy difference

$$
E_{\mathrm{S}}^{\mathrm{ex}} - E_{\mathrm{T}}^{\mathrm{ex}} = 2\iint [\psi_{\mathrm{a}}^{*}(\boldsymbol{r}_1)\psi_{\mathrm{b}}^{*}(\boldsymbol{r}_2)\mathcal{H}^{\mathrm{ex}}\psi_{\mathrm{a}}(\boldsymbol{r}_2)\psi_{\mathrm{b}}(\boldsymbol{r}_1)]\,\mathrm{d}\boldsymbol{r}_1\mathrm{d}\boldsymbol{r}_2 \quad , \qquad (3.24)
$$

and the exchange constant $\mathcal{J}$ finally is

$$
\mathcal{J} = \iint [\psi_{\mathrm{a}}^{*}(\boldsymbol{r}_1)\psi_{\mathrm{b}}^{*}(\boldsymbol{r}_2)\mathcal{H}^{\mathrm{ex}}\psi_{\mathrm{a}}(\boldsymbol{r}_2)\psi_{\mathrm{b}}(\boldsymbol{r}_1)]\,\mathrm{d}\boldsymbol{r}_1\mathrm{d}\boldsymbol{r}_2 \quad . \qquad (3.25)
$$

According to the definition of $\mathcal{J}$ in (3.20), a positive value of J means that the triplet state ($S = 1$) with spins in parallel alignment is favoured, and vice versa. Equation (3.19) was derived for two electrons. For atoms with many electrons, the valence electrons provide the vast majority of the exchange interaction, as electrons of inner shells are tightly bound to the nucleus and do not overlap with electrons of other atoms. Still, the problem usually involves more than two electrons, but the assumption is that the overall Hamiltonian is made up by the Hamiltonians of the interacting pairs, resulting in the so-called Heisenberg Hamiltonian

$$
\mathcal{H}^{\mathrm{H}} = -\sum_{i,j} \mathcal{J}_{ij}\,\boldsymbol{\mathcal{S}}_i \cdot \boldsymbol{\mathcal{S}}_j \quad , \qquad (3.26)
$$

where $\mathcal{J}_{ij}$ is the exchange constant of the electron pair (i,j) with spins $\boldsymbol{\mathcal{S}}_i$ and $\boldsymbol{\mathcal{S}}_j$. The factor of 2 is omitted because the summation accounts twice for each pair.

3.2.2 Continuum approximation

The considerations of section 3.2.1 were based on the existence of individual atoms and the associated spins of their electron wave functions. However, there is the necessity to transform the discrete equation (3.26) to a form that is applicable to a continuous material. This transition is the core of *micromagnetics*: the atomic struc-

ture of matter is ignored and the magnetisation vector is taken as a continuous function of space (*Brown*, 1963).

Since the exchange interaction is strong on short ranges, and since the exchange interaction tries to align spins, the difference of the spin directions of neighbouring particles is assumed to be sufficiently small. For the derivation, it is further assumed that the material is homogeneous, or in other words, the spin magnitude does not differ (but the spin direction does).

The spins of N particles, $\boldsymbol{S}_i$ with $i \leq N$, are regarded as classical vectors (hence the omission of the calligraphic operator font for the $\boldsymbol{S}_i$). The spins interact and provide an additional energy term which is represented by the Heisenberg exchange Hamiltonian $\mathcal{H}^{\mathrm{H}}$ in equation (3.26). Under the assumption of a constant $\mathcal{J} = \mathcal{J}_{ij}$, this equation reads

$$\mathcal{H}^{\mathrm{H}} = -\mathcal{J} \sum_{i,j} \boldsymbol{S}_i \cdot \boldsymbol{S}_j \quad . \tag{3.27}$$

Knowing that the exchange energy is extremely short-ranged, only nearest neighbour pairs are included for a good approximation. The energy E_{ex} is the expectation value of $\mathcal{H}^{\mathrm{H}}$,

$$E_{\mathrm{ex}} = \langle \mathcal{H}^{\mathrm{H}} \rangle = -\mathcal{J} S^2 \sum_{\text{neighbouring } i,j} \cos \phi_{i,j} \quad , \tag{3.28}$$

with $\phi_{i,j}$ being the angle formed by the classical spin vectors $\boldsymbol{S}_i$ and $\boldsymbol{S}_j$, and S being $|\boldsymbol{S}_i| = |\boldsymbol{S}_j|$. The cosine is approximated by $\cos \phi_{i,j} \approx 1 - \frac{\phi_{i,j}^2}{2}$ for $\phi_{i,j} \ll 1$, so that

$$E_{\mathrm{ex}} = \mathrm{const} + \frac{1}{2} \mathcal{J} S^2 \sum_{\text{neighbouring } i,j} \phi_{i,j}^2 \quad . \tag{3.29}$$

We disregard the constant energy term, because only relative energy differences matter, rather than the absolute energy. Next, we substitute the angle $\phi_{i,j}$. For any small angle, the length of a circle segment can be approximated by the length of the direct connection of the segment points. So for all unit vectors $\hat{\boldsymbol{e}}_i$, $\hat{\boldsymbol{e}}_j$ enclosing an angle $\phi_{i,j}$,

$$|\hat{\boldsymbol{e}}_{ij}| = |\hat{\boldsymbol{e}}_j - \hat{\boldsymbol{e}}_i| \approx |\sphericalangle(\hat{\boldsymbol{e}}_i, \hat{\boldsymbol{e}}_j)| = |\phi_{i,j}| \quad . \tag{3.30}$$

We now introduce unit vectors $\hat{\boldsymbol{M}}_i = \hat{\boldsymbol{M}}(\boldsymbol{r}_i) = \frac{\boldsymbol{M}(\boldsymbol{r}_i)}{|\boldsymbol{M}(\boldsymbol{r}_i)|}$. These are vectors which are defined at the locations of the particles, where they are aligned with the respective spin directions. However, we generalise the discrete vectors by introducing a vector function $\hat{\boldsymbol{M}}(\boldsymbol{r})$, which is defined everywhere within the material, and the vector at the particle location is parallel to the particle spin (micromagnetic approach). The vector function $\hat{\boldsymbol{M}}_j$ at a point $\boldsymbol{r}_j$ can be expressed by a Taylor expan-

sion around a particle location $\boldsymbol{r}_i$ (*Bronstein and Semendjajew*, 1989, p. 565):

$$\hat{\boldsymbol{M}}_j = \hat{\boldsymbol{M}}_i + (\boldsymbol{r}_{ij} \cdot \boldsymbol{\nabla})\hat{\boldsymbol{M}}_i + \dots \tag{3.31}$$

where $\boldsymbol{r}_{ij} = \boldsymbol{r}_j - \boldsymbol{r}_i$. Inserting (3.31) into (3.30), we get

$$|\phi_{i,j}| \approx |\hat{\boldsymbol{M}}_j - \hat{\boldsymbol{M}}_i| \approx |\,(\boldsymbol{r}_{ij} \cdot \boldsymbol{\nabla})\,\hat{\boldsymbol{M}}_i\,| \quad , \tag{3.32}$$

and equation (3.29) becomes

$$E_{\mathrm{ex}} = \frac{1}{2}\mathcal{J}S^2 \sum_{\text{neighbouring } i,j} \Big[\,(\boldsymbol{r}_{ij} \cdot \boldsymbol{\nabla})\,\hat{\boldsymbol{M}}_i\,\Big]^2 \quad . \tag{3.33}$$

This summation includes each pair of particles twice. Alternatively, the summation can consider each interacting pair once, and a factor of 2 compensates for this:

$$E_{\mathrm{ex}} = \mathcal{J}S^2 \sum_i \sum_{\text{neighbouring } j} \Big[\,(\boldsymbol{r}_{ij} \cdot \boldsymbol{\nabla})\,\hat{\boldsymbol{M}}_i\,\Big]^2 \quad . \tag{3.34}$$

Making use of the acronym $\partial_{\mathrm{x,y,z}} = \frac{\partial}{\partial \mathrm{x,y,z}}$, the addend $\Big[\,(\boldsymbol{r}_{ij} \cdot \boldsymbol{\nabla})\,\hat{\boldsymbol{M}}_i\,\Big]^2$ is expanded:

$$\begin{pmatrix} r_{ij,\mathrm{x}}\partial_{\mathrm{x}}\hat{M}_{i,\mathrm{x}} + r_{ij,\mathrm{y}}\partial_{\mathrm{y}}\hat{M}_{i,\mathrm{x}} + r_{ij,\mathrm{z}}\partial_{\mathrm{z}}\hat{M}_{i,\mathrm{x}} \\ r_{ij,\mathrm{x}}\partial_{\mathrm{x}}\hat{M}_{i,\mathrm{y}} + r_{ij,\mathrm{y}}\partial_{\mathrm{y}}\hat{M}_{i,\mathrm{y}} + r_{ij,\mathrm{z}}\partial_{\mathrm{z}}\hat{M}_{i,\mathrm{y}} \\ r_{ij,\mathrm{x}}\partial_{\mathrm{x}}\hat{M}_{i,\mathrm{z}} + r_{ij,\mathrm{y}}\partial_{\mathrm{y}}\hat{M}_{i,\mathrm{z}} + r_{ij,\mathrm{z}}\partial_{\mathrm{z}}\hat{M}_{i,\mathrm{z}} \end{pmatrix} \cdot \begin{pmatrix} r_{ij,\mathrm{x}}\partial_{\mathrm{x}}\hat{M}_{i,\mathrm{x}} + r_{ij,\mathrm{y}}\partial_{\mathrm{y}}\hat{M}_{i,\mathrm{x}} + r_{ij,\mathrm{z}}\partial_{\mathrm{z}}\hat{M}_{i,\mathrm{x}} \\ r_{ij,\mathrm{x}}\partial_{\mathrm{x}}\hat{M}_{i,\mathrm{y}} + r_{ij,\mathrm{y}}\partial_{\mathrm{y}}\hat{M}_{i,\mathrm{y}} + r_{ij,\mathrm{z}}\partial_{\mathrm{z}}\hat{M}_{i,\mathrm{y}} \\ r_{ij,\mathrm{x}}\partial_{\mathrm{x}}\hat{M}_{i,\mathrm{z}} + r_{ij,\mathrm{y}}\partial_{\mathrm{y}}\hat{M}_{i,\mathrm{z}} + r_{ij,\mathrm{z}}\partial_{\mathrm{z}}\hat{M}_{i,\mathrm{z}} \end{pmatrix}$$

$$\begin{aligned} = \quad & r_{ij,\mathrm{x}}^2(\partial_{\mathrm{x}}\hat{M}_{i,\mathrm{x}})^2 + r_{ij,\mathrm{y}}^2(\partial_{\mathrm{y}}\hat{M}_{i,\mathrm{x}})^2 + r_{ij,\mathrm{z}}^2(\partial_{\mathrm{z}}\hat{M}_{i,\mathrm{x}})^2 \\ & + 2r_{ij,\mathrm{x}}r_{ij,\mathrm{y}}\partial_{\mathrm{x}}\hat{M}_{i,\mathrm{x}}\partial_{\mathrm{y}}\hat{M}_{i,\mathrm{x}} + 2r_{ij,\mathrm{x}}r_{ij,\mathrm{z}}\partial_{\mathrm{x}}\hat{M}_{i,\mathrm{x}}\partial_{\mathrm{z}}\hat{M}_{i,\mathrm{x}} + 2r_{ij,\mathrm{y}}r_{ij,\mathrm{z}}\partial_{\mathrm{y}}\hat{M}_{i,\mathrm{x}}\partial_{\mathrm{z}}\hat{M}_{i,\mathrm{x}} \\ & + r_{ij,\mathrm{x}}^2(\partial_{\mathrm{x}}\hat{M}_{i,\mathrm{y}})^2 + r_{ij,\mathrm{y}}^2(\partial_{\mathrm{y}}\hat{M}_{i,\mathrm{y}})^2 + r_{ij,\mathrm{z}}^2(\partial_{\mathrm{z}}\hat{M}_{i,\mathrm{y}})^2 \\ & + 2r_{ij,\mathrm{x}}r_{ij,\mathrm{y}}\partial_{\mathrm{x}}\hat{M}_{i,\mathrm{y}}\partial_{\mathrm{y}}\hat{M}_{i,\mathrm{y}} + 2r_{ij,\mathrm{x}}r_{ij,\mathrm{z}}\partial_{\mathrm{x}}\hat{M}_{i,\mathrm{y}}\partial_{\mathrm{z}}\hat{M}_{i,\mathrm{y}} + 2r_{ij,\mathrm{y}}r_{ij,\mathrm{z}}\partial_{\mathrm{y}}\hat{M}_{i,\mathrm{y}}\partial_{\mathrm{z}}\hat{M}_{i,\mathrm{y}} \\ & + r_{ij,\mathrm{x}}^2(\partial_{\mathrm{x}}\hat{M}_{i,\mathrm{z}})^2 + r_{ij,\mathrm{y}}^2(\partial_{\mathrm{y}}\hat{M}_{i,\mathrm{z}})^2 + r_{ij,\mathrm{z}}^2(\partial_{\mathrm{z}}\hat{M}_{i,\mathrm{z}})^2 \\ & + \quad 2r_{ij,\mathrm{x}}r_{ij,\mathrm{y}}\partial_{\mathrm{x}}\hat{M}_{i,\mathrm{z}}\partial_{\mathrm{y}}\hat{M}_{i,\mathrm{z}} + 2r_{ij,\mathrm{x}}r_{ij,\mathrm{z}}\partial_{\mathrm{x}}\hat{M}_{i,\mathrm{z}}\partial_{\mathrm{z}}\hat{M}_{i,\mathrm{z}} + 2r_{ij,\mathrm{y}}r_{ij,\mathrm{z}}\partial_{\mathrm{y}}\hat{M}_{i,\mathrm{z}}\partial_{\mathrm{z}}\hat{M}_{i,\mathrm{z}} \quad . \end{aligned} \tag{3.35}$$

In order to proceed with explicit calculations, we assume a specific grid type, in this case a simple cubic lattice. Each grid point i has six next neighbours j which

are located at the relative positions $\boldsymbol{r}_{ij}$

$$\boldsymbol{r}_{i1} = \begin{pmatrix} a \\ 0 \\ 0 \end{pmatrix} \quad , \boldsymbol{r}_{i2} = \begin{pmatrix} -a \\ 0 \\ 0 \end{pmatrix} \quad , \boldsymbol{r}_{i3} = \begin{pmatrix} 0 \\ a \\ 0 \end{pmatrix} \quad ,$$
$$\boldsymbol{r}_{i4} = \begin{pmatrix} 0 \\ -a \\ 0 \end{pmatrix} \quad , \boldsymbol{r}_{i5} = \begin{pmatrix} 0 \\ 0 \\ a \end{pmatrix} \quad , \boldsymbol{r}_{i6} = \begin{pmatrix} 0 \\ 0 \\ -a \end{pmatrix} \quad , \tag{3.36}$$

where a is the nearest neighbour distance. With this choice of $\boldsymbol{r}_{ij}$, all the mixed terms in (3.35) vanish, and only the square terms are left. Applying (3.36) and (3.35) to (3.34) finally results in

$$\begin{aligned} E_{\mathrm{ex}} &= 2\,a^2\,\mathcal{J}S^2 \sum_i \Big[(\partial_{\mathrm{x}}\hat{M}_{i,\mathrm{x}})^2 + (\partial_{\mathrm{y}}\hat{M}_{i,\mathrm{x}})^2 + (\partial_{\mathrm{z}}\hat{M}_{i,\mathrm{x}})^2 \\ &\quad + (\partial_{\mathrm{x}}\hat{M}_{i,\mathrm{y}})^2 + (\partial_{\mathrm{y}}\hat{M}_{i,\mathrm{y}})^2 + (\partial_{\mathrm{z}}\hat{M}_{i,\mathrm{y}})^2 \\ &\quad + (\partial_{\mathrm{x}}\hat{M}_{i,\mathrm{z}})^2 + (\partial_{\mathrm{y}}\hat{M}_{i,\mathrm{z}})^2 + (\partial_{\mathrm{z}}\hat{M}_{i,\mathrm{z}})^2 \Big] \\ &= 2\,a^2\,\mathcal{J}S^2 \sum_i \Big[(\boldsymbol{\nabla}\hat{M}_{i,\mathrm{x}})^2 + (\boldsymbol{\nabla}\hat{M}_{i,\mathrm{y}})^2 + (\boldsymbol{\nabla}\hat{M}_{i,\mathrm{z}})^2 \Big] \quad . \end{aligned} \tag{3.37}$$

For different lattice types, the derivation works accordingly, but one has to take into consideration additional next neighbours with different $\boldsymbol{r}_{ij}$. By using a lattice parameter z denoting the number of particles entirely assigned to one crystal unit cell, the generalised form of (3.37) is

$$E_{\mathrm{ex}} = 2\,a^2\,z\mathcal{J}S^2 \sum_i \Big[(\boldsymbol{\nabla}\hat{M}_{i,\mathrm{x}})^2 + (\boldsymbol{\nabla}\hat{M}_{i,\mathrm{y}})^2 + (\boldsymbol{\nabla}\hat{M}_{i,\mathrm{z}})^2 \Big] \quad . \tag{3.38}$$

A simple cubic lattice implies $z = 1$, a body-centred cubic lattice $z = 2$, a face-centred cubic lattice $z = 4$. In the continuum limit, the summation is replaced by an integral with an integration volume cell a^3. This leads to

$$E_{\mathrm{ex}} = \frac{C}{2} \int_V \Big[(\boldsymbol{\nabla}\hat{M}_{\mathrm{x}})^2 + (\boldsymbol{\nabla}\hat{M}_{\mathrm{y}})^2 + (\boldsymbol{\nabla}\hat{M}_{\mathrm{z}})^2 \Big] \,\mathrm{d}V \tag{3.39}$$

$$= \frac{C}{2} \int_V (\boldsymbol{\nabla} \cdot \hat{\boldsymbol{M}})^2 \,\mathrm{d}V \quad , \tag{3.40}$$

where C is the exchange constant, given by

$$C = 2\mathcal{J}S^2 \frac{z}{a} \quad . \tag{3.41}$$

Occasionally, an alternative exchange constant A is used with $A = 2\,C$. Both A and C are associated with the unit Joule/meter (J/m), and are of the order of magnitude 10^{-11} to 10^{-13}J/m.

3.2.3 Discretised formulation

We now derive a discretised form of the exchange energy equation (3.39) that is suitable for usage in finite difference simulations, as it takes regard to the underlying computational lattice (*Donahue and Porter*, 2004). The resulting equation is implemented in the *OOMMF* code, one of the standard micromagnetic simulation packages (*Donahue and Porter*, 2003, 1999).

The transformations in section 3.2.2 started with an atomistic view on the crystal lattice, and then derived equations for a continuous material. For the finite difference method, this strategy is inverted, projecting the continuous formulation onto an artificial computational cubic lattice for discretisation. It is important to understand that the finite difference lattice is of a completely different nature than the crystal lattice, and that the respective lattice constants do not comply.

We start with equation (3.39). From the product rule of differential calculus for products with differentiable functions f and g, $(fg)' = f'g + fg'$, we find that

$$(\boldsymbol{\nabla} f) \cdot (\boldsymbol{\nabla} f) \;=\; \boldsymbol{\nabla} \cdot (f \boldsymbol{\nabla} f) - f \triangle f \tag{3.42}$$

with $g = \boldsymbol{\nabla} f$. Applying this to equation (3.39) results in

$$\begin{aligned}
E_{\mathrm{ex}} = A \int_V \Big[\;& \boldsymbol{\nabla} \cdot (\hat{M}_{\mathrm{x}} \boldsymbol{\nabla} \hat{M}_{\mathrm{x}}) - \hat{M}_{\mathrm{x}} \triangle \hat{M}_{\mathrm{x}} + \\
& \boldsymbol{\nabla} \cdot (\hat{M}_{\mathrm{y}} \boldsymbol{\nabla} \hat{M}_{\mathrm{y}}) - \hat{M}_{\mathrm{y}} \triangle \hat{M}_{\mathrm{y}} + \\
& \boldsymbol{\nabla} \cdot (\hat{M}_{\mathrm{z}} \boldsymbol{\nabla} \hat{M}_{\mathrm{z}}) - \hat{M}_{\mathrm{z}} \triangle \hat{M}_{\mathrm{z}} \Big] \, \mathrm{d}V \\
= A \int_V \Big[\;& \boldsymbol{\nabla} \cdot (\hat{M}_{\mathrm{x}} \boldsymbol{\nabla} \hat{M}_{\mathrm{x}} + \hat{M}_{\mathrm{y}} \boldsymbol{\nabla} \hat{M}_{\mathrm{y}} + \hat{M}_{\mathrm{z}} \boldsymbol{\nabla} \hat{M}_{\mathrm{z}}) - \hat{\boldsymbol{M}} (\triangle \hat{\boldsymbol{M}}) \Big] \, \mathrm{d}V \\
= A \int_V \Big[\;& \boldsymbol{\nabla} \cdot \begin{pmatrix}
\hat{M}_{\mathrm{x}} \partial_{\mathrm{x}} \hat{M}_{\mathrm{x}} + \hat{M}_{\mathrm{y}} \partial_{\mathrm{x}} \hat{M}_{\mathrm{y}} + \hat{M}_{\mathrm{z}} \partial_{\mathrm{x}} \hat{M}_{\mathrm{z}} \\
\hat{M}_{\mathrm{x}} \partial_{\mathrm{y}} \hat{M}_{\mathrm{x}} + \hat{M}_{\mathrm{y}} \partial_{\mathrm{y}} \hat{M}_{\mathrm{y}} + \hat{M}_{\mathrm{z}} \partial_{\mathrm{y}} \hat{M}_{\mathrm{z}} \\
\hat{M}_{\mathrm{x}} \partial_{\mathrm{z}} \hat{M}_{\mathrm{x}} + \hat{M}_{\mathrm{y}} \partial_{\mathrm{z}} \hat{M}_{\mathrm{y}} + \hat{M}_{\mathrm{z}} \partial_{\mathrm{z}} \hat{M}_{\mathrm{z}}
\end{pmatrix} \\
& - \hat{\boldsymbol{M}} \cdot (\triangle \hat{\boldsymbol{M}}) \Big] \, \mathrm{d}V \quad .
\end{aligned} \tag{3.43}$$

From the normalisation of $\hat{\boldsymbol{M}}$, it follows that $\hat{\boldsymbol{M}} \cdot \partial_{\mathrm{x}} \hat{\boldsymbol{M}} = 0$, and correspondingly for y and z:

$$\begin{aligned}
\hat{M}_{\mathrm{x}} \partial_{\mathrm{x}} \hat{M}_{\mathrm{x}} + \hat{M}_{\mathrm{y}} \partial_{\mathrm{x}} \hat{M}_{\mathrm{y}} + \hat{M}_{\mathrm{z}} \partial_{\mathrm{x}} \hat{M}_{\mathrm{z}} &= 0 \\
\hat{M}_{\mathrm{x}} \partial_{\mathrm{y}} \hat{M}_{\mathrm{x}} + \hat{M}_{\mathrm{y}} \partial_{\mathrm{y}} \hat{M}_{\mathrm{y}} + \hat{M}_{\mathrm{z}} \partial_{\mathrm{y}} \hat{M}_{\mathrm{z}} &= 0 \\
\hat{M}_{\mathrm{x}} \partial_{\mathrm{z}} \hat{M}_{\mathrm{x}} + \hat{M}_{\mathrm{y}} \partial_{\mathrm{z}} \hat{M}_{\mathrm{y}} + \hat{M}_{\mathrm{z}} \partial_{\mathrm{z}} \hat{M}_{\mathrm{z}} &= 0 \quad .
\end{aligned} \tag{3.44}$$

We expand the last term of equation (3.43),

$$\begin{aligned}\hat{\boldsymbol{M}} \cdot (\triangle \hat{\boldsymbol{M}}) &= \hat{M}_\mathrm{x}\partial_\mathrm{x}^2\hat{M}_\mathrm{x} + \hat{M}_\mathrm{x}\partial_\mathrm{y}^2\hat{M}_\mathrm{x} + \hat{M}_\mathrm{x}\partial_\mathrm{z}^2\hat{M}_\mathrm{x} + \\ &\quad \hat{M}_\mathrm{y}\partial_\mathrm{x}^2\hat{M}_\mathrm{y} + \hat{M}_\mathrm{y}\partial_\mathrm{y}^2\hat{M}_\mathrm{y} + \hat{M}_\mathrm{y}\partial_\mathrm{z}^2\hat{M}_\mathrm{y} + \\ &\quad \hat{M}_\mathrm{z}\partial_\mathrm{x}^2\hat{M}_\mathrm{z} + \hat{M}_\mathrm{z}\partial_\mathrm{y}^2\hat{M}_\mathrm{z} + \hat{M}_\mathrm{z}\partial_\mathrm{z}^2\hat{M}_\mathrm{z} \\ &= \hat{\boldsymbol{M}} \cdot \partial_\mathrm{x}^2\hat{\boldsymbol{M}} + \hat{\boldsymbol{M}} \cdot \partial_\mathrm{y}^2\hat{\boldsymbol{M}} + \hat{\boldsymbol{M}} \cdot \partial_\mathrm{z}^2\hat{\boldsymbol{M}} \quad . \end{aligned} \tag{3.45}$$

Using equations (3.44) and (3.45), equation (3.43) takes on the form

$$E_\mathrm{ex} = -A \int_V \hat{\boldsymbol{M}} \cdot \left[\partial_\mathrm{x}^2\hat{\boldsymbol{M}} + \partial_\mathrm{y}^2\hat{\boldsymbol{M}} + \partial_\mathrm{z}^2\hat{\boldsymbol{M}} \right] \mathrm{d}V \quad . \tag{3.46}$$

This integral is now approximated by standard methods of numerics. Generally, a one-dimensional integral of a function $f(x)$ from a to b can be approximated by a discrete sum:

$$\int_a^b f(x)\mathrm{d}x = h\sum_{i=1}^{n} \omega_i f_i + O(h^\alpha) \quad , \tag{3.47}$$

with sample points $x_i = a + (i - \frac{1}{2})h$ of equidistant spacing $h = (b-a)/n$ and $f_i = f(x_i)$ (*Bronstein and Semendjajew*, 1989, p. 762). The choice of the sample point weights ω_i determines the convergence order α of the sum. For a three-dimensional integral, the approximation is

$$\int_V f(x)\mathrm{d}V = h^3 \sum_{ijk=1}^{mno} \omega_i^\mathrm{x}\omega_j^\mathrm{y}\omega_k^\mathrm{z} f_{ijk} + O(h^\alpha) \quad , \tag{3.48}$$

with weights ω_i^x, ω_j^y, ω_k^z along the x, y, z axes, and $f_{ijk} = f(x_i, y_j, z_k)$. Application to the first term of equation (3.46) results in

$$E_\mathrm{ex,x} = -h^3 A \sum_{jk} \omega_j^\mathrm{y}\omega_k^\mathrm{z} \sum_{ii'} \omega_i^\mathrm{x} d_{ii'} \hat{\boldsymbol{M}}_{ijk} \cdot \hat{\boldsymbol{M}}_{i'jk} + O(h^\alpha) \quad , \tag{3.49}$$

where $d_{ii'}$ is a discrete representation for the operator ∂_x^2 and $\hat{\boldsymbol{M}}_{ijk} = \hat{\boldsymbol{M}}(x_i, y_j, z_k)$. We use a simple second order ($\alpha = 2$) scheme where all ω equal 1 (trapezoidal rule). Furthermore, we apply a second-order central difference scheme for the second derivative in x,

$$\begin{aligned} f''_{ijk} &= \frac{f_{(i-1)jk} - 2f_{ijk} + f_{(i+1)jk}}{h^2} + O(h^2) \\ &= \sum_{i' \in (i-1, i+1)} \frac{f_{i'jk} - f_{ijk}}{h^2} + O(h^2) \quad , \end{aligned} \tag{3.50}$$

and we get

$$\begin{aligned} E_{\mathrm{ex,x}} &= -hA \sum_{ijk} \sum_{i' \in (i-1,i+1)} \hat{\boldsymbol{M}}_{ijk} \cdot (\hat{\boldsymbol{M}}_{i'jk} - \hat{\boldsymbol{M}}_{ijk}) \\ &= hA \sum_{ijk} \sum_{i' \in (i-1,i+1)} (\hat{\boldsymbol{M}}_{ijk} \cdot \hat{\boldsymbol{M}}_{i'jk} - 1) \quad . \end{aligned} \tag{3.51}$$

Proceeding accordingly with the ∂_{y}^2 and ∂_{z}^2 terms of equation (3.46), the discretised exchange energy equation finally is

$$E_{\mathrm{ex}} = hA \sum_{\eta} \sum_{\eta'} (\hat{\boldsymbol{M}}_{\eta} \cdot \hat{\boldsymbol{M}}_{\eta'} - 1) \quad , \tag{3.52}$$

with η running over all cells in the computational domain, and η' being the list of next neighbours of η.

3.3 Anisotropy energy

When a physical property of a material is a directional function, this property is said to exhibit anisotropy. The preference for the magnetisation to lie in a particular direction of a sample is called *magnetic anisotropy*. There are different kind of anisotropies in the context of magnetism: magnetocrystalline, strain induced, shape, and surface anisotropy. One anisotropy considered here, the magnetocrystalline anisotropy, has its origin in the crystal symmetry of the sample and the $\boldsymbol{LS}$ coupling (or spin-orbit coupling) of the electron angular momenta: the crystallographic structure influences the shape and orientation of the electron orbits. These, in turn, affect the electron spins via the $\boldsymbol{LS}$ coupling in a way that the spins tend to align along the crystallographic axes. Different sample materials with different crystal symmetries show different anisotropy types. The anisotropy types are now discussed (*O'Handley*, 1999).

3.3.1 Phenomenology of anisotropy

Experiments reveal the character of the anisotropy for different materials: when an external field is used to magnetise a probe, the magnetisation process depends on the angle between the applied field and a crystal reference direction. *E.g.* in iron, the magnetisation process is said to be easy in the $[100]$ direction (along the edge of the crystal cell), and hard in the $[111]$ direction (along the body diagonal of the crystal cell); that is, the field needed to magnetise iron to saturation is smaller in $[100]$ than in any other direction (figure 3.1 on the following page).

The anisotropy energy density ε_{a} is defined as the energy density difference required to saturate a sample (saturation magnetisation M_{s}) alongside a given

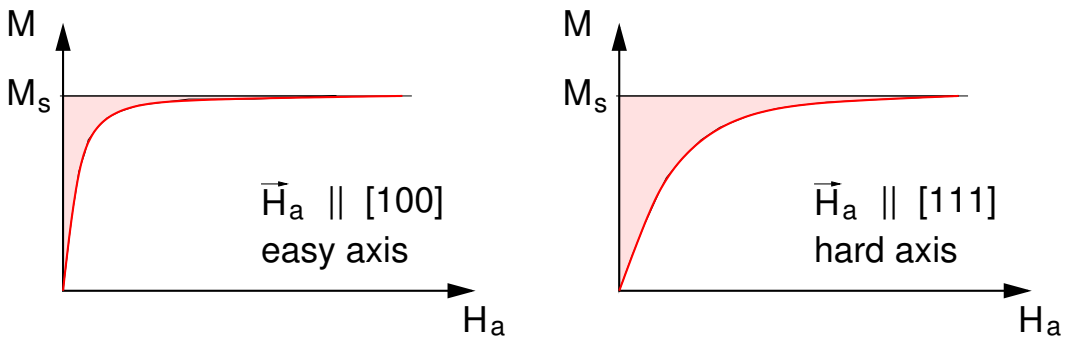

Figure 3.1: Schematic hysteresis loops of a material with an easy axis in [100] and a hard axis in [111], *e.g.* iron. The left plot shows the function of the magnetisation M over the applied field H_a along the easy axis, the right plot along the hard axis. The shaded area in each plot indicates the energy required to magnetise the sample up to saturation.

direction and alongside the hard axis (shaded areas in the plots of figure 3.1),

$$\begin{aligned} \varepsilon_\mathrm{a} &= \mu_0 \int_0^{M_\mathrm{s}} \boldsymbol{H}_\mathrm{a}^\mathrm{hard}(\boldsymbol{M})\,\mathrm{d}\boldsymbol{M} - \mu_0 \int_0^{M_\mathrm{s}} \boldsymbol{H}_\mathrm{a}^\mathrm{any}(\boldsymbol{M})\,\mathrm{d}\boldsymbol{M} \\ &= -\mu_0 \int_0^{M_\mathrm{s}} \boldsymbol{H}_\mathrm{a}^\mathrm{any}(\boldsymbol{M})\,\mathrm{d}\boldsymbol{M} \quad . \end{aligned} \tag{3.53}$$

For the second equation, the energy is scaled in such a way that the saturation energy along the hard axis is zero. The field $\boldsymbol{H}_\mathbf{a}$ in this formulation is a function of a given magnetisation. As we only consider anisotropy energy contributions here, this field is called the anisotropy field. It can be determined by

$$\boldsymbol{H}_\mathrm{a} = -\frac{1}{\mu_0}\frac{\partial \varepsilon_\mathrm{a}}{\partial \boldsymbol{M}} = -\frac{1}{\mu_0}\boldsymbol{\nabla}_{\boldsymbol{M}}\varepsilon_\mathrm{a} \quad . \tag{3.54}$$

For specific crystal symmetries, equations for the anisotropy energy and field are now derived for usage in numerical computation codes.

3.3.2 Uniaxial anisotropy

The simplest case is a uniaxial anisotropy, as observed in cobalt: magnetic measurements for different directions suggest the existence of an axis that minimises the anisotropy energy. Plotting the anisotropy energy as a function of the angle θ enclosed by this easy axis (defined as the z axis, without loss of generality) and the magnetisation, shows a onefold symmetry (figure 3.2a). The anisotropy energy does not depend on the azimuthal angle ϕ in this system, and it is maximal in the basal plane ($\theta = 90°$), the hard plane. A 3D plot of the uniaxial anisotropy energy is depicted in figure 3.2b.

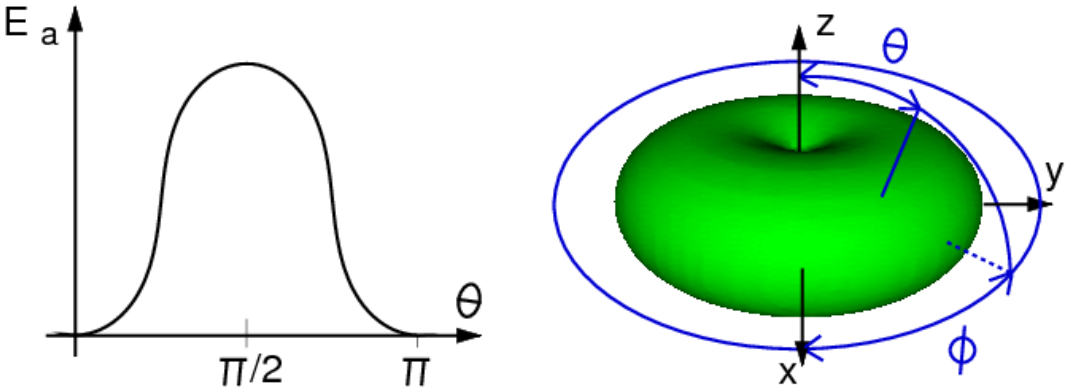

Figure 3.2: Sketches of the anisotropy energy, as a 2D plot over θ (left), and as a 3D parametric plot (right), with an easy axis along $\pm$ z.

We now find an expression for the uniaxial anisotropy energy density as a function of θ. The most general approach is a Fourier series with coefficients K_n^{s} and K_n^{c} of the form

$$\varepsilon_{\mathrm{a}} = -\sum_{n=0}^{\infty} K_n^{\mathrm{s}} \sin^n(\theta) - \sum_{n=0}^{\infty} K_n^{\mathrm{c}} \cos^n(\theta) \quad . \tag{3.55}$$

Taking into account the onefold symmetry evident in the measurements of uniaxial anisotropy, all odd powers of $\sin(\theta)$ and $\cos(\theta)$ in the Fourier series can be dropped. Of the remaining terms, the $\sin^{2n}(\theta)$ are expressed by $\cos^{2m}(\theta)$ ($m \leq n$) plus irrelevant constants, as in $\sin^2(\theta) = 1 - \cos^2(\theta)$. After discarding the constant terms and recollecting the coefficients K_n^{c} into K_n, we get

$$\varepsilon_{\mathrm{a}} = -\sum_{n=1}^{\infty} K_n \cos^{2n}(\theta) \quad . \tag{3.56}$$

Positive coefficients K_n correspond to an easy axis and a hard basal plane. This is a consequence of the minus signs in equation (3.55), and sometimes used differently in literature.

For most applications, the first term $\cos^2(\theta)$ is sufficient. However, some spherical problems require an additional order, so that the following approximation includes fourth-order terms:

$$\varepsilon_{\mathrm{a}} = -K_1 \cos^2(\theta) - K_2 \cos^4(\theta) \quad . \tag{3.57}$$

With $\hat{\boldsymbol{e}}$ being the normalised vector in the direction of the anisotropy field, and $\hat{\boldsymbol{M}}$ being the normalised vector in the direction of the magnetisation,

$$\boldsymbol{H}_{\mathrm{a}} = H_{\mathrm{a}} \hat{\boldsymbol{e}} \tag{3.58}$$

$$\boldsymbol{M} = M \hat{\boldsymbol{M}} \quad , \tag{3.59}$$

the equation reads

$$\varepsilon_{\mathrm{a}} = -K_1|\hat{\boldsymbol{e}}\cdot\hat{\boldsymbol{M}}|^2 - K_2 \mid \hat{\boldsymbol{e}}\cdot\hat{\boldsymbol{M}} \mid^4 \quad . \tag{3.60}$$

If fourth-order terms are ignored (*i.e.* $K_2 = 0$), we have

$$\varepsilon_{\mathrm{a}} = -K_1|\hat{\boldsymbol{e}}\cdot\hat{\boldsymbol{M}}|^2 \quad . \tag{3.61}$$

For numerical purposes, an alternative form of the fourth-order approximation (3.60) is advantageous at times, obtained from (3.57) via

$$\begin{aligned}
|\hat{\boldsymbol{e}}\times\hat{\boldsymbol{M}}|^2 &= |\hat{\boldsymbol{e}}|^2|\hat{\boldsymbol{M}}|^2\sin^2(\theta) = \sin^2(\theta) = 1-\cos^2(\theta) && (3.62)\\
|\hat{\boldsymbol{e}}\times\hat{\boldsymbol{M}}|^4 &= \left(1-\cos^2(\theta)\right)^2 = 1+\cos^4(\theta)-2\cos^2(\theta) && (3.63)\\
\cos^4(\theta) &= |\hat{\boldsymbol{e}}\times\hat{\boldsymbol{M}}|^4 - 2|\hat{\boldsymbol{e}}\times\hat{\boldsymbol{M}}|^2 + 1 \quad , && (3.64)
\end{aligned}$$

and dropping constant terms:

$$\varepsilon_{\mathrm{a}} = (K_1+2K_2)\,|\hat{\boldsymbol{e}}\times\hat{\boldsymbol{M}}|^2 - K_2|\hat{\boldsymbol{e}}\times\hat{\boldsymbol{M}}|^4 \quad , \tag{3.65}$$

or, with second-order terms only (*i.e.* $K_2 = 0$),

$$\varepsilon_{\mathrm{a}} = K_1|\hat{\boldsymbol{e}}\times\hat{\boldsymbol{M}}|^2 \quad . \tag{3.66}$$

Next, we derive the anisotropy field which corresponds to this anisotropy energy (3.60). Therefore, equation (3.54) is used. To calculate the gradient of the energy, the previous assumption is recalled that aligned the anisotropy in the z direction without loss of generality:

$$|\hat{\boldsymbol{e}}\cdot\hat{\boldsymbol{M}}| = \frac{1}{M}|\hat{\boldsymbol{e}}\cdot\boldsymbol{M}| = \frac{1}{M}M_{\mathrm{z}} \quad , \tag{3.67}$$

and the field components are

$$\begin{aligned}
H_{\mathrm{a,x}} &= -\frac{1}{\mu_0}\frac{\partial\varepsilon_{\mathrm{a}}}{\partial M_{\mathrm{x}}} = 0 && (3.68)\\
H_{\mathrm{a,y}} &= -\frac{1}{\mu_0}\frac{\partial\varepsilon_{\mathrm{a}}}{\partial M_{\mathrm{y}}} = 0 && (3.69)\\
H_{\mathrm{a,z}} &= -\frac{1}{\mu_0}\frac{\partial\varepsilon_{\mathrm{a}}}{\partial M_{\mathrm{z}}}\\
&= 2\frac{K_1}{\mu_0 M^2}M_{\mathrm{z}} + 4\frac{K_2}{\mu_0 M^4}M_{\mathrm{z}}^3\\
&= 2\frac{K_1}{\mu_0 M}|\hat{\boldsymbol{e}}\cdot\hat{\boldsymbol{M}}| + 4\frac{K_2}{\mu_0 M}|\hat{\boldsymbol{e}}\cdot\hat{\boldsymbol{M}}|^3 = |\boldsymbol{H}_{\mathrm{a}}| = H_{\mathrm{a}} \quad . && (3.70)
\end{aligned}$$

This is in compliance with the fact that $\boldsymbol{H}_{\mathrm{a}}$ was chosen to be in the direction of the

anisotropy, and of the z axis (3.58):

$$\boldsymbol{H}_{\mathrm{a}} = \left(2\frac{K_1}{\mu_0 M}|\hat{\boldsymbol{e}} \cdot \hat{\boldsymbol{M}}| + 4\frac{K_2}{\mu_0 M}|\hat{\boldsymbol{e}} \cdot \hat{\boldsymbol{M}}|^3 \right) \hat{\boldsymbol{e}} \quad . \tag{3.71}$$

If fourth-order terms are ignored (i.e. $K_2 = 0$), the length H_{a} is approximated by

$$H_{\mathrm{a}} = 2\frac{K_1}{\mu_0 M}|\hat{\boldsymbol{e}} \cdot \hat{\boldsymbol{M}}| \quad , \tag{3.72}$$

so that

$$\boldsymbol{H}_{\mathrm{a}} = 2\frac{K_1}{\mu_0 M}|\hat{\boldsymbol{e}} \cdot \hat{\boldsymbol{M}}|\, \hat{\boldsymbol{e}} \quad . \tag{3.73}$$

The fourth-order terms are important for cases with two uniaxial anisotropies in perpendicular directions. Then, the second-order terms for the two directions compensate each other, so that the resulting second-order anisotropy is a constant energy term of irrelevance. An angular dependence of the resulting anisotropy is obtained only by inclusion of fourth-order terms.

3.3.3 Cubic anisotropy

Most materials, *e.g.* iron and nickel, do not feature the simple and easy-to-handle uniaxial anisotropy due to the nature of their crystal lattice structure. Experiments reveal that these materials bear a cubic anisotropy. Here, the energy depends on the three angles γ_1, γ_2, γ_3 (see figure 3.4 on page 33) rather than one angle θ. Measurements of the anisotropy in the basal plane show a fourfold symmetry (figure 3.3, left), with either an easy axis for $\phi = 0°$ (*e.g.* iron, 3.3a)), or a hard axis (*e.g.* nickel, 3.3b)). A complete 3D mapping of the anisotropy provides a function as shown on the right side of figure 3.3: the easy axes of iron are the crystal cell base directions, the easy axes of nickel the crystal cell body diagonals.

The symmetry axes of the cubic anisotropy are chosen to be aligned with the basis of the coordinate system $(\hat{\boldsymbol{e}}_i)$, $i \in \{1, 2, 3\}$, without loss of generality, so that

$$\gamma_i = \sphericalangle(\hat{\boldsymbol{e}}_i, \hat{\boldsymbol{M}}) \quad . \tag{3.74}$$

The angle cosines $\alpha_i = \cos\gamma_i$ (see figure 3.4) are the projections of a unit vector onto the corresponding coordinate axes. The correlation to the Cartesian and spherical coordinates is

$$\begin{aligned} \alpha_1 &= \cos\gamma_1 = \hat{M}_{\mathrm{x}} = \cos\phi\, \sin\theta \\ \alpha_2 &= \cos\gamma_2 = \hat{M}_{\mathrm{y}} = \sin\phi\, \sin\theta \\ \alpha_3 &= \cos\gamma_3 = \hat{M}_{\mathrm{z}} = \cos\theta \qquad . \end{aligned} \tag{3.75}$$

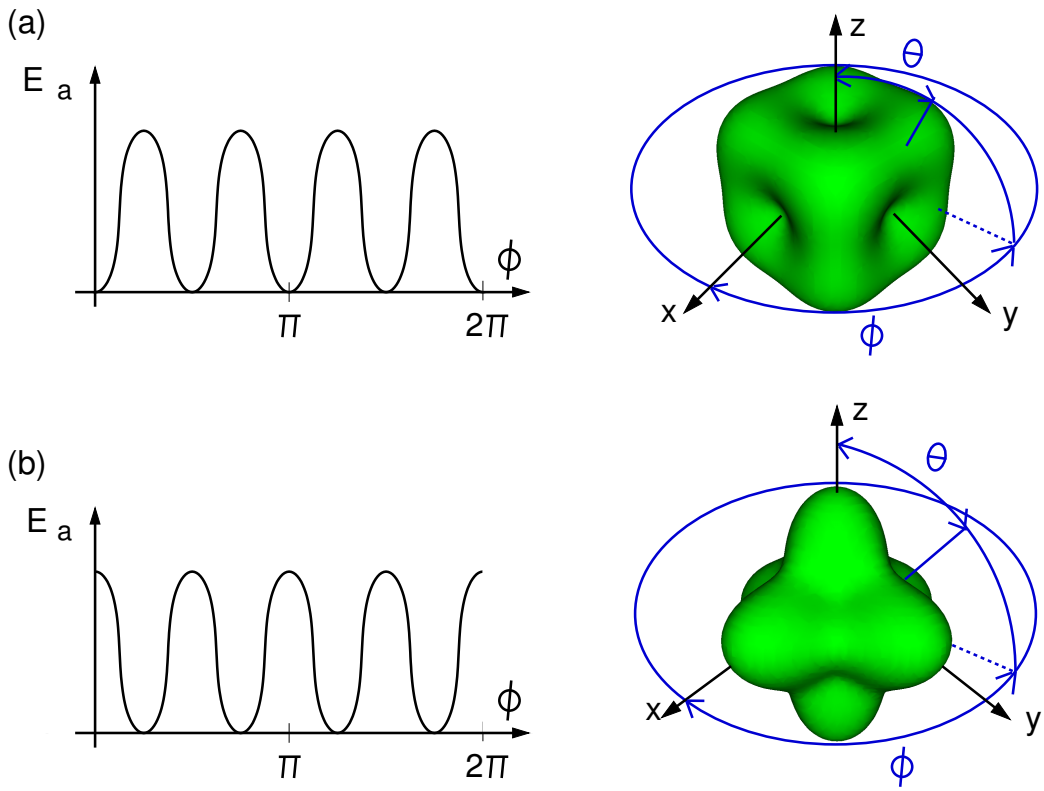

Figure 3.3: Schematic result of an in-plane measurement of the anisotropy energy as a function of the azimuthal angle ϕ (left), and a 3D parametric plot of the anisotropy energy (right) for the materials Fe (a) and Ni (b).

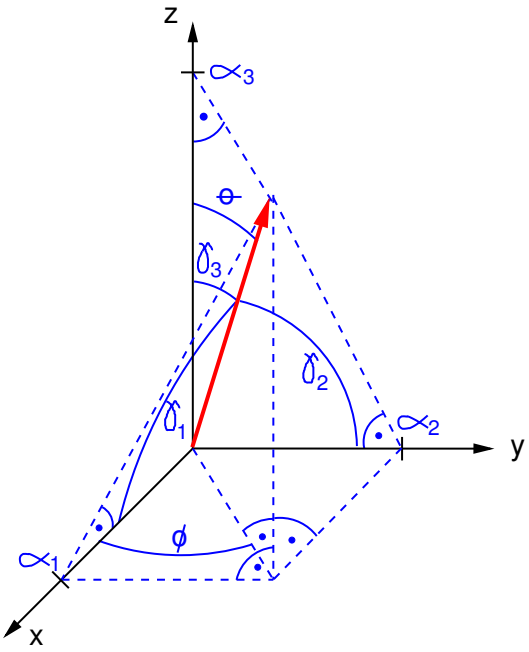

Figure 3.4: Definition of α_i in a Cartesian coordinate system (black): the α_i are the projection lengths of a unit vector (red) onto the coordinate axes. The angles enclosing the unit vector and the coordinate axes are named γ_i. The spherical coordinates ϕ and θ are depicted as well. Projection lines and angles are displayed in blue colour.

The energy density is expressed in terms of linear combinations of powers of the α_i:

$$\varepsilon_\mathrm{a} = \sum_{i=0}^{\infty}\sum_{j=0}^{\infty}\sum_{k=0}^{\infty} K_{i+j+k}\,\alpha_1^i\,\alpha_2^j\,\alpha_3^k \quad . \tag{3.76}$$

Many of the contributing terms vanish due to the symmetries involved (*O'Handley*, 1999, p. 214):

- cyclic permutation
- mirror reflection
- rotation
- time reversal invariance.

As usual, constant energy terms are ignored. The remaining terms up to eighth order are

$$\begin{aligned}\varepsilon_\mathrm{a} = \quad & K_1\left(\alpha_1^2\alpha_2^2+\alpha_1^2\alpha_3^2+\alpha_2^2\alpha_3^2\right)+K_2\left(\alpha_1^2\alpha_2^2\alpha_3^2\right)\\ & +K_3\left(\alpha_1^4\alpha_2^4+\alpha_1^4\alpha_3^4+\alpha_2^4\alpha_3^4\right) \quad .\end{aligned} \tag{3.77}$$

The indices of the anisotropy constants K_i from equation (3.76) are relabelled in

order to start with the lowest numbers. Again, anisotropy constants depend on the temperature.

The phenomenological constants K_i of rare earth metals can be derived from Mößbauer spectroscopy studies in a cumbersome process by analysis of spin-orientation diagrams (SODs) (*Atzmony and Dariel*, 1976). Alternatively, the K_i of rare earth metals can be derived from first principles by the Callen and Callen model of magnetic anisotropy (*Callen and Callen*, 1965, 1966) with a first-order expansion of the central field Hamiltonian, or by the extended Callen and Callen model (*Martin et al.*, 2006a) up to second order. The resulting K_i are in accordance with the values given by *Atzmony and Dariel* (1976).

3.3.4 Multipolar decomposition

Atzmony and Dariel (1976) have specified the phenomenological parameters K_1, K_2, K_3 as a function of the temperature T for the most important rare earth materials. Very surprisingly, some higher order terms do not decay with rising T; at times K_3 exceeds K_2, and even changes sign. The explanation for this behaviour was given by *Martin et al.* (2006a) who calculated anisotropy coefficients $\tilde{K_j}$ ($j = 2, 4, 6, ...$) with regard to the multipolar basis functions, the spherical harmonics Y_m^n. These $\tilde{K_j}$ coefficients are the mathematically correct higher order decomposition (and not the K_i). They decrease monotonically with T without changing sign, and higher order terms decrease faster than lower order terms. The phenomenological K_i parameters are a superposition of the multipolar coefficients $\tilde{K_j}$, where higher order terms up to $\tilde{K_8}$ cannot be neglected (equation (24) in *Martin et al.* (2006a)):

$$\begin{aligned} K_1 &= -\frac{15}{2\sqrt{\pi}}\tilde{K}_4 - \frac{21}{4}\sqrt{\frac{13}{\pi}}\tilde{K}_6 - 9\sqrt{\frac{17}{\pi}}\tilde{K}_8 \\ K_2 &= +\frac{231}{4}\sqrt{\frac{13}{\pi}}\tilde{K}_6 + 39\sqrt{\frac{17}{\pi}}\tilde{K}_8 \\ K_3 &= +\frac{65}{2}\sqrt{\frac{17}{\pi}}\tilde{K}_8 \quad . \end{aligned} \tag{3.78}$$

In appendix A.2, temperature dependent values of $\tilde{K_j}$ are listed for Er and Dy, so that the K_i values can be calculated using equation (3.78).

3.3.5 Cubic anisotropy in a (110) MBE grown film

In the previous section 3.3.3, we assumed that the x, y, z axes of the coordinate system coincide with the base directions of the crystal cell (labelled [100], [010], [001]). Equation (3.77) is only valid in this reference system. However, when a crystal film is grown by molecular beam epitaxy, the film coordinate directions are not necessarily identical to the crystal directions. For the multi-layered $REFe_2$ films (RE = rare earth element) investigated in chapters 6, 7, and 8, the growth direction of

the film (z axis) coincides with the crystallographic [110] direction. Any crystallographic direction $[abc]$ can be made up by a superposition of $a\,[100]+b\,[010]+c\,[001]$, and a barred number $\bar{d}$ corresponds to a negative sign of the coefficient d. In the following, we derive an equation of the cubic anisotropy energy that is applicable to the [110] grown films.

By crystallographic convention, the [110] growth direction is defined in a way that links the two coordinate systems as

- x axis $\equiv [00\bar{1}]$
- y axis $\equiv [\bar{1}10]$
- z axis $\equiv [110]$.

We now need to know the coordinate transformation that maps the two systems. The base vectors of the crystal cell system can be transformed onto the the base vectors of the film system by two Euler rotations: first, a rotation of 45° about the z axis ($\rightarrow$ x'y'z'), and second, a rotation of 90° about the new y' axis ($\rightarrow$ x'' y'' z'').

The Euler rotations are represented by the following matrix operations:

$$\begin{pmatrix} x' \\ y' \\ z' \end{pmatrix} = \begin{pmatrix} \frac{1}{\sqrt{2}} & \frac{1}{\sqrt{2}} & 0 \\ -\frac{1}{\sqrt{2}} & \frac{1}{\sqrt{2}} & 0 \\ 0 & 0 & 1 \end{pmatrix} \begin{pmatrix} x \\ y \\ z \end{pmatrix} \tag{3.79}$$

and

$$\begin{pmatrix} x'' \\ y'' \\ z'' \end{pmatrix} = \begin{pmatrix} 0 & 0 & -1 \\ 0 & 1 & 0 \\ 1 & 0 & 0 \end{pmatrix} \begin{pmatrix} x' \\ y' \\ z' \end{pmatrix} \quad . \tag{3.80}$$

These transformations determine how the coordinates of a fix point, given the in system (xyz/x'y'z'), appear in the rotated system (x'y'z'/x''y''z'').

The corresponding back transformation is obtained by matrix multiplication and inversion:

$$\begin{pmatrix} x \\ y \\ z \end{pmatrix} = \begin{pmatrix} 0 & -\frac{1}{\sqrt{2}} & \frac{1}{\sqrt{2}} \\ 0 & \frac{1}{\sqrt{2}} & \frac{1}{\sqrt{2}} \\ -1 & 0 & 0 \end{pmatrix} \begin{pmatrix} x'' \\ y'' \\ z'' \end{pmatrix} \quad . \tag{3.81}$$

The equations derived in section 3.3.3 refer to (xyz) coinciding with the crystal system . Replacing the α_i by x, y, z in the cubic anisotropy (3.77), applying the inverse

transformation (3.81) and dropping the ″ for simplification results in

$$\begin{aligned}\varepsilon_{\mathrm{a}} = \quad & K_1\left(\frac{1}{4}\left(y^2-z^2\right)^2+x^2\left(y^2+z^2\right)\right)+K_2\left(\frac{1}{4}x^2\left(y^2-z^2\right)^2\right)\\ + \quad & K_3\left(\frac{1}{16}\left(y^2-z^2\right)^4+\frac{1}{2}x^4\left(y^4+z^4+6y^2z^2\right)\right) \quad . \end{aligned} \tag{3.82}$$

It is reminded that the direction (x,y,z) must be normalised: point (x,y,z) is located on the unit sphere around the origin.

3.3.6 Strain energy

Magnetic measurements (*Mougin et al.*, 2000) have shown that $REFe_2$ (RE = rare earth element) superlattice films grown by molecular beam epitaxy are strained compared to bulk compounds. The strain is caused by differential thermal contraction between the film and the substrate. It can be treated as an additional energy term and affects the directions of the easy axes. For low temperatures, the cubic anisotropy is dominant, and the easy axes are identical for bulk compounds and films. Over a specific temperature threshold, the easy axes of the films start to rotate, and can be offset by 90° for room temperature.

Following *Bowden et al.* (2006), the magnetoelastic Hamiltonian generally can be written as

$$\begin{aligned}\mathcal{H}_{\mathrm{me}} = \quad & b_2\left(\epsilon_{\mathrm{xx}}\alpha_{\mathrm{x}}^2+\epsilon_{\mathrm{yy}}\alpha_{\mathrm{y}}^2+\epsilon_{\mathrm{zz}}\alpha_{\mathrm{z}}^2\right)+\\ & b_2\left(\epsilon_{\mathrm{xy}}\alpha_{\mathrm{x}}\alpha_{\mathrm{y}}+\epsilon_{\mathrm{xz}}\alpha_{\mathrm{x}}\alpha_{\mathrm{z}}+\epsilon_{\mathrm{yz}}\alpha_{\mathrm{y}}\alpha_{\mathrm{z}}\right) \quad , \end{aligned} \tag{3.83}$$

where ϵ_{ij} with $i,j \in \{\mathrm{x},\mathrm{y},\mathrm{z}\}$ is the strain tensor and b_2 is the magnetoelastic coefficient. For the investigated [110] grown films, only ϵ_{xy} is relevant. The first-order change to the free energy per formula unit due to the magnetoelastic term $E_{\mathrm{me}}^{\mathrm{first}}$ is the expectation value of the Hamiltonian, and we get an energy density

$$\begin{aligned}\varepsilon_{\mathrm{me}}^{\mathrm{first}} &= b_2\,\epsilon_{\mathrm{xy}}\alpha_{\mathrm{x}}\alpha_{\mathrm{y}}\\ &= \tilde{K}_2'\sqrt{\frac{15}{2\pi}}\alpha_{\mathrm{x}}\alpha_{\mathrm{y}} \quad , \end{aligned} \tag{3.84}$$

with the rank 2 multipole coefficient $\tilde{K}_2' = \sqrt{\frac{2\pi}{15}}b_2\,\epsilon_{\mathrm{xy}}$ in units of J/m.

Out of the second-order contributions $\varepsilon_{\mathrm{me}}^{\mathrm{second}}$, only one term has considerable weight, and we ignore the other terms:

$$\varepsilon_{\mathrm{me}}^{\mathrm{second}} = \tilde{K}_{242}''\sqrt{\frac{15}{2\pi}}\alpha_{\mathrm{x}}\alpha_{\mathrm{y}} \quad , \tag{3.85}$$

with the same functional form as $\varepsilon_{\mathrm{me}}^{\mathrm{first}}$. The comprehensive calculation of $\tilde{K}_2'$ and $\tilde{K}_{242}''$ is detailed in *Bowden et al.* (2006), and values for Er and Dy are given in the

appendix A.3 for the temperature range 10 K to 400 K. This leaves us with a second-order total energy approximation

$$\varepsilon_{\mathrm{me}} = \sqrt{\frac{15}{2\pi}}(\tilde{K}_2' + \tilde{K}_{242}'')\,\alpha_{\mathrm{x}}\alpha_{\mathrm{y}} \quad . \tag{3.86}$$

It is emphasised that the frame of reference so far are the crystal lattice directions. As for the cubic anisotropy in the previous chapter, the magnetoelastic energy has to be transformed to the film plane system. Thus, we apply transformation (3.81) (skipping the ″) and get

$$\varepsilon_{\mathrm{me}} = \frac{1}{2}\sqrt{\frac{15}{2\pi}}(\tilde{K}_2' + \tilde{K}_{242}'')(z^2 - y^2) \quad , \tag{3.87}$$

or, in polar coordinates,

$$\varepsilon_{\mathrm{me}} = \frac{1}{2}\sqrt{\frac{15}{2\pi}}(\tilde{K}_2' + \tilde{K}_{242}'')(\cos^2\theta - \sin^2\theta\sin^2\phi) \quad . \tag{3.88}$$

Occasionally, the strain terms $d_{\mathrm{xy}} = 2\sqrt{\frac{15}{2\pi}}\tilde{K}_2'$ and $d_{242} = 2\sqrt{\frac{15}{2\pi}}\tilde{K}_{242}''$ are used instead of $\tilde{K}_2'$ and $\tilde{K}_{242}''$. A comparison of equation (3.87) with the second-order uniaxial anisotropy energy (3.61) shows that the strain energy can be considered a superposition of uniaxial anisotropies in y and z. The corresponding anisotropy constants k_{y} and k_{z} have the same modulus but opposite signs,

$$k_{\mathrm{y}} = -k_{\mathrm{z}} = \frac{1}{4}(d_{\mathrm{xy}} + d_{242}) \quad . \tag{3.89}$$

This relation is helpful for the OOMMF simulation package, as OOMMF provides an option to input uniaxial anisotropies, but not strain terms directly.

3.4 Zeeman and dipolar energy

There are two approaches to consider magnetic phenomena inside matter: a microscopic one is to resolve the matter into its constituents, a very large number of individual particles, and to see how each of them individually reacts on an externally applied field and on the field produced by the other particles. The particles — tiny magnets themselves — align with the external field, and produce an additional field that is opposed to the external field. This is the so-called demagnetising or dipolar field. The second approach is a macroscopic view, based on the observation of a reduced effective field inside matter. The reduction of the field is accounted to the magnetisation inside the magnetic body as a reaction to the applied field, without considering the atomic origin of the field reduction. Usually, the first option is not feasible, as far too many interacting particles would have to be taken

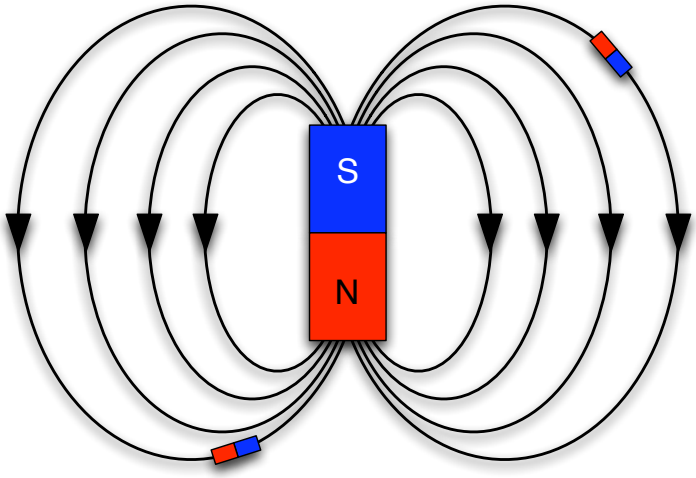

Figure 3.5: Schematic of a dipolar magnetic field, with the field lines running from the north pole to the south pole

regard to. Still, it is useful to introduce the demagnetising field for the macroscopic approach, knowing about its atomic origin.

3.4.1 Microscopic approach: dipolar energy of particles

For the microscopic approach, we assume that the magnetic body is made up by a lattice of dipolar particles, each dipole representing the magnetic moment $\boldsymbol{m}$ of one molecule (figure 3.5). Each individual dipole generates its magnetic field, thus acting on all the other dipoles, and vice versa. The field of a dipole j at position $\boldsymbol{r}$ is known as (*Jackson*, 1999, p. 186)

$$\boldsymbol{B}_j(\boldsymbol{r}) = \frac{\mu_0}{4\pi}\left[\frac{3\hat{\boldsymbol{n}}_j(\hat{\boldsymbol{n}}_j \cdot \boldsymbol{m}_j) - \boldsymbol{m}_j}{r_j^3}\right] \quad , \tag{3.90}$$

where $\hat{\boldsymbol{n}}_j$ is the unit vector pointing from the dipole j to $\boldsymbol{r}$, and r_j is the distance. Another dipole i at position $\boldsymbol{r}_i$ will then feel the field contributions of all other dipoles:

$$\boldsymbol{B}(\boldsymbol{r}_i) = \frac{\mu_0}{4\pi}\sum_{j\neq i}\left[\frac{3\hat{\boldsymbol{n}}_{ji}(\hat{\boldsymbol{n}}_{ji} \cdot \boldsymbol{m}_j) - \boldsymbol{m}_j}{r_{ij}^3}\right] \quad , \tag{3.91}$$

where $\hat{\boldsymbol{n}}_{ji}$ is the unit vector pointing from j to i, and r_{ij} is the distance between i and j. The energy of a dipole i with the magnetic moment $\boldsymbol{m}_i$ in an external magnetic field $\boldsymbol{B}(\boldsymbol{r}_i)$ is

$$E_{\text{dipole},i} = -\boldsymbol{m}_i \cdot \boldsymbol{B}(\boldsymbol{r}_i) \quad . \tag{3.92}$$

For the complete ensemble, the total energy is the sum of the energy of the individual dipoles,

$$E_{\text{dipoles}} = -\frac{1}{2}\sum_i \boldsymbol{m}_i \cdot \boldsymbol{B}(\boldsymbol{r}_i) = -\frac{1}{2}\frac{\mu_0}{4\pi}\sum_i \boldsymbol{m}_i \cdot \sum_{j\neq i}\left[\frac{3\hat{\boldsymbol{n}}_{ji}(\hat{\boldsymbol{n}}_{ji}\cdot\boldsymbol{m}_j) - \boldsymbol{m}_j}{r_{ij}^3}\right] . \quad (3.93)$$

The factor $\frac{1}{2}$ is required to avoid double counting the interactions, as the double summation runs over each pair of (i, j) twice.

3.4.2 Macroscopic approach: energy of an external field and a demagnetising field in a magnetic body

The standard equations for the magnetic field $\boldsymbol{H}$ and the flux density $\boldsymbol{B}$ in a magnetic body are (*Blundell*, 2001, p. 216)

$$\boldsymbol{H}(\boldsymbol{r}) = \boldsymbol{H}_{\text{z}}(\boldsymbol{r}) + \boldsymbol{H}_{\text{d}}(\boldsymbol{r}) \quad (3.94)$$

$$\boldsymbol{B}(\boldsymbol{r}) = \boldsymbol{B}_{\text{z}}(\boldsymbol{r}) + \boldsymbol{B}_{\text{d}}(\boldsymbol{r}) \quad , \quad (3.95)$$

where both $\boldsymbol{H}$ and $\boldsymbol{B}$ are made up by externally applied contributions (subscript z for Zeeman) and demagnetising contributions (subscript d). It is recalled that the demagnetising flux density inside the body is related to the field by

$$\boldsymbol{B}_{\text{d}}(\boldsymbol{r}) = \mu_0(\boldsymbol{H}_{\text{d}}(\boldsymbol{r}) + \boldsymbol{M}(\boldsymbol{r})) \quad , \quad (3.96)$$

where $\boldsymbol{M}(\boldsymbol{r})$ is the magnetisation. For the applied field,

$$\boldsymbol{B}_{\text{z}}(\boldsymbol{r}) = \mu_0\boldsymbol{H}_{\text{z}}(\boldsymbol{r}) \quad . \quad (3.97)$$

The energy of the ferromagnetic body itself is the energy where the body is placed in overall space minus the energy of overall space without any matter. This corresponds to the energy difference between the total field $\int \frac{1}{2}\mu_0\boldsymbol{H}^2\text{d}V$ and the applied field $\int \frac{1}{2}\mu_0\boldsymbol{H}_{\text{z}}^2\text{d}V$ in overall space (*Jackson*, 1999, p. 214):

$$E = \frac{\mu_0}{2}\int_{\text{allspace}} \left(\boldsymbol{H}^2 - \boldsymbol{H}_{\text{z}}^2\right)\text{d}V \quad . \quad (3.98)$$

From (3.94) it follows that

$$\boldsymbol{H}^2 = \boldsymbol{H}_{\text{z}}^2 + 2\boldsymbol{H}_{\text{z}}\cdot\boldsymbol{H}_{\text{d}} + \boldsymbol{H}_{\text{d}}^2 \quad , \quad (3.99)$$

so that

$$\begin{aligned} E &= \frac{\mu_0}{2}\int_{\text{allspace}} \left(2\boldsymbol{H}_\text{d}\cdot\boldsymbol{H}_\text{z}+\boldsymbol{H}_\text{d}^2\right)\text{d}V \\ &= \frac{\mu_0}{2}\int_{\text{allspace}} \boldsymbol{H}_\text{d}\cdot\left(2\boldsymbol{H}_\text{z}+\boldsymbol{H}_\text{d}\right)\text{d}V \quad . \end{aligned} \tag{3.100}$$

By use of (3.96) we get

$$\begin{aligned} E &= \frac{\mu_0}{2}\int_{\text{allspace}} \left(\frac{\boldsymbol{B}_\text{d}}{\mu_0}-\boldsymbol{M}\right)\cdot\left(2\boldsymbol{H}_\text{z}+\boldsymbol{H}_\text{d}\right)\text{d}V \\ &= -\frac{\mu_0}{2}\int_{\text{allspace}} \boldsymbol{M}\cdot\boldsymbol{H}_\text{d}\text{d}V-\mu_0\int_{\text{allspace}} \boldsymbol{M}\cdot\boldsymbol{H}_\text{z}\text{d}V \\ &\quad +\int_{\text{allspace}} \boldsymbol{B}_\text{d}\cdot\boldsymbol{H}_\text{z}\text{d}V+\frac{1}{2}\int_{\text{allspace}} \boldsymbol{B}_\text{d}\cdot\boldsymbol{H}_\text{d}\text{d}V \quad . \end{aligned} \tag{3.101}$$

The last two terms in (3.101) vanish. This is because of the vanishing rotation $\boldsymbol{\nabla}\times\boldsymbol{H}_\text{d}=0$ and $\boldsymbol{\nabla}\times\boldsymbol{H}_\text{z}=0$, and because of the vanishing divergence $\boldsymbol{\nabla}\cdot\boldsymbol{H}_\text{d}=0$ and $\boldsymbol{\nabla}\cdot\boldsymbol{H}_\text{z}=0$. The complete proof is shown on (*Blundell*, 2001, p. 216) or (*Aharoni*, 2000, p. 146). Finally, the energy equation becomes

$$E = -\frac{\mu_0}{2}\int_{\text{volume}} \boldsymbol{M}\cdot\boldsymbol{H}_\text{d}\text{d}V-\mu_0\int_{\text{volume}} \boldsymbol{M}\cdot\boldsymbol{H}_\text{z}\text{d}V \tag{3.102}$$

and contains a demagnetising term and a Zeeman term. The integral is restricted to the volume of the ferromagnetic body now, because the magnetisation vanishes outside the body. Still, the equation implicitly includes the energy of overall space. The factor $\frac{1}{2}$ for the demagnetising term reflects the fact that the particles had to produce their demagnetising configuration themselves, whereas the Zeeman term is due to an outer applied field that is kept permanently and does not feel any repercussion from the system inside. An alternative strategy to explain the origin of the factor $\frac{1}{2}$ is to refer to the microscopic equation (3.93), where the factor $\frac{1}{2}$ compensates for double counting, and to substitute the summation by an integral. However, the macroscopic concept provides a clear insight into the interaction of the applied field and the resulting demagnetising field.

3.4.3 Calculation of the demagnetising field

The difficulty with equation (3.102) is that we do not know the demagnetising field per se. It is possible to analytically calculate this field for a number of simple cases (like a homogeneously magnetised sphere or cube), but generally a Poisson/Laplace equation derived from Maxwell equations with appropriate boundary conditions has to be solved.

We assume that there are no free currents. Then, one of the Maxwell equations

states that the curl of a magnetic field $\boldsymbol{H}$ vanishes:

$$\boldsymbol{\nabla} \times \boldsymbol{H} = \boldsymbol{0} \quad . \tag{3.103}$$

It is emphasised that the absence of free currents refers to macroscopic currents, as equation (3.103) is valid for the macroscopic field $\boldsymbol{H}$ only, but absolutely invalid for $\boldsymbol{B}$. Another Maxwell equation embodies the absence of magnetic monopoles:

$$\boldsymbol{\nabla} \cdot \boldsymbol{B} = \boldsymbol{0} \quad . \tag{3.104}$$

The next bit needed in this context is the interrelation of $\boldsymbol{H}$ and $\boldsymbol{B}$, which was already given in equation (3.96). The fact that $\boldsymbol{H}$ is curl-free (3.103) allows us to define a potential Φ in a way that

$$\boldsymbol{H} = -\boldsymbol{\nabla}\Phi \tag{3.105}$$

holds. Putting the pieces together, we can write the Laplace operator of Φ as a Poisson equation,

$$\begin{aligned} \triangle\Phi &= \boldsymbol{\nabla} \cdot \boldsymbol{\nabla}\Phi = \boldsymbol{\nabla} \cdot (-\boldsymbol{H}) \\ &= \boldsymbol{\nabla} \cdot \left[\frac{1}{\mu_0} (\boldsymbol{M} - \boldsymbol{B}) \right] = \frac{1}{\mu_0} \boldsymbol{\nabla} \cdot \boldsymbol{M} \quad . \end{aligned} \tag{3.106}$$

Outside the magnetic body, $\boldsymbol{M}$ is zero, and we get the Laplace equation

$$\triangle\Phi = 0 \quad . \tag{3.107}$$

At the surface of the magnetic body, appropriate boundary conditions have to be applied to (3.106). The same applies to (3.107) at an infinite distance. This actually is the problem with the combined Poisson/Laplace equation: the function Φ ranges over the complete space and not only the magnetic body, due to the far-ranging character of the dipolar interaction. It is an 'open boundary problem'.

Several approaches to solve the Poisson/Laplace equation (3.106)/ (3.107) exist: One option is to encapsulate the magnetic body in a sufficiently large area, with area boundaries far away from the magnetic body, so that the potential Φ is constant to a good approximation outside this area (*Ridley*, 2000, *Spargo*, 2002). Then solving the Poisson/Laplace equation, *e.g.* by using finite elements, can be restricted to this area with an acceptable error.

Another approach is the hybrid finite element/boundary element method, which requires no finite elements outside the magnetic body (*Fredkin and Koehler*, 1990, *Scholz*, 2003). The idea of this method is to split the potential Φ in two parts Φ_1 and Φ_2, so that Φ_1 vanishes outside the magnetic body, and Φ_2 solves the homogeneous Laplace equation for the complete space. The resulting Poisson equation for Φ_1 can

then be solved by means of finite elements. By applying the proper boundary conditions, we can express Φ_2 by Φ_1 and the Green functions. The total potential Φ is finally retrieved by adding Φ_1 and Φ_2.

A third option to tackle the problem is applied by OOMMF. Its regular finite difference lattice with equally shaped cuboidal cells allows OOMMF to calculate a homogeneous demagnetising field inside each of the cells by use of demagnetising tensors (*Aharoni*, 1998, *Newell et al.*, 1993). The global demagnetisation is then determined by convolution of the individual cells via the Fast Fourier Transformation.

3.4.4 Thin film approximation for the demagnetising energy

For many thin film applications, it is a feasible approach to assume an infinite flat slab for each film layer. In this case, we can express the demagnetising energy in terms of a uniaxial anisotropy that is numerically easy to handle.

The magnetisation $\boldsymbol{M}$ in the slab is split into one component perpendicular to the film plane ($\boldsymbol{M}_\perp$), and another component in the film plane ($\boldsymbol{M}_\parallel$):

$$\boldsymbol{M} = \boldsymbol{M}_\perp + \boldsymbol{M}_\parallel \quad . \tag{3.108}$$

With θ denoting the angle that encloses the normalised magnetisation direction $\hat{\boldsymbol{M}}$ and the unit direction $\hat{\boldsymbol{e}}_\perp$ perpendicular to the slab, the perpendicular component $\boldsymbol{M}_\perp$ can be written as ($M = |\boldsymbol{M}|$)

$$\boldsymbol{M}_\perp = M\, \cos\theta\, \hat{\boldsymbol{e}}_\perp \quad . \tag{3.109}$$

While $\boldsymbol{M}_\perp$ excites magnetic charges on the top and bottom of the slab and subsequently a demagnetising field $\boldsymbol{H}_{\mathrm{d},\perp} = -\boldsymbol{M}_\perp$, $\boldsymbol{M}_\parallel$ generates infinitely small magnetic charges on the sides of the slab that are negligible, with vanishing demagnetising field $\boldsymbol{H}_{\mathrm{d},\parallel}$. In conclusion, we get the total demagnetising field $\boldsymbol{H}_\mathrm{d}$:

$$\boldsymbol{H}_\mathrm{d} = \boldsymbol{H}_{\mathrm{d},\perp} = -\boldsymbol{M}_\perp = -M\, \cos\theta\, \hat{\boldsymbol{e}}_\perp \quad . \tag{3.110}$$

Applying (3.110) on (3.102), the energy of a thin film layer becomes

$$\begin{aligned}
E &= -\frac{\mu_0}{2} \int_\mathrm{layer} \boldsymbol{M} \cdot \boldsymbol{H}_\mathrm{d}\, \mathrm{d}V \\
&= -\frac{\mu_0}{2} \int_\mathrm{layer} (\boldsymbol{M}_\perp + \boldsymbol{M}_\parallel) \cdot (-M\, \cos\theta\, \hat{\boldsymbol{e}}_\perp)\, \mathrm{d}V \\
&= \frac{\mu_0}{2} \int_\mathrm{layer} \boldsymbol{M}_\perp \cdot (M\, \cos\theta\, \hat{\boldsymbol{e}}_\perp)\, \mathrm{d}V \\
&= \frac{\mu_0}{2} \int_\mathrm{layer} M^2\, \cos^2(\theta)\, \mathrm{d}V \\
&= \frac{\mu_0}{2} \int_\mathrm{layer} M^2\, |\hat{\boldsymbol{M}} \cdot \hat{\boldsymbol{e}}_\perp|^2\, \mathrm{d}V \quad .
\end{aligned} \tag{3.111}$$

Recalling equation (3.61), we realise that this is the energy of a uniaxial anisotropy with $K_1 = -\frac{\mu_0}{2}M^2$ and the hard axis in $\hat{\boldsymbol{e}}_\perp$. This result will prove valuable for various simulations of thin film samples presented in upcoming chapters.

Chapter 4

Discrete molecular dynamic magnetic simulation code

4.1 Introduction

The micromagnetic simulation code OOMMF has become a standard in magnetic research, successfully used by the community in a multitude of projects. Our own research is based on OOMMF simulations as well. In spite of its strong uptake in the community, it is a necessity to assess the quality and reliability of OOMMF ourselves. Therefore we have developed an alternative code on the basis of discrete dipolar magnets with discrete magnetisation vectors: *discreteMag*. DiscreteMag allows real-time monitoring of the magnetisation dynamics. The magnetisation vectors are displayed and updated at runtime, making the program suitable for educational purposes.

In the next section 4.2, we briefly describe OOMMF and the other programs used to run simulations and evaluate the results. In section 4.3, we explain the implementation of the discreteMag code and the energy equations used. DiscreteMag and OOMMF are then applied on a set of simple test scenarios (section 4.4), comprising of tests of the individual energies (4.4.1 to 4.4.4) and the Stoner-Wohlfarth model (4.4.5), and results are compared.

4.2 OOMMF and the software environment

The Object Oriented MicroMagnetic Framework (OOMMF) is an open source software package created by the National Institute for Standards and Technology (NIST). It uses finite difference methods to solve the relevant micromagnetic equations. Its advantages are stability and reliability, availability, support by NIST, and relative ease-of-use. Extensions are possible up to some degree. For these reasons, it is widely used by micromagnetic researchers.

Micromagnetic simulations are specified to the OOMMF solvers by a problem

definition file in the Micromagnetic Input Format (*MIF*): the geometry and resolution is defined, the relevant energies selected, the physical and material parameters as well as technical execution variables set. Position dependent quantities can be defined as functions by plug-in Tcl/Tk code.

The open source programming language Python (*Python community*, 2007, *van Rossum and Drake*, 2001) is an all-purpose tool extensively used in this project. It is object oriented and portable, with powerful support of various toolkits, libraries, and mathematical packages. Thus, it serves as a scripting language for generating MIF files and controlling their execution, calculating physical quantities as an input for the MIF files, as a tool to convert between different file formats of the simulation output, and to process data, *e.g.* by determining average magnetisations. Python offers an interactive interpreter mode for quick calculations and tests, but can also precompile and run program files.

For the visualisation of the simulation results, the tool of our choice is MayaVi (*Ramachandran*, 2001), based on the Visualisation ToolKit VTK (*Schroeder et al.*, 1996). These are open source tools as well. VTK is an integrated image processing toolkit which has 3D algorithms and makes use of hardware accelerated graphics adapters. MayaVi offers multiple rendering and filtering modalities, *e.g.* enabling the presentation of vector fields, scalar fields, or isosurfaces. The latter option is combined with a python program in order to plot 3D graphs for analytically known functions like the anisotropy energy (*e.g.* right side of figure 3.3 on page 32).

4.3 DiscreteMag implementation

A cubic lattice is assumed, with the particles being located at the lattice nodes. We choose a cuboidal simulation geometry. For the energy and field calculations, the following equations are applied:

- exchange energy: equation (3.26), where $\mathcal{J}$ is calculated from the exchange constant by equation (3.41)
- Zeeman energy: equation (3.92)
- anisotropy energy: equation (3.61)
- dipolar energy: equation (3.93).

The following parameters can be set in a configuration file:

- material parameters like saturation magnetisation, exchange constant, uniaxial anisotropy constant and direction
- geometry parameters
- lattice constant

- initial configuration of magnetisation vectors — random configuration possible
- energies to be considered
- applied field — field sweep from a start value to an end value in a number of steps in order to generate a magnetisation curve
- visualisation options
- numerical parameters (e.g. accuracy of the integrator).

For the temporal evolution, the Landau-Lifshitz equation (2.8) is used. The code is implemented in Python. Integration is performed in temporal slices, and for each slice, the resulting magnetisation configuration is displayed via the 3d graphics Python module *Visual* (*Chabay et al.*, 2005). The *VODE* package (*Hindmarsh and Petzold*, 1995) is used to perform the integration for each time slice. VODE is part of the Python package *scipy.integrate* for scientific computing (*SciPy community*, 2007), and as such ready to use. Its algorithms are implemented in C and provide sufficient performance. As a stopping criterion, the overall change of the magnetisation vectors between successive time slices is compared to a stopping value.

4.4 Results

Both programs, OOMMF and discreteMag, perform simulation runs on corresponding test scenarios, for each interaction separately, and on a Stoner-Wohlfarth setup. For every test scenario, the trajectory of the magnetisation vectors is depicted as obtained by discreteMag to outline the dynamics of the individual interactions. The consistency of the results is checked by plots of energy and spatially averaged magnetisation components as a function of evolution time.

The parameters used for the simulations are:

parameter	value
lattice constant	$1.0 \cdot 10^{-9}\mathrm{m}$
magnetisation M	$1.4 \cdot 10^{6}\mathrm{A/m}$
anisotropy constant K	$5.2 \cdot 10^{5}\mathrm{J/m^3}$
exchange constant A	$1.5 \cdot 10^{-11}\mathrm{J/m}$

The material parameters stated correspond to the values of cobalt. The time slicing is chosen in a way that it sufficiently resolves the dynamics of the precession and damping movement of the magnetisation vectors.

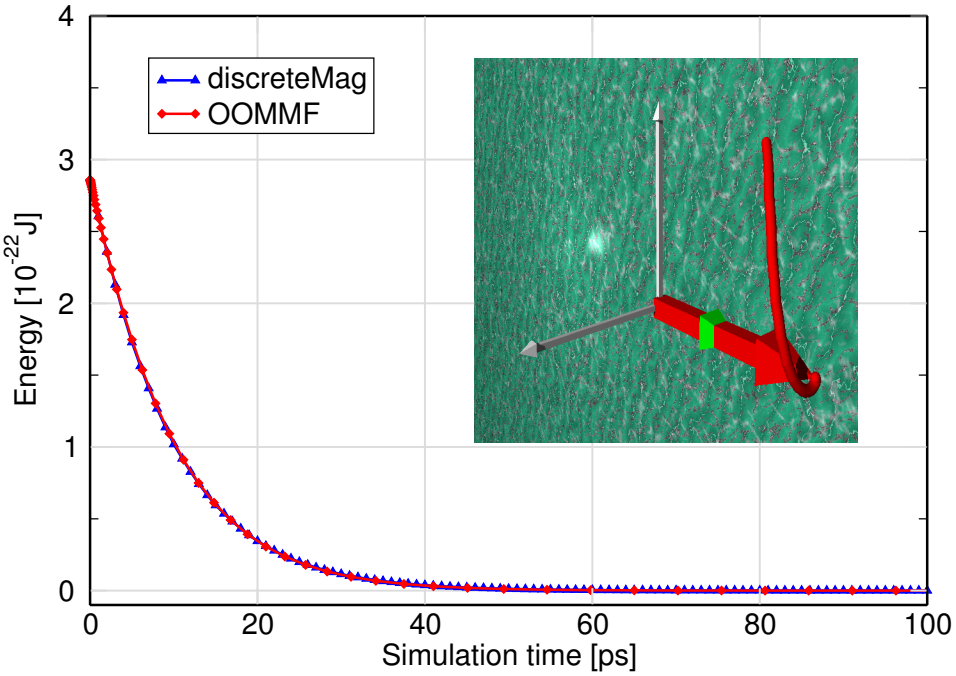

Figure 4.1: Comparison of the energy dynamics as a result of OOMMF and discreteMag for sole Zeeman interaction. The inset depicts the trajectory (red curved tube) of the magnetisation vector (red arrow) for a damping factor of $\alpha = 1.6$. The applied field direction is represented by the green arrow (only tip visible), the coordinate axes by the white arrows (x axis covered). The magnetisation vector finally settles in the direction of the applied field.

4.4.1 Dynamics of Zeeman

When applying an external field in x direction on a single cell, the discreteMag simulation results show the expected behaviour of a damped precessional movement for the magnetisation vector (see inset of figure 4.1). At the end of the relaxation, the magnetisation is aligned with the applied field. A comparison of the discreteMag dynamics of the energy and of the magnetisation components with corresponding OOMMF results is given in figures 4.1 and 4.2 on the next page. The energy values and the relaxation time fit well: both energy curves match to a degree that they practically overlay each other. Sufficient agreement on the dynamics of the magnetisation components is achieved, too.

The latter simulations were performed for a Landau-Lifshitz damping parameter $\alpha = 1.6$. With a smaller $\alpha = 0.1$ corresponding to reduced damping, the precession persists for a longer time with additional orbits (figure 4.3 on the following page).

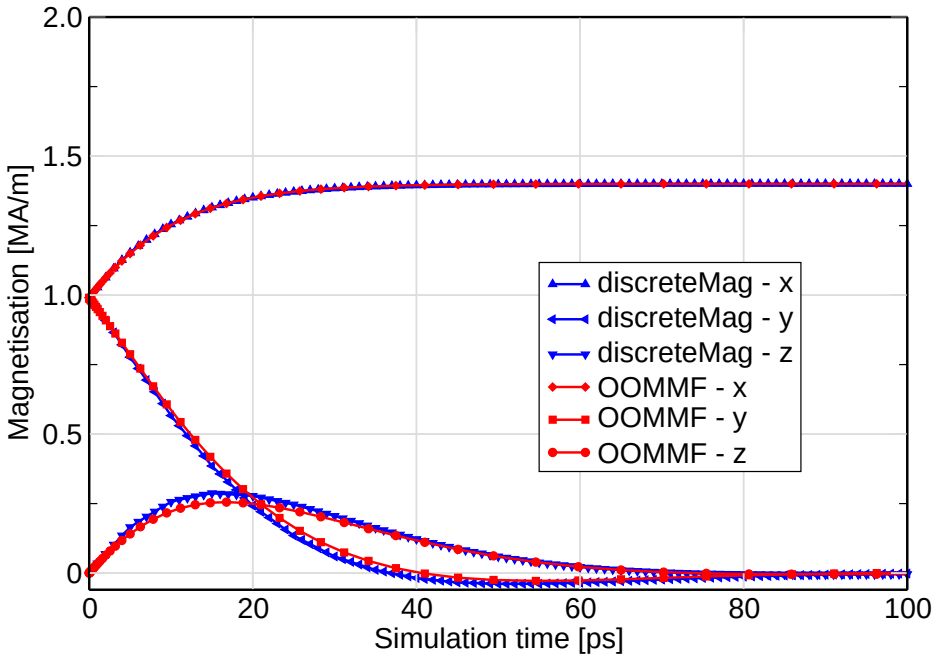

Figure 4.2: Comparison of the dynamics of the $\mathrm{x}, \mathrm{y}, \mathrm{z}$ magnetisation components as a result of OOMMF and discreteMag for sole Zeeman interaction.

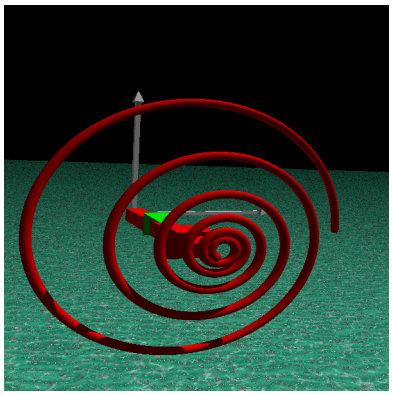

Figure 4.3: Magnetisation trajectory with reduced damping parameter $\alpha = 0.1$ for sole Zeeman interaction. The red curved line is the trace of the tip of the magnetisation vector, spiralling towards the applied field direction (green arrow, only tip visible).

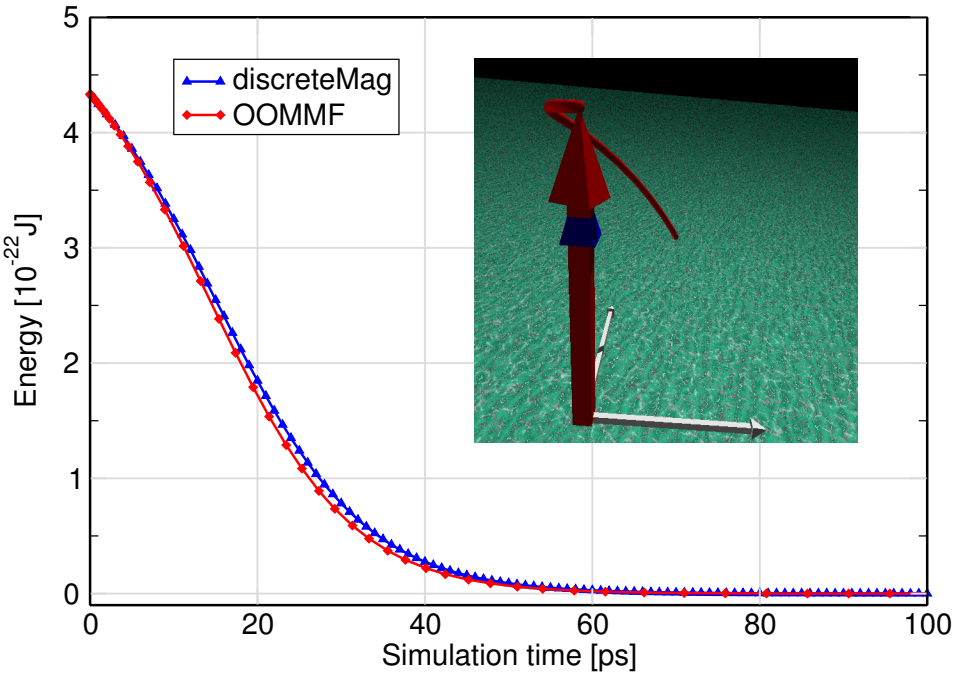

Figure 4.4: Comparison of the energy dynamics as a result of OOMMF and discreteMag for sole uniaxial anisotropy interaction. The inset depicts the trajectory (red curved tube) of the magnetisation vector (red arrow) for $\alpha = 1.6$. The easy anisotropy axis is represented by the blue arrow (only tip visible), the coordinate axes by the white arrows (x axis covered). The magnetisation vector finally settles in the direction of the easy axis.

4.4.2 Dynamics of anisotropy

When applying a uniaxial anisotropy with an easy axis in x direction, the discreteMag simulation results show the expected behaviour for the magnetisation vector: it gyrates towards the easy axis (see inset of figure 4.4). At the end of the relaxation, the magnetisation is aligned with the easy anisotropy axis. A comparison of the discreteMag dynamics of the energy and of the magnetisation components with corresponding OOMMF results is given in figures 4.4 and 4.5. Again, energy dynamics and magnetisation dynamics are in satisfactory accordance.

4.4.3 Dynamics of exchange

In order to validate discreteMag and OOMMF with regard to exchange interaction, both simulations start from the same random spin configuration of an ensemble of $3 \times 3 \times 3 = 27$ particles or cells. Naturally, the exchange interaction aligns the spins, in accordance to the discreteMag simulation results (see inset of figure 4.6 on page 51). The final common direction of the spins is not obvious from the start configuration. A comparison of the discreteMag dynamics of the energy and of the magnetisation components with corresponding OOMMF results is given in figures

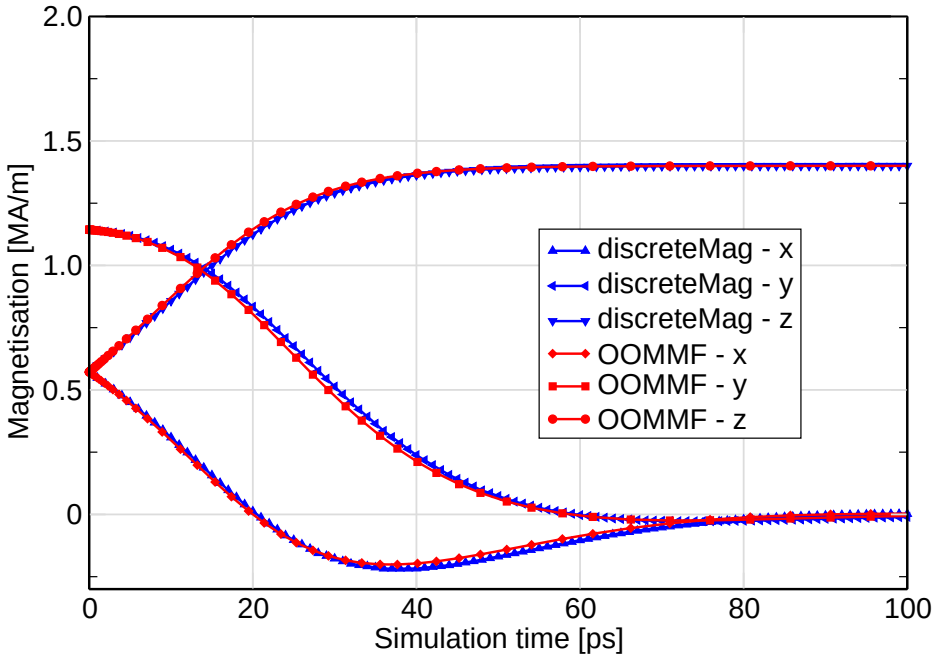

Figure 4.5: Comparison of the dynamics of the $\mathrm{x}, \mathrm{y}, \mathrm{z}$ magnetisation components as a result of OOMMF and discreteMag for sole uniaxial anisotropy interaction.

4.6 and 4.7 on the next page. Again, energy dynamics and magnetisation dynamics are in satisfactory agreement.

4.4.4 Dynamics of demagnetisation

For the dipolar interaction, 2×2 particles were simulated, starting from a given spin configuration. Here, the spins are expected to form a vortex, minimising distances between different magnetic poles and maximising distances between identical magnetic poles. The inset of figure 4.8 on page 52 as a result of discreteMag confirms the expectation. The energy dynamics and magnetisation dynamics for OOMMF and discreteMag, depicted in figures 4.8 and 4.9 on page 52, match well. All three magnetisation components in figure 4.9 converge to zero — the correct value for a vortex.

4.4.5 Stoner-Wohlfarth model

Another approach for assessing the quality of a simulation code is the application to a scenario where an analytic solution is known. A famous representative of this class of systems in the field of magnetism is the Stoner-Wohlfarth model. It describes a ferromagnetic particle of a size that is large enough to ignore the

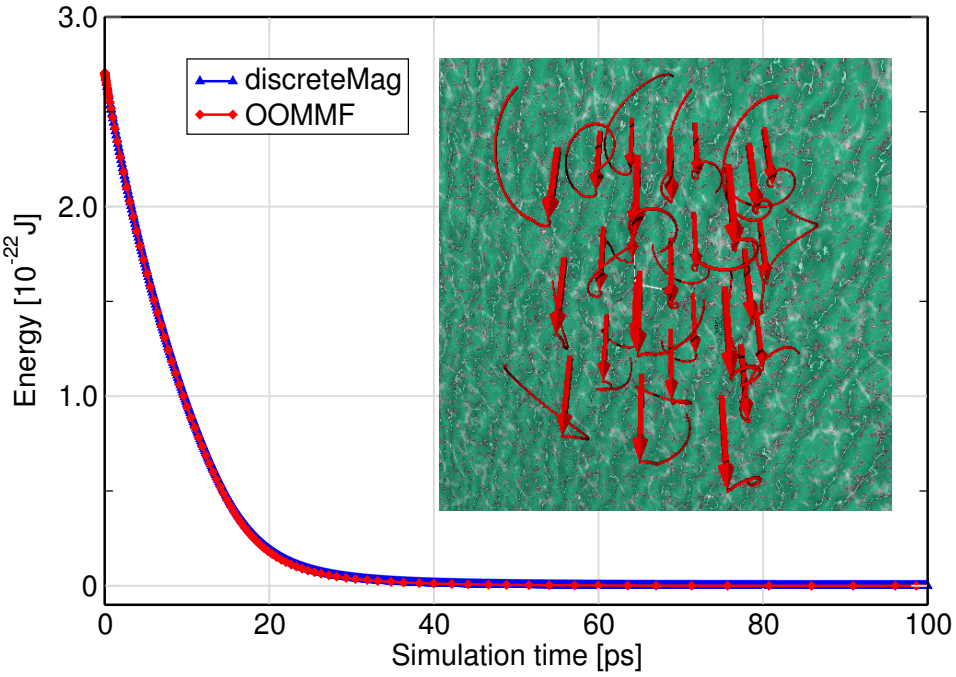

Figure 4.6: Comparison of the energy dynamics as a result of OOMMF and discreteMag for sole exchange interaction. The inset depicts the trajectories (red curved tubes) of $3 \times 3 \times 3 = 27$ spins (red arrows) for $\alpha = 1.6$. The coordinate axes are represented by the white arrows far behind the spins. In the final equilibrium state, all spins are aligned.

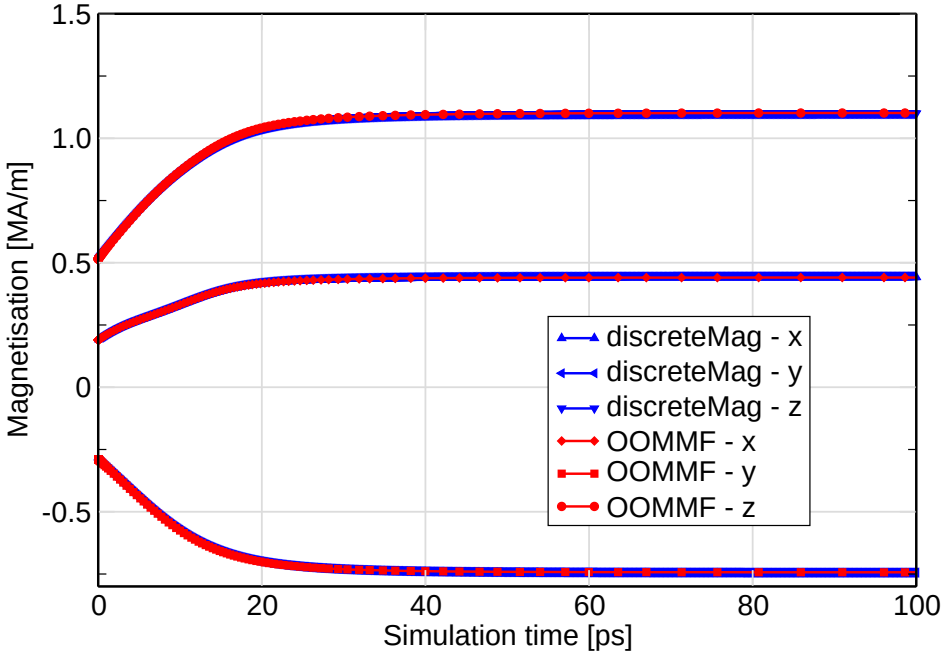

Figure 4.7: Comparison of the dynamics of the $\mathrm{x}, \mathrm{y}, \mathrm{z}$ magnetisation components as a result of OOMMF and discreteMag for sole exchange interaction.

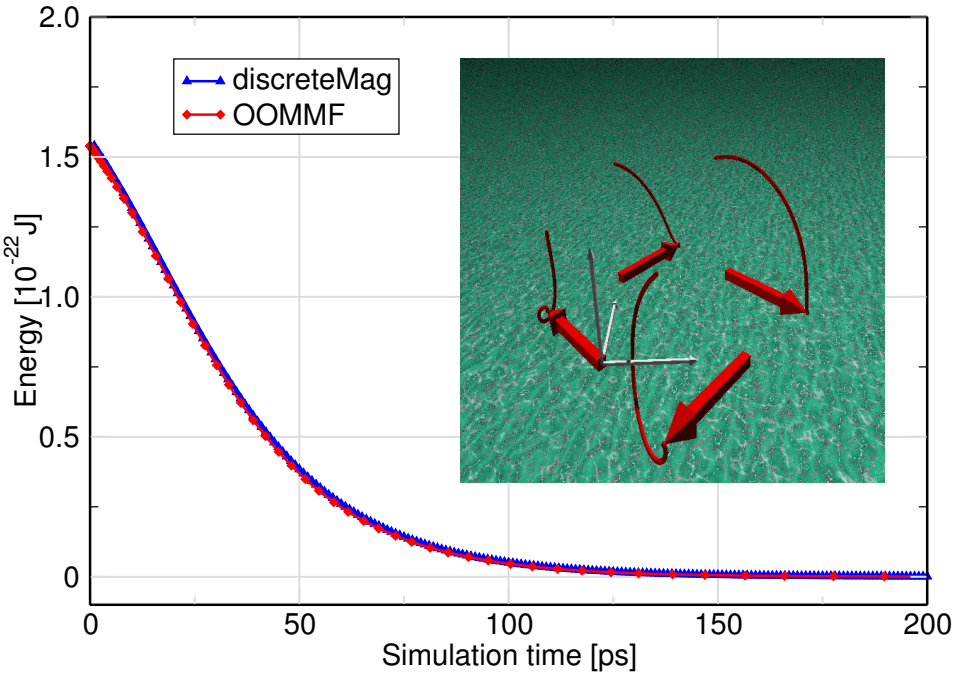

Figure 4.8: Comparison of the energy dynamics as a result of OOMMF and discreteMag for sole dipolar interaction. The inset depicts the trajectories (red curved tubes) of $2 \times 2 = 4$ spins (red arrows) for $\alpha = 1.6$. The coordinate axes are represented by the white arrow. In the final equilibrium state, the spins form a vortex.

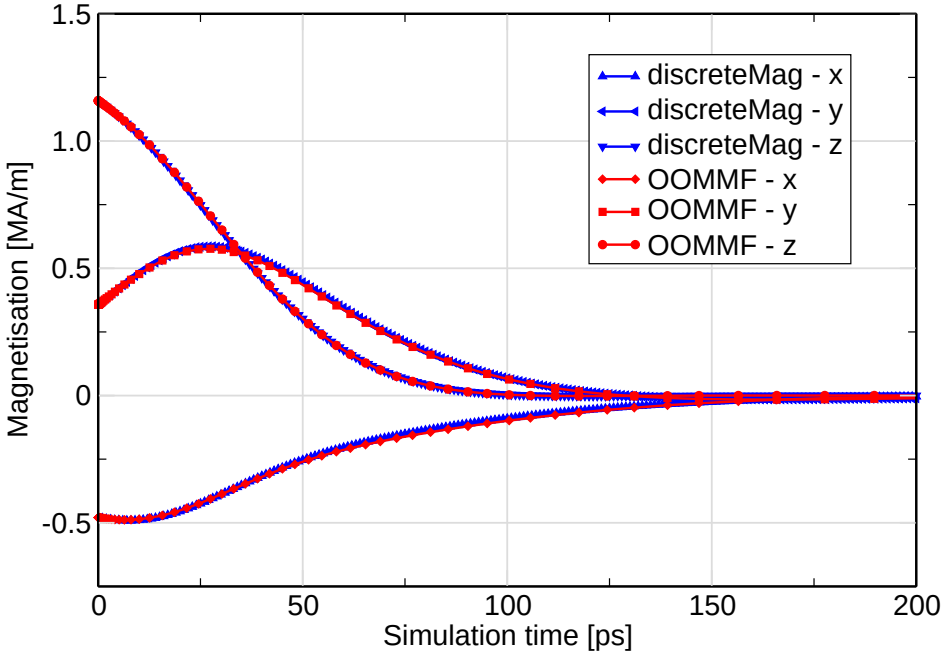

Figure 4.9: Comparison of the dynamics of the $\mathrm{x}, \mathrm{y}, \mathrm{z}$ magnetisation components as a result of OOMMF and discreteMag for sole dipolar interaction.

atomic structure of the material, but small enough to neglect demagnetising effects in comparison to exchange interaction and uniaxial anisotropy. The dimensions are thought to be smaller than the exchange length, so that the system behaves as a single domain. The exchange energy is constant then, and is ignored. We apply a field $\boldsymbol{H}_{\mathbf{app}}$ along the z direction and sweep it from +z to -z. The uniaxial anisotropy direction (constant K) is in the xz plane, off the $\pm$ z direction by an angle θ_{anis}. We find a total energy density

$$\varepsilon_{\mathrm{SW}} = -K\cos^2(\theta_{\mathrm{anis}} - \theta_{\mathrm{mag}}) - \mu_0 M_{\mathrm{sat}} H_{\mathrm{app}} \cos(\theta_{\mathrm{mag}}) \quad , \tag{4.1}$$

with the angle θ_{mag} enclosed by the magnetisation $\boldsymbol{M}$ and the +z direction, and the saturation magnetisation $M_{\mathrm{sat}} = |\boldsymbol{M}|$. Details can be found in *Blundell* (2001, chap. 6.7.8). We consider two cases:

Case A: θ_{anis} = 90°

When the uniaxial anisotropy direction is perpendicular to the direction of the applied field ($\theta_{\mathrm{anis}} = 90°$), the magnetisation can be derived analytically as a function of the applied field. For this, the relevant magnetic energies, Zeeman energy plus anisotropy energy, as stated by $\varepsilon_{\mathrm{SW}}$ in equation (4.1), are minimised. Introducing a dimensionless applied field parameter $h(H_{\mathrm{app}})$ as

$$h = \frac{\mu_0 M_{\mathrm{sat}} H_{\mathrm{app}}}{2K} \quad , \tag{4.2}$$

the z component of the magnetisation, $M(h) = M_{\mathrm{sat}} \cos(\theta_{\mathrm{mag}}(h))$, is

$$\begin{aligned} M(h) = \mathrm{const} = \pm M_{\mathrm{sat}} \qquad & \text{for} \qquad |h| > 1 \\ M(h) = M_{\mathrm{sat}}\, h \qquad & \text{for} \qquad |h| \leq 1. \end{aligned} \tag{4.3}$$

The magnetisation stays aligned with the applied field for $|h| > 1$ ($|H_{\mathrm{app}}| > \frac{2K}{\mu_0 M_{\mathrm{sat}}}$), and then rotates towards the opposing direction at a constant pace. The simulation data can be seen in figure 4.10 on the following page. Both OOMMF and discreteMag practically match the analytical solution (4.3). A marginal deviation is visible in the slightly rounded edges at $h = \pm 1$, contrary to the sharp edge of the analytical solution. The sequence of dynamic steps of the complete field sweep can be seen in the inset of 4.10 as a result of discreteMag: the trajectories for each field step are short, linking the metastable states of the magnetisation in a straight way to form a half circle that indicates the gradual reversal path.

Case B: θ_{anis} = 30°

The angle between the uniaxial anisotropy direction and the $\pm$ z direction (the direction of the applied field) is now set to $\theta_{\mathrm{anis}} = 30°$. No closed analytical form of

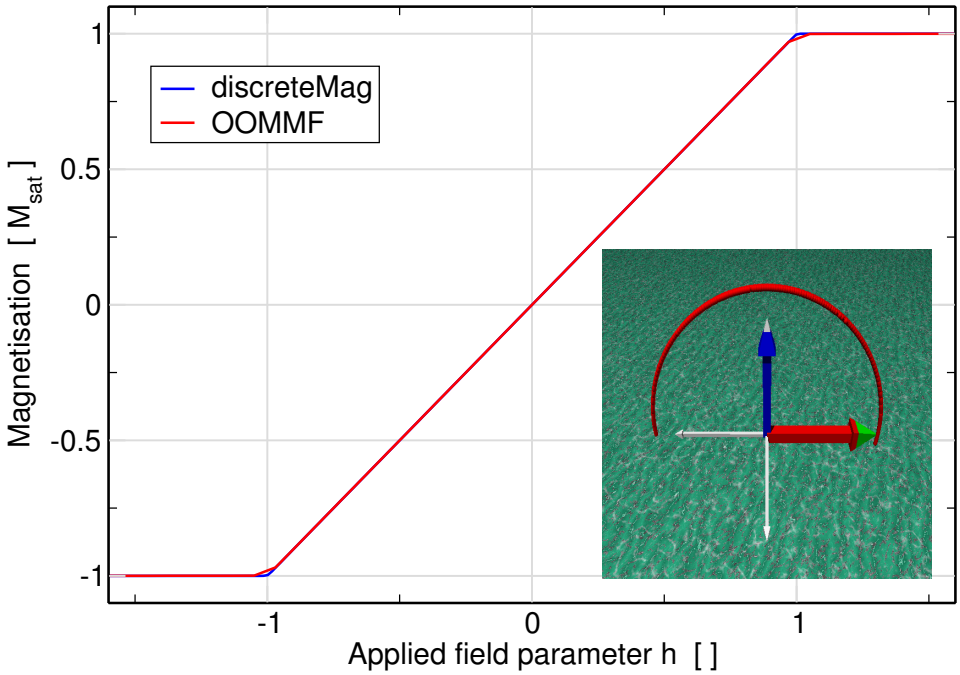

Figure 4.10: OOMMF and discreteMag magnetisation curves for the Stoner-Wohlfarth 90° case. The inset shows the coordinate system (white arrows), the uniaxial anisotropy direction (blue arrow) in +x, as well as the applied field vector (green arrow) in -z and magnetisation (red arrow) as at the complete field reversal from left to right. The winding red line marks the successive trajectories of the magnetisation when advancing to the next field sweep state.

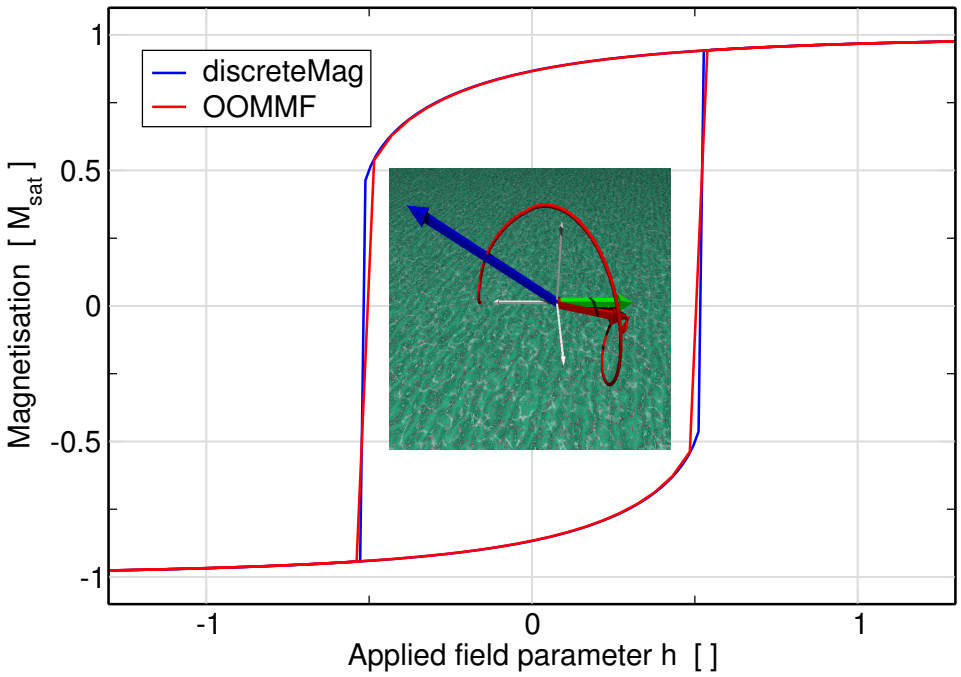

Figure 4.11: OOMMF and discreteMag magnetisation curves for the Stoner-Wohlfarth 30° case. The uniaxial anisotropy direction (blue arrow) is now at an angle of 30° off the z direction in the xz plane. The vector representation of the coordinate axes, applied field, and magnetisation is unchanged to figure 4.10 on the previous page.

the magnetisation function $M(h)$ exists in this case to solve equation (4.1). However, numerical treatment reveals the qualitative behaviour: at high applied fields ($h > 1$), the magnetisation is almost saturated ($M \approx M_{\mathrm{sat}}$), gradually declining for lower fields to $M \approx 0.5\, M_{\mathrm{sat}}$ at $h \gtrsim -0.5$. Then, the magnetisation switches to almost negative saturation, manifested in a sharp step of the magnetisation loop at $h \approx -0.5$. In figure 4.11, the simulation results of OOMMF and discreteMag expose the right properties. Again, the inset shows the sequence of trajectories for one field sweep based on discreteMag data. The magnetisation gradually rotates into the easy direction of the anisotropy. Then the reversed field yanks the magnetisation to the other side, producing the one large gyrating trajectory. From there on, the magnetisation steadily wanders into its final direction.

4.5 Conclusions

DiscreteMag reproduces data generated by OOMMF for simple test cases, building confidence in the abilities of OOMMF and justifying its usage for scientific applications as demonstrated in chapters 6 to 8 of this thesis.

Chapter 5

Magnetic exchange spring systems

5.1 Introduction

We now discuss general aspects of the so-called exchange spring systems. This provides the foundations for the understanding of the results that are presented in chapters 6 to 8.

We distinguish between different types of exchange spring systems in section 5.2: systems with rigidly coupled hard and soft layers (5.2.1), systems with an inhomogeneous magnetisation configuration during the reversal (5.2.2), and a special case of the latter, systems with antiferromagnetically coupled layers (5.2.3). The historical key results are discussed for each case. Finally, potential applications are outlined in section 5.3.

5.2 Basic concept of exchange spring systems

Exchange spring systems are magnetic heterostructures that consist of magnetically hard and soft compounds that are exchange coupled across the compound interfaces. Various nanostructures have been devised, typically clustered structures where soft inclusions are embedded into a hard matrix (figure 5.1a), or multilayered systems of alternating hard and soft layers (figure 5.1b). In the following, we will focus on the latter.

The nature of the magnetic reversal processes depends on the geometry of the system, the dimensions of the compounds, and their intrinsic material properties. However, it has been theoretically shown that the crucial factor is the dimension of the soft compound (*Fischer et al.*, 1998, *Leineweber and Kronmüller*, 1997). For a layered model system with a thickness of the soft layers t_s, the magnetisation of the soft compound is rigidly coupled to the hard compound as long as t_s does not exceed a critical value that is roughly the Bloch domain wall δ_h width of the hard

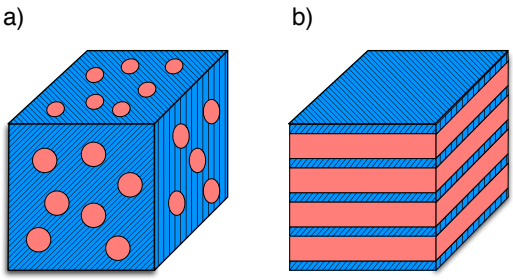

Figure 5.1: Types of exchange spring systems, with magnetically hard (blue) and soft (red) material. a) clustered structure b) multilayered structure

compound:

$$t_{\mathrm{s}} \lesssim \delta_{\mathrm{h}} = \pi\sqrt{\frac{A_{\mathrm{h}}}{K_{\mathrm{h}}}} \quad , \tag{5.1}$$

where A_{h} is the exchange constant and K_{h} the uniaxial anisotropy constant of the hard compound. The soft and hard layers switch together, and the hysteresis loop is a rectangle. For systems with sufficiently thick soft layers, *i.e.* $t_{\mathrm{s}} \gtrsim \delta_{\mathrm{h}}$, the soft layers start nucleating and reverse inhomogeneously before the hard layers switch. Next, both scenarios are described in more detail.

5.2.1 Rigidly coupled systems

The interest in nanostructured systems with rigidly coupled hard and soft layers stems from the prospect of permanent magnet materials with huge energy storage capacities. This capacity is described by the maximum energy product $(BH)_{\mathrm{max}}$ which is subsequently introduced.

A hysteresis loop characterising the magnetic behaviour of a ferromagnetic material is either depicted as a plot of the magnetisation M as a function of the applied field H_{app} [1] (normally used in this thesis), or as a plot of the magnetic induction B as a function of H_{app} (see figure 5.2 on the following page). The plots are correlated by the relation $B = \mu_0(H_{\mathrm{app}} + M)$, resulting in the inclination of the lines in the $B(H_{\mathrm{app}})$ plot. For a rectangular curve $M = M_{\mathrm{sat}}$ for $H_{\mathrm{app}} > {}_M H_{\mathrm{c}}$ and $M = -M_{\mathrm{sat}}$ elsewhere, the corresponding $B(H_{\mathrm{app}})$ curve is a straight line with constant positive gradient in the second quadrant. The general energy density of a magnetic field in matter is $\epsilon_{\mathrm{mag}} = -\frac{1}{2}BH_{\mathrm{app}}$ (*Jackson*, 1999). The point of maximum energy density $(BH)_{\mathrm{max}}$ on a hysteresis loop is then obtained by solving

$$\frac{\mathrm{d}}{\mathrm{d}H_{\mathrm{app}}}[BH_{\mathrm{app}}] = \frac{\mathrm{d}}{\mathrm{d}H_{\mathrm{app}}}[\mu_0(H_{\mathrm{app}}^2 + M_{\mathrm{sat}}H_{\mathrm{app}})] = 0 \tag{5.2}$$

[1] The *applied field* can refer to either magnetic induction B_{app} (unit Telsla, T), or to magnetic field strength H_{app} (unit amperes/meter, A/m). As the applied field is the *vacuum* field inside the external magnet in absence of the magnetic probe, B_{app} and H_{app} are proportionally related by $B_{\mathrm{app}} = \mu_0 H_{\mathrm{app}}$, and are equally suitable for use as abscissa on a hysteresis loop.

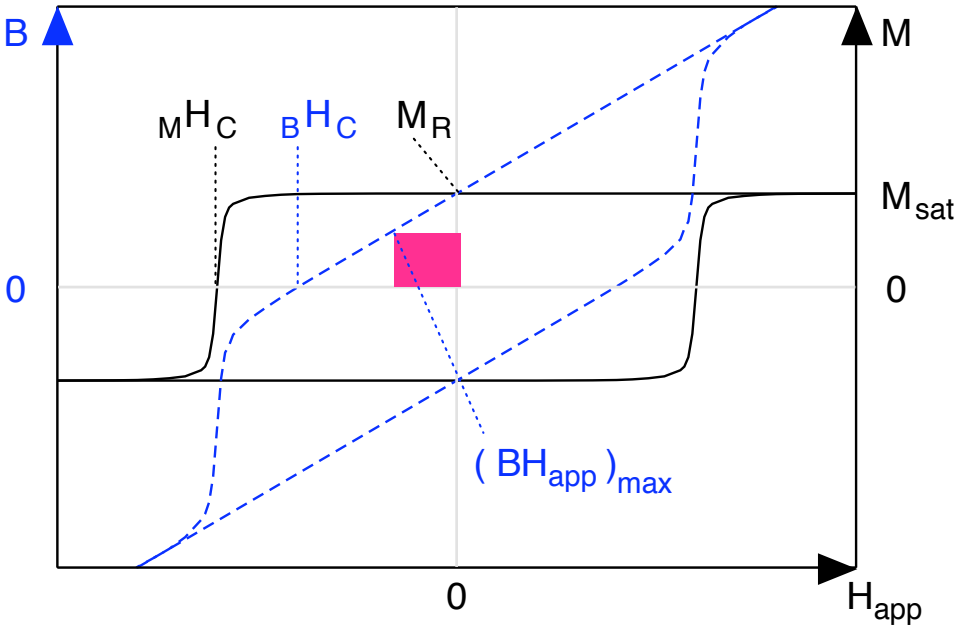

Figure 5.2: Representations of hysteresis loops: 1) Magnetisation M as a function of the applied field H_{app} (black solid lines). For high applied fields, the magnetisation converges to M_{sat}, the saturation magnetisation. The magnetisation for zero applied field is called the remanence M_{R}. The coercive field with respect to the magnetisation ${}_MH_{\mathrm{c}}$ is the applied field where the magnetisation is zero. 2) Magnetic induction B as a function of the applied field H_{app} (blue dashed lines). The coercive field with respect to the induction ${}_BH_{\mathrm{c}}$ is the applied field where the induction is zero. In this thesis, we refer to ${}_MH_{\mathrm{c}}$ by default for coercive fields. The red box is the graphical representation of the maximum magnetic energy density $(BH)_{\mathrm{max}}$ during a magnetisation cycle.

for H_{app}. This maximum point is found at $H_{\mathrm{app}} = -\frac{1}{2}M_{\mathrm{sat}}$ with

$$(BH)_{\max} = \frac{1}{4}\mu_0 M_{\mathrm{sat}}^2 \quad , \tag{5.3}$$

under the premise that the magnetisation reversal does not take place before the point of maximum energy density is reached, or in other words, that ${}_M H_{\mathrm{c}} \geq \frac{1}{2}M_{\mathrm{sat}}$. Strictly speaking, $(BH)_{\max}$ is negative, but we implicitly apply the modulus. The maximum energy density for arbitrary $M(H_{\mathrm{app}})$ curves is generally limited to $\frac{1}{4}\mu_0 M_{\mathrm{sat}}^2$, as obtained for a rectangular $M(H_{\mathrm{app}})$ loop (*Fullerton et al.*, 1999).

From equation (5.3) we derive that optimising the maximum energy product involves identifying materials with high saturation magnetisation and sufficient coercive fields. Research has focussed on developing high-performance magnets of binary or ternary rare earth / transition metal / boride or nitride compounds like $NdFe_{14}B$ or $Sm_2Fe_{17}N_3$ (*Long and Grandjean*, 1991). The rare earth atoms with their huge anisotropy provide the required coercivity at the cost of a reduced saturation magnetisation of the compound material.

The approach of *Kneller and Hawig* (1991) is to use a nanocomposite of regions of exchange-coupled magnetically hard and soft materials, the magnetic exchange spring systems. The hard compound serves as the rigid skeleton against demagnetisation while the soft compound provides the high saturation magnetisation. By this construction, the fraction of the rare earth material is kept at a minimum, optimising manufacturing costs and corrosion resistance. *Coehoorn et al.* (1988) was the first to experimentally investigate such a system.

Skomski and Coey (1993) predicted a maximum energy product of 1 MJ/m^3 =120 MG Oe for multilayers of hard $SM_2Fe_{17}N_3$ and soft $Fe_{65}Co_{35}$ with an atomic rare earth fraction of 5 %. *Fullerton et al.* (1998) performed simulations based on a model where the bilayer structure is divided into a sum of atomic layers, and the bilayer is treated as a one-dimensional chain of spins, each spin representing one layer. They confirmed the numerical results by experiments for Sm-Co/Fe and Sm-Co/Co bilayers, estimating a maximum energy product of 80 MG Oe. *Sabiryanov and Jaswal* (1998) conclude values for $(BH)_{\max}$ of the same order of magnitude for $SmCo_5/Co_{1-x}Fe_{1-x}$ by ab-initio calculations. All these results highlight the potential of exchange spring systems to maximise $(BH)_{\max}$.

5.2.2 Systems with inhomogeneous reversal behaviour

For systems with sufficiently thick magnetically soft layers, eq. (5.1) does not hold any more, and the magnetisation reversal in the soft compound takes place in an inhomogeneous way at fields below that of the hard layers. Consequently, the coercive field is reduced, deteriorating the hard-magnet properties. Instead, interest focuses on the process of the exchange spring reversal itself.

Goto et al. (1965) theoretically studied the reversal characteristics of a soft magnetic layer without anisotropy that is ferromagnetically coupled to an extremely hard and rigid substrate. He found that the system stays in a ferromagnetic alignment as long as the opposing applied field is lower than the so-called characteristic bending field H_b with

$$H_\mathrm{b} = -\frac{\pi^2 A}{2 M_\mathrm{sat}\, t_\mathrm{s}^2} \quad , \tag{5.4}$$

where A is the global exchange constant and M_sat is the saturation magnetisation of the soft layer. When the applied field exceeds the bending field, a differential rotation in the soft layer sets in: a Bloch domain wall-like structure is formed, with the magnetisation pinned to the hard layer at the interface, and relatively free to wind towards the applied field direction in the interior of the soft layer.

Figure 5.3 on the next page illustrates Goto's findings, generalised to a soft layer sandwiched between two hard layers. The magnetisation curve shows a flat part with values close to M_sat for positive applied fields and negative applied fields up to H_b, according to the ferromagnetic spin structure 5.3 ①. For $H < H_\mathrm{b}$, the increasing differential rotation in the soft layer 5.3 ② ③ is reflected in the reversible area of the hysteresis loop. Finally, the system becomes unstable, and the hard layer switches into the opposite easy axis direction at the switching field H_s. All spins are then aligned with the applied field direction, resuming a ferromagnetic configuration in 5.3 ④.

Goto also coined the term ***exchange spring*** by designing the mechanical analogue of dual uniaxial films in form of a torsion spring. Both the simplified magnetic bilayer system and the torsion spring analogue obey energy equations of corresponding structure.

Bowden et al. (2000) recalculated the bending field based on the model of discrete atomic layers earlier used by *Fullerton et al.* (1998). He found a layer thickness dependence of the bending field corresponding to eq. (5.4), $H_\mathrm{b} \propto \frac{1}{N^2}$, with the number of atomic layers N. Asti *et al.* derived magnetic phase diagrams in terms of layer thicknesses by calculating the differential susceptibility at a nucleation field. In their one-dimensional models, uniaxial anisotropies were assumed with easy axes either in (*Asti et al.*, 2004) or perpendicular to (*Asti et al.*, 2006) the film plane.

5.2.3 Antiferromagnetically coupled layers

When the interface coupling of the soft and hard layers is antiferromagnetic instead of ferromagnetic, the sequence of the spin states during a reversal changes. Figure 5.4 on page 63 sketches hysteresis loop and spin states for a trilayer model system. Here, the exchange spring configuration with the Bloch domain wall-like structure occurs at high applied fields. The hard top and bottom layers are aligned

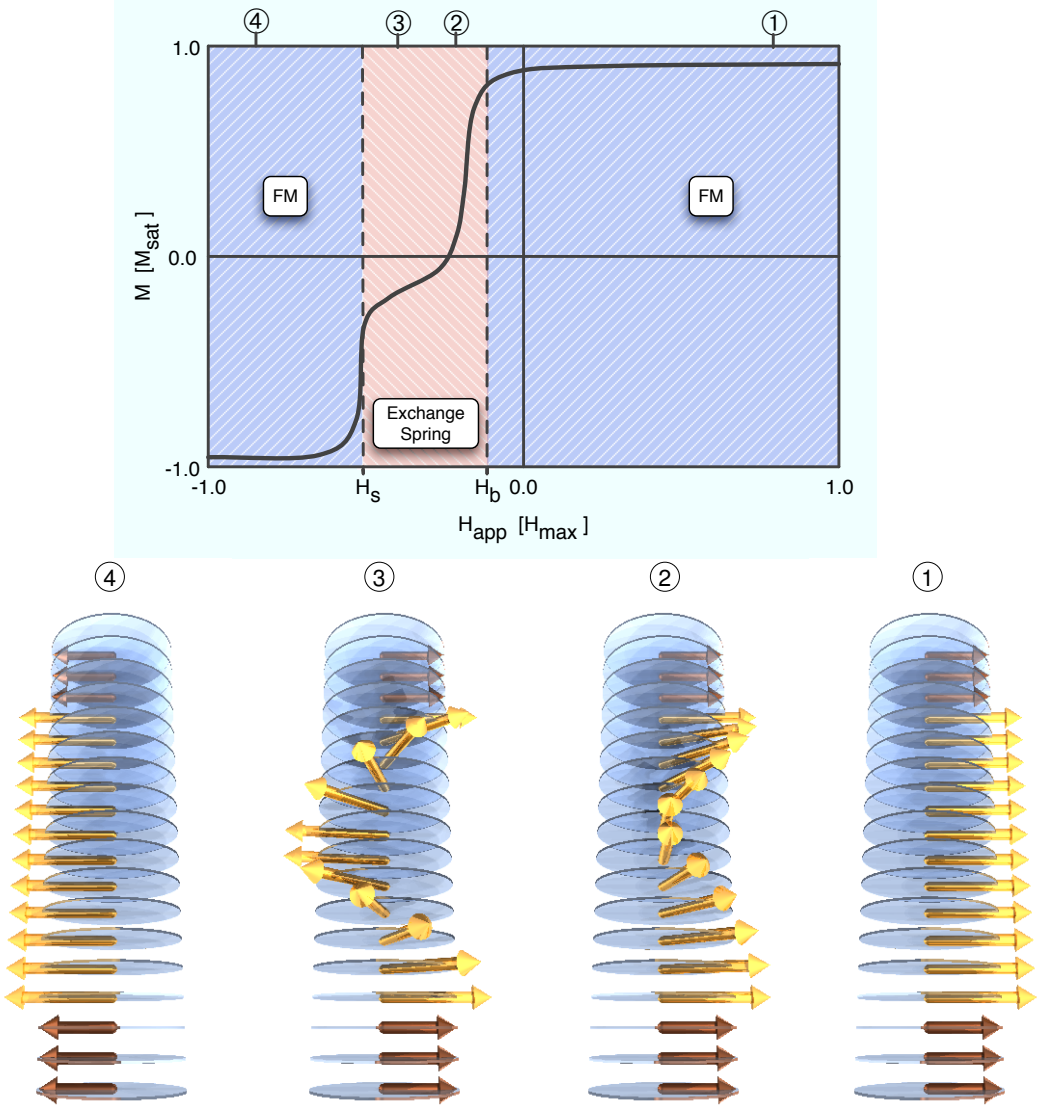

Figure 5.3: Model hysteresis loop and spin schematics of a FM exchange spring system. Two blue shaded areas in the hysteresis loop are marked *FM* to indicate a ferromagnetic spin configuration, a red shaded area is marked *Exchange Spring* as the spin configuration in the soft layer is wound towards the applied field direction like a torsion spring. The circled numbers on the top of the hysteresis loop refer to the spin schematics in the bottom row. In either plot, the horizontal planes are depicted as blue glass discs, and the arrows represent the homogeneous magnetisation in each plane. The longer golden coloured arrows are the magnetisation vectors in the soft layer, the shorter copper coloured arrows in the hard layer.

with the applied field, pinning the interface area in the sandwiched soft layer into an antiferromagnetic direction. In the interior of the soft layer, the magnetisation gradually twists towards the applied field. The higher the applied field, the stronger the twist in the soft layer, the larger the magnetisation — see states 5.4 ① and ②. Due to the antiferromagnetic coupling, the bending field H_{b} is positive. This implies that the remanent state is an antiferromagnetic alignment of the moments as in 5.4 ③. The antiferromagnetic alignment holds until the negative applied field exceeds the switching field H_{s}. Then the hard layers switch towards the applied field and wind up the soft layers (state 5.4 ④).

The technical realisation requires identifying magnetically hard and soft materials that effectively couple antiferromagnetically at the interface. The approach by the Magnetic Materials group at the School of Physics and Astronomy at the University of Southampton is to use single-crystal Laves phase (*Laves*, 1956) $REFe_2/YFe_2$ samples (RE = rare earth element, details in section 6.2) that are grown by Dr Roger C. C. Ward, Clarendon Laboratory, University of Oxford, using molecular beam epitaxy (MBE) methods. The material properties are described in detail in the subsequent chapters 6 to 8. The relevant interactions are the dominant ferromagnetic Fe-Fe exchange (≈ 600 T) inside and across the layers, the antiferromagnetic Fe-RE exchange (≈ 100 T) in the $REFe_2$ layers, and the RE crystal field anisotropy (≈ 10-100 T) (*Gordeev et al.*, 2001a). Consequently, the effective moments in the $REFe_2$ and YFe_2 layers are subject to antiferromagnetic coupling across the interface.

Figure 5.5 on page 64 sketches the coupling behaviour for typical spin states, depicting the magnetic moments of the constituent materials: Fe moments (red, short) in both the YFe_2 and $REFe_2$ compounds, RE moments (blue, long) in $REFe_2$, and effective moments (green, bold) in $REFe_2$ as a result of the geometrical addition of the respective Fe and RE moments. When the applied field H_{app} is between the negative switching field H_{s} and the positive bending field H_{b} (state 5.5a), the spin coupling is obvious: the Fe moments align ferromagnetically inside and across the compound interfaces. The RE moments are antiferromagnetically coupled to the Fe moments in $REFe_2$, and the effective moments are antiferromagnetically oriented with respect to the Fe moments as well. The ferrimagnetic state 5.5a corresponds to figure 5.4 ③, and the state of exchange spring winding 5.5b to figure 5.4 ②. State 5.5c illustrates a spin flop structure, where the spins point perpendicular to the film plane. This structure is caused by a complex crystal anisotropy that favours an out-of-plane alignment of the magnetisation, and usually occurs at an intermediate applied field H_{sf}. The extreme case of an almost infinite applied field is shown in figure 5.5d. All Fe spins in the YFe_2 layer are aligned with the field, as are the RE spins. According to the model used in subsequent chapters, the Fe-RE exchange is approximated to be infinite, causing the Fe spins in $REFe_2$ to align against the field direction. Consequently, the neighbouring Fe spins at the interface are frustrated with regard to Fe-Fe exchange.

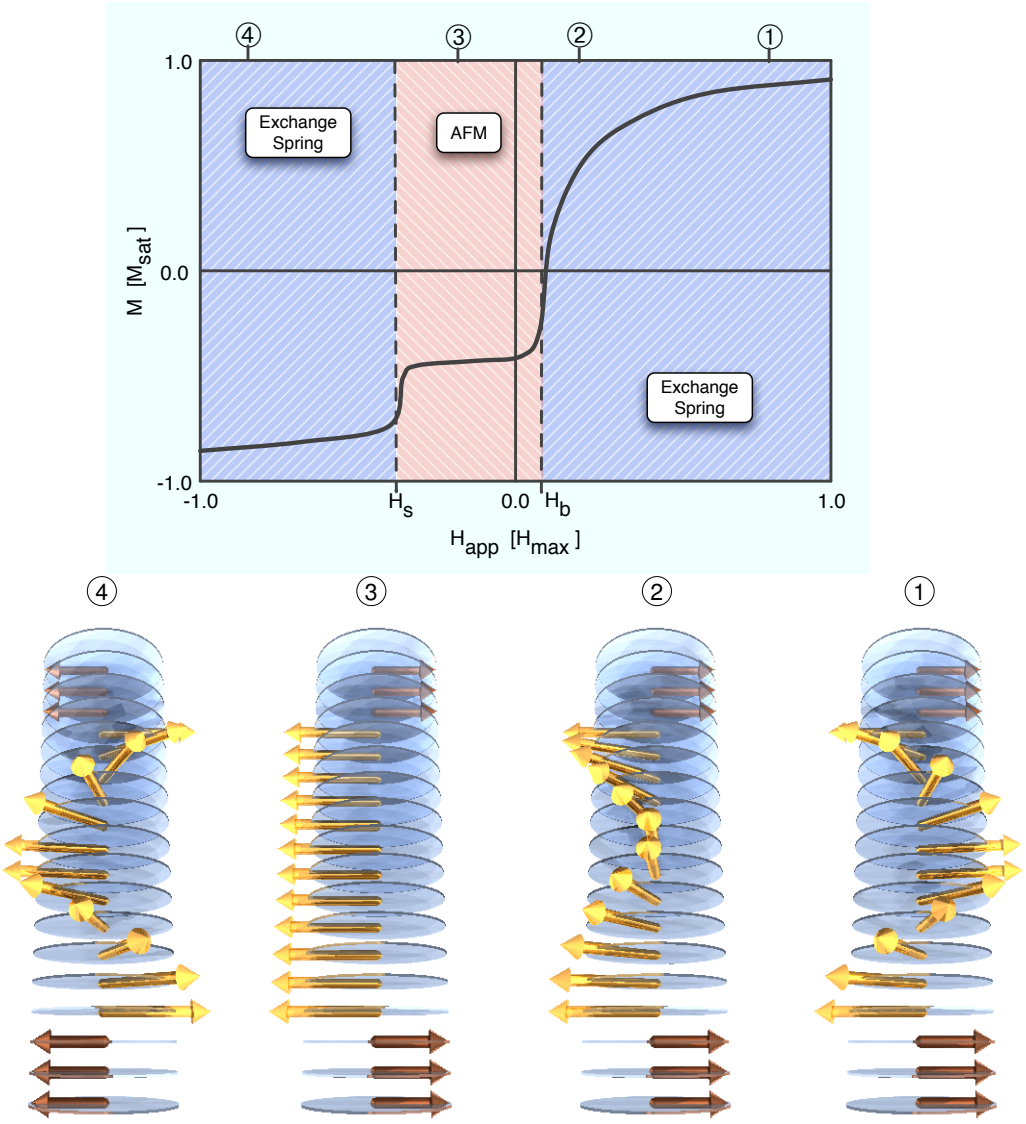

Figure 5.4: Model hysteresis loop and spin schematics of an AFM exchange spring system. Two blue shaded areas in the hysteresis loop are marked *Exchange Spring* to indicate an exchange spring-like configuration, a red shaded area is marked *AFM* to highlight the antiferromagnetic configuration in this region. The remaining description of the figure corresponds to figure 5.3 on page 61.

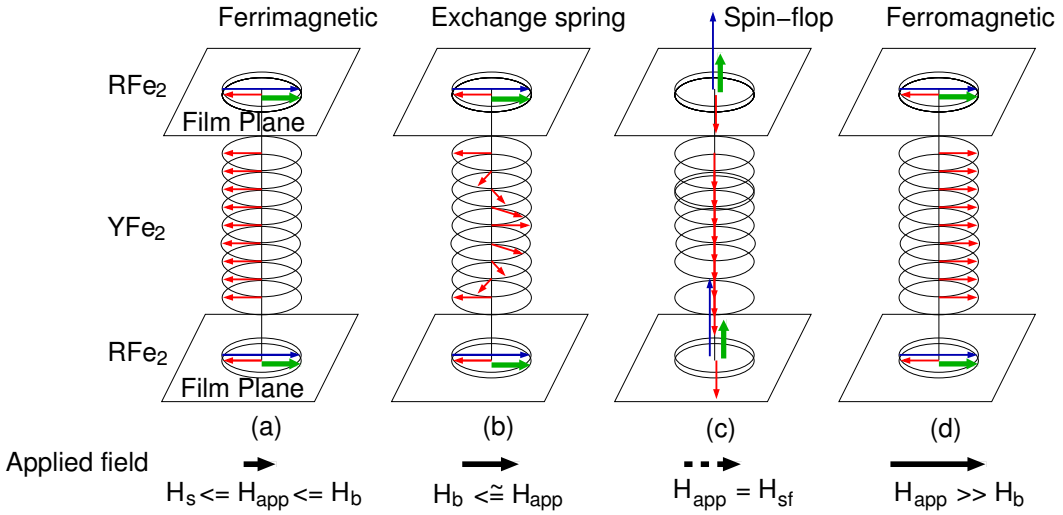

Figure 5.5: Spin schematics of four states in a $REFe_2/YFe_2$ exchange spring system. The short arrows (red) characterise the iron moments, the long arrows (blue) the rare earth moments, and the bold arrows (green) the effective moment in the $REFe_2$ layers. The arrows below each scheme (black) indicate the applied field.

The characteristics of antiferromagnetically coupled exchange spring systems suggest usage for the design of novel applications as they can be engineered to specific magnetic properties. In particular, $DyFe_2/YFe_2$ samples have been manufactured

- to a specified coercive field H_c in the range $H_\mathrm{c}(\mathrm{DyFe_2}) \leq H_\mathrm{c} \leq \infty$ (*Sawicki et al.*, 2000a)
- to a target bending field H_b, following the dependence $H_\mathrm{b} \propto \frac{1}{d_\mathrm{s}^2}$, with d_s being the thickness of the soft layers (*Sawicki et al.*, 2000b)
- at the magnetic compensation point ($M_\mathrm{s}t_\mathrm{s} = M_\mathrm{h}t_\mathrm{h}$), with M_s and M_h denoting the saturation magnetisation of the soft and hard material, and t_s and t_h the according layer thicknesses (*Sawicki et al.*, 2000c)
- with tailored negative coercivity (*Beaujour et al.*, 2001a,b, *Gordeev et al.*, 2001a).

5.3 Applications

The usage of exchange spring systems as high-performance permanent magnets was already explained in subsection 5.2.1. One area that could strongly profit from such magnets is the development of microelectromechanical systems (MEMS). MEMS are widely used as actuators and sensors already, with the the automotive airbag deployment sensor as the most prominent representative. The ongoing

miniaturisation of MEMS promotes the development of magnetic MEMS (MagMEMS) devices as microsensors and microactuators, since magnetostatic interactions dominate over electrostatic effects on a nanometre scale. Several topical reviews exist (*Cugat et al.*, 2003, *Gibbs et al.*, 2004, *Niarchos*, 2003). Coils are economically and technically not viable as a magnetic flux generator in MagMEMS. Instead, exchange spring magnets, when tailored for a giant energy product and magnetic hardness, could create high displacement rates in actuators, or high signal output in sensors, respectively.

Exchange spring systems also attract attention as potential candidates for novel storage media with ultra high storage densities in the field of hard disk development. Conventional hard disks store information in the magnetic orientation of magnetically hard grains with a reversal mechanism of a Stoner–Wohlfarth particle. Exchange spring magnets have additional degrees of freedom in form of domain walls present in the soft layers, and the soft elements facilitate the switching of the hard elements. This proves beneficial for use as storage media in various ways: *Ando and Nishihara* (1997) implemented an exchange spring triple layer for perpendicular recording media in order to achieve a high signal-noise ratio and signal stability. *Victora and Shen* (2005) suggested the usage of exchange spring multilayers as perpendicular magnetic recording media in order to facilitate the fabrication and to improve magnetic switching properties. *Suess et al.* (2005a,b) showed that the thermal stability of exchange spring recording media can be improved without increasing the coercive field, which is limited by the maximum field of the write head of roughly 1.7 T. For thermally assisted magnetic recording (TAR), *Thiele et al.* (2003) used exchange spring media to allow for easier writing under a reduced coercive field above a transition temperature.

In the field of spintronics, *Kiselev et al.* (2003) and *Xi et al.* (2005) reported on magnetic motions in a nanomagnet driven by a spin-polarised current, possibly serving as an easily tunable nanoscale microwave generator. With their well-defined interlayer domain walls stretching over vast parts of the multilayer, exchange spring systems are highly suitable for such devices, providing high spin torque yields. They have been suggested for use as GMR spin devices (*Gordeev et al.*, 2001b) and as devices exploiting the magnetomechanical properties (*Mougin et al.*, 2000). Furthermore, the spin torque emerges useful in order to manipulate switching states at comparably small applied fields (*Zhang et al.*, 2002).

Chapter 6

Magnetic $DyFe_2/YFe_2$ exchange spring systems

The work on $DyFe_2/YFe_2$ exchange spring simulations described in this chapter has been published in *Journal of Applied Physics* (*Zimmermann et al.*, 2006).

6.1 Introduction

Magnetic measurements of [110] [50ÅDyFe_2/200ÅYFe_2] [1] reveal a rich switching behaviour: the formation of exchange springs in this system of alternating hard and soft layers can be observed for low temperatures. For high temperatures, the appearance of the hysteresis loop changes significantly, implying a more complicated reversal process.

First of all, the general crystalline and magnetic basics of $REFe_2$ superlattices are described in section 6.2. We focus on spin coupling aspects and the resulting effective magnetisation (6.2.1), the exchange interaction (6.2.2), and the magnetic anisotropy (6.2.3). The method for the investigation of the particular [50ÅDyFe_2-/200ÅYFe_2] system is presented in sections 6.3 and 6.4. In section 6.5, we reproduce hysteresis loops for net and compound-specific magnetisation by means of micromagnetic simulations and assess the quality by a direct comparison to recent XMCD measurements. The high-temperature switching characteristics, showing an unexpected magnetisation reversal of the hard magnetic layer before the soft magnetic layer, are investigated and understood on the basis of detailed magnetic configuration plots. The crossover of low- to high-temperature switching patterns is explained by energy considerations, and the dependence on different parameters is outlined.

[1] Multilayered system of alternating layers of 50 Å $DyFe_2$ and 200 Å YFe_2, with a crystallographic [110] growth direction.

6.2 Crystalline and magnetic basics of $REFe_2$ superlattices

In this and the following chapters, we investigate models of superlattices composed of $DyFe_2$, $ErFe_2$, and YFe_2 multilayers. Dysprosium (Dy) and erbium (Er) are representatives of the element group of the rare earth metals. The term 'rare earth metal' is a trivial name for the lanthanides, the official name in accordance with the IUPAC (International Union of Pure and Applied Chemistry) nomenclature. The lanthanides comprise of the 15 elements with atomic numbers 57 to 71, a sequence from lanthanum to lutetium, with the additional electron placed into the 4f orbitals. The 4f orbitals with their low spatial extension have little influence on the resembling chemical properties of the lanthanides (*Mortimer*, 1987).

Confusingly, the term 'rare earths' is also used to denote the lanthanides excluding promethium, together with the chemically similar transition metals yttrium and scandium. In this thesis, we will stick to the former definition of rare earths.

A common property of those elements is the strong magnetocrystalline anisotropy due to the effects of the crystal field on the rare earth's $4f$ electron wave function. The magnetocrystalline anisotropy will play a crucial role in the following simulations. Yttrium (Y) and iron (Fe) are transition metals, bearing strong exchange coupling as a consequence of the large spatial extend of the 3d wave functions.

Bulk $REFe_2$ (with RE = Dy, Er) and YFe_2 crystallise in a Laves phase, a face-centred cubic diamond structure with eight $REFe_2$ units per cubic unit cell. A $REFe_2$ unit cell is schematically depicted in figure 6.1 on the following page.

6.2.1 Effective magnetisation

$REFe_2$ are ferrimagnets, and for the computational modelling we assume a rigid ferromagnetic Fe-Fe and antiferromagnetic Fe-RE coupling inside a crystal cell. This allows us to calculate an effective or net magnetisation of $REFe_2$ by subtracting the magnetisation of Fe from that of RE. In the YFe_2 layers, the magnetisation of Y is negligible, and Fe solely contributes to the net magnetisation of YFe_2. The total magnetisation M_{REFe2} of a $REFe_2$ unit cell (cell base length a) can thus be calculated as

$$M_{\mathrm{REFe2}} = |\,(8\,m_{\mathrm{RE}} - 16 m_{\mathrm{Fe}})\,| \,/\, a^3 \quad , \tag{6.1}$$

and for YFe_2 this simplifies to

$$M_{\mathrm{YFe2}} = 16\,m_{\mathrm{Fe}} \,/\, a^3 \quad , \tag{6.2}$$

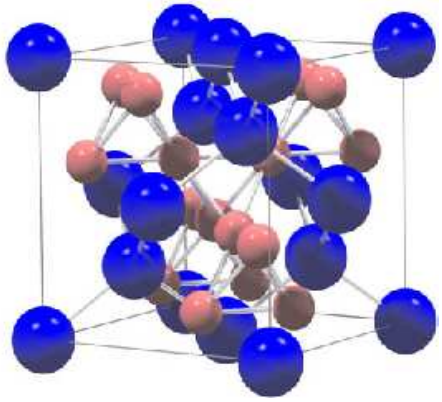

Figure 6.1: Schematic of a $REFe_2$ Laves phase unit cell, with RE being represented by the large (blue) spheres and Fe by the small (red) spheres (*Bentall and R. C. C. Ward*, 2003).

with $a = 0.7363$ nm for YFe_2 and $a = 0.7325$ nm for both $ErFe_2$ and $DyFe_2$ (*Bentall and R. C. C. Ward*, 2003). The magnetic moments m are temperature dependent. The values relevant for the simulations in chapters 6 and 7 can be looked up in table 6.1 on page 74. For a comprehensive listing, see appendix A.1.

6.2.2 Exchange interaction

Regarding the exchange interaction, we only consider the ferromagnetic coupling of the Fe atoms across crystal cells. This results in a positive intra-layer exchange coupling A_{i} for all compounds, a negative across-layer exchange coupling $A_{\mathrm{a(RE\text{-}Y)}}$ between the effective $REFe_2$ and YFe_2 moments, and a positive across-layer exchange coupling $A_{\mathrm{a(RE\text{-}RE)}}$ between the effective $ErFe_2$ and $DyFe_2$ moments to be discussed in chapter 8. The exchange constant used for pure iron is 2.5×10^{-11} J/m (*Suess et al.*, 2000). For the exchange constants of the compounds, we apply a finding from mean field theory: according to *O'Handley* (1999, page 121), the Curie temperature can be calculated by the Curie constant C_{C} and λ, $T_{\mathrm{C}} = \lambda C_{\mathrm{C}}$. The function λ is proportional to the Heisenberg exchange constant $\mathcal{J}$ of equation (3.27). Hence, the exchange constants for the compound materials are obtained by taking the value for pure iron scaled by the corresponding Curie temperatures, stated in *Buschow* (1977). As the simulation results are robust with respect to moderate variations of the exchange constants, we use the same intra-layer exchange constant of $A_{\mathrm{i}} = 1.46 \times 10^{-11}$ J/m for all three compounds, and the across-layer exchange constants $A_{\mathrm{a(RE\text{-}RE)}} = -A_{\mathrm{a(RE\text{-}Y)}} = A_{\mathrm{i}}$.

6.2.3 Magnetic anisotropy

For considerations of the magnetic anisotropy we introduce two coordinate systems: the laboratory system xyz and the system of the lattice cell with its basis

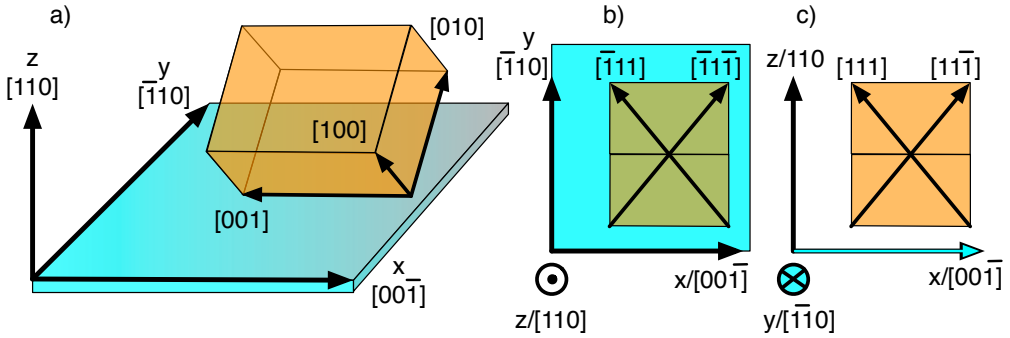

Figure 6.2: (a) Lattice cell (yellow cube) with respect to the film plane (blue). The lab system is spanned by the basis vectors $\boldsymbol{x}$, $\boldsymbol{y}$, $\boldsymbol{z}$, the lattice cell by [100], [010], [001]. The crystal is grown in the [110] direction. (b) In-film plane body diagonals of the lattice cell in an xy cross section (c), out-of-film plane body diagonals in an xz cross section.

vectors [100], [010], [001]. Both systems are interlinked by the crystal growth direction [110] which is the z direction of the lab system. The orientation of the lattice cell in the lab system is outlined in figure 6.2. Please see figure 6.3 on the next page for the correlation of film plane base directions, base directions of a [110] grown crystal, and body diagonals of the crystal.

The RE magnetocrystalline (MC) anisotropy of the bulk with the phenomenological parameters K_1, K_2, K_3 is described by the cubic anisotropy energy density (eq. (3.77)) in the lattice cell system:

$$\begin{aligned} \varepsilon_{\mathrm{a,MC}} = \quad & K_1 \left[\alpha_{100}^2\alpha_{010}^2 + \alpha_{100}^2\alpha_{001}^2 + \alpha_{010}^2\alpha_{001}^2\right] + \\ & K_2 \left[\alpha_{100}^2\alpha_{010}^2\alpha_{001}^2\right] + \\ & K_3 \left[\alpha_{100}^4\alpha_{010}^4 + \alpha_{100}^4\alpha_{001}^4 + \alpha_{010}^4\alpha_{001}^4\right] \quad , \end{aligned} \tag{6.3}$$

where α_{100}, α_{010}, α_{001} are the direction cosines of the magnetisation with respect to the crystal lattice directions [100], [010], and [001], as defined in subsection 3.3.3 on page 31 for arbitrary directions. The temperature dependent K_1, K_2, K_3 values are taken from calculations extending the Callen-Callen model to second order (*Martin et al.*, 2006a). The values relevant for the simulations in chapters 6 and 7 can be looked up in table 6.2 on page 75. For a comprehensive listing, see appendix A.2.

6.3 $DyFe_2/YFe_2$ simulations

The system studied in this section is a model of a [110] [50ÅDyFe_2/200ÅYFe_2]×27 Laves phase superlattice. It is sketched on the left side of figure 6.4 on page 71. Macroscopic magnetisation measurements as well as compound-resolved XMCD analysis (*Dumesnil et al.*, 2005, 2004) reveal a typical exchange spring magnetisation

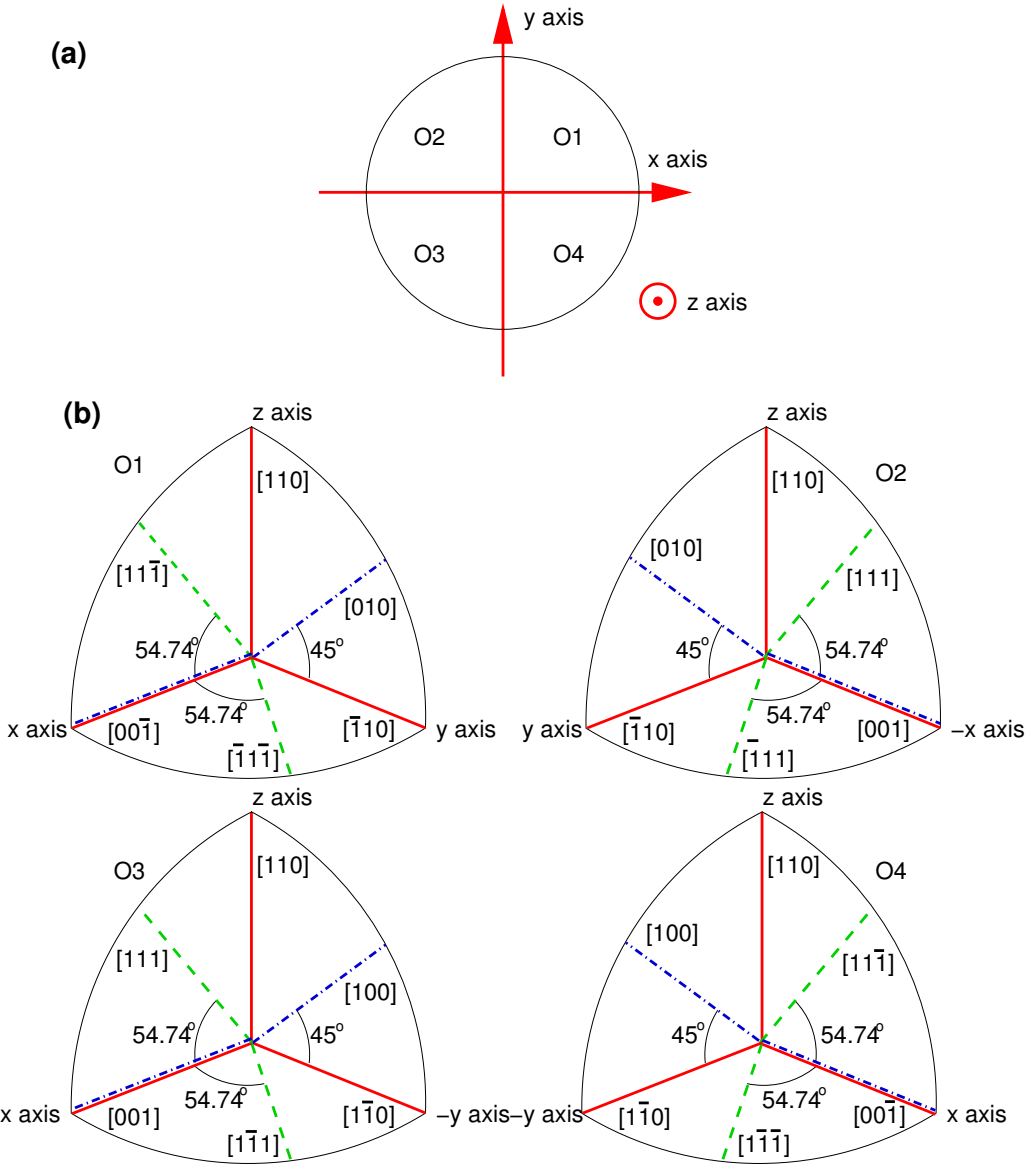

Figure 6.3: Bird's eye view (a) and individual perspective views (b) on upper four octants (O1 - O4) of a sphere marking the film plane base directions x,y,z (solid, red), base directions $\langle 001 \rangle$ of a [110] grown crystal (dotted dashed, blue), and body diagonals of the crystal $\langle 111 \rangle$ (dashed, green). Each octant is represented by three orthogonal planes, intersecting at the solid (red) lines.

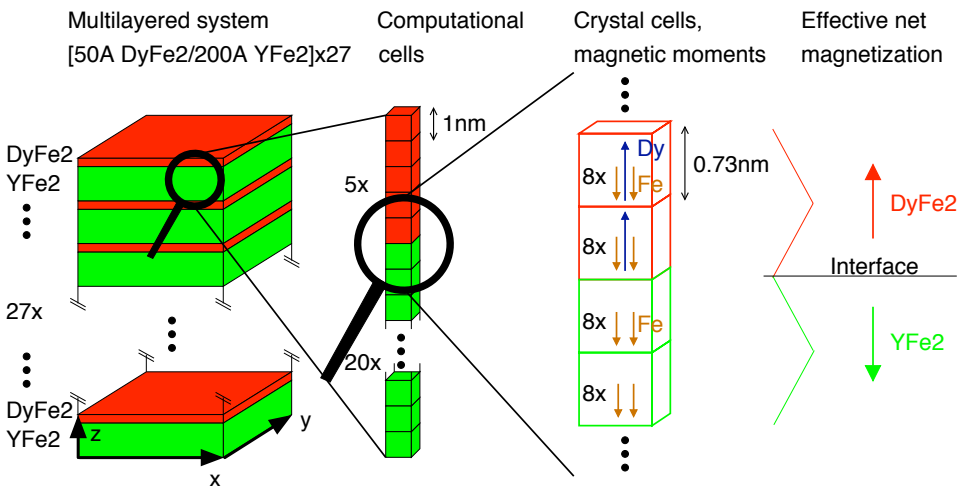

Figure 6.4: Sketch of the compound layers of the investigated [50ÅDyFe$_2$/200ÅYFe$_2$]×27 exchange spring system (left), and closeups showing the computational cells (centre) and the atomic spin coupling (right).

reversal for low temperatures and an unexpected switching behaviour with three irreversible switchings for high temperatures, where the hard magnetic layers reverse before the soft magnetic layers (figure 6.5 on the next page). We investigate the spin configuration of this interesting reversal behaviour by means of micromagnetic simulations. The resulting compound-specific and net hysteresis loops are presented and compared with experimental data. Good qualitative agreement legitimates the simulation data and allows the interpretation of resolved configuration plots that clarify the different switching behaviour.

6.4 Method

We use the OOMMF code to perform the micromagnetic simulations. The layer structure and the direction of the applied field $\boldsymbol{B}_{\text{app}} \parallel [\bar{1}10]$ correspond to *Dumesnil et al.* (2005, 2004). A cell size of 1 nm^3 provides sufficient resolution with respect to an exchange length of 3.4 nm. For computational feasibility, the magnetisation of each layer is represented by one cell (figure 6.4, centre). The simulations account for thermal effects by temperature-dependent magnetisation and anisotropy parameters. Owing to the one-dimensional character of the model with its limited xy resolution, demagnetising effects cannot be considered by explicit OOMMF methods as described in subsection 3.4.3. Instead, the thin film approximation of subsection 3.4.4 is applied.

The spin coupling is schematically depicted on the right side of figure 6.4: the Fe atoms are ferromagnetically coupled, effecting positive intra-layer and negative across-layer exchange coupling between the net moments (subsection 6.2.2). The magnetisation values are derived from equations (6.1) and (6.2), with input param-

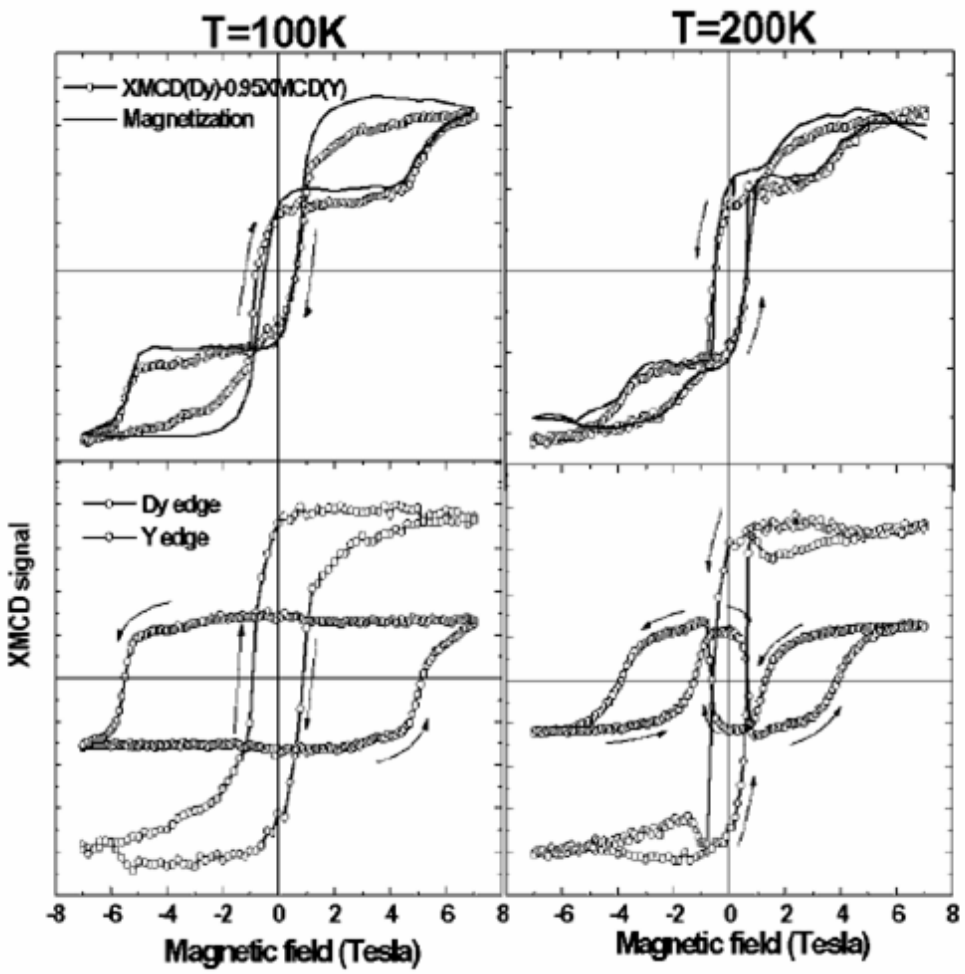

Figure 6.5: Experimental $DyFe_2$ hysteresis loops of the net (top) and compound-specific (bottom) magnetisation M_y for 100 K (left) and 200 K (right), as measured by *Dumesnil et al.* (2004). The compound-specific data in the bottom row was obtained by XMCD measurements at the Y and Dy edges. The solid lines in the top row are magnetic measurements of the net magnetisation, superimposed to a linear combination of the XMCD loops.

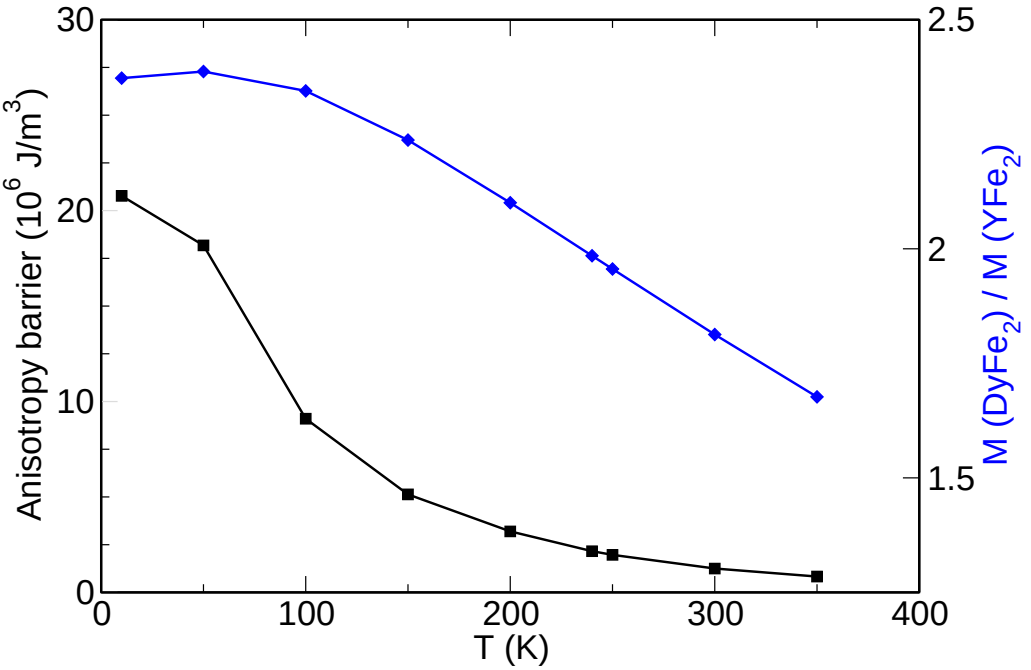

Figure 6.6: Dy anisotropy energy barrier dE (black squares) and the ratio of the net magnetisation of $DyFe_2$ to YFe_2 (blue diamonds, based on *Bleaney et al.* (1982), *Bowden* (2005), *Bowden et al.* (1968)) for various temperatures T.

Material	Magn. moment per atom / 0 K	Temperature normalisation	
	m_0 [μ_B]	T [K]	r_T[]
Dy	10	200	0.8762
		350	0.6867
Fe	1.5	100	0.9835
		200	0.9519
		350	0.8634
Y	0.0	–	–
Er	9.0	100	0.8905
		200	0.7210
		350	0.4884

Table 6.1: Magnetic moments for different bulk materials (*Bleaney et al.*, 1982, *Bowden*, 2005, *Bowden et al.*, 1968). To get an atomic magnetic moment for a given temperature T, the zero temperature magnetic moment m_0 has to be multiplied with the dimensionless temperature normalisation r_T: $m(T) = m_0\, r_\mathrm{T}(T)$.

eters listed in table 6.1. With increasing temperature, the magnetic moment of Dy diminishes faster than that of Fe, and the $DyFe_2$ and YFe_2 magnetisations tend to level (figure 6.6 on the previous page).

While we can ignore magnetic anisotropy for YFe_2, the anisotropy of $DyFe_2$ plays a crucial role in the understanding of the switching behaviour, bearing a magnetocrystalline contribution of the bulk Dy and a strain energy due to epitaxial effects. The bulk Dy anisotropy is manifested in the phenomenological cubic crystal constants K_1, K_2, K_3 of eq. (6.3); the values are extracted from *Atzmony and Dariel* (1976), with easy axes in $\langle 100 \rangle$. The strain term d_xy of eq. (3.89) gets increasingly important for higher temperatures: up to 170 K, the easy axis coincides with the easy axis of a pure magnetocrystalline anisotropy, and above 170 K rotates in the (001) plane towards $[\bar{1}10]$ (*Bowden et al.*, 2006, *Mougin et al.*, 2000). At room temperature, the direction of the moments is located at an angle of 30° out of the film plane. The strain parameters used in the simulations are derived from a single-ion point charge model (*Bowden et al.*, 2006) in qualitative agreement with *Mougin et al.* (2000), as explained in subsection 3.3.6. In figure 6.7 on page 76, the overall anisotropy shapes are depicted for 200 K (a) and 350 K (b). The magnetocrystalline anisotropy contributions fade comparably slowly for Dy (compared to other rare earth materials) with rising temperature (*Atzmony and Dariel*, 1976), and the cubic shape is pronounced for both temperatures. However, for 350 K, the cubic symmetry is notably distorted towards the z direction, favouring directions in the film plane. Figure 6.6 on the previous page shows the calculated values of the anisotropy energy barrier in z direction separating the easy axes, indicating a rapid decay of the barrier with rising temperatures.

Compound	Temperature	Cubic anisotropy constants			Strain term
	T [K]	K_1 [K]	K_2 [K]	K_3 [K]	d_{xy} [K]
$DyFe_2$	200	3.55e1	-1.00e1	3.16e0	8.75e0
	350	6.27e0	-1.00e0	9.31e-2	4.68e0
$ErFe_2$	100	-3.00e1	-4.50e1	4.50e0	-4.95e0
	200	-4.50e0	-2.50e0	6.20e-2	-2.81e0
	350	-4.84e-1	-1.29e-1	0.0	-1.13

Table 6.2: Anisotropy constants for different materials and different temperatures (*Bowden*, 2005, *Mougin et al.*, 2000). The first-order strain term d_{xy}, occasionally used instead of $\tilde{K}_2'$, is $d_{\mathrm{xy}} = \frac{1}{2}\sqrt{\frac{2\pi}{15}}\tilde{K}_2'$. Second-order strain terms are ignored.

The anisotropy constants K_1 to K_3 as well as the strain term d_{xy} used in the simulations are stated in table 6.2. The strain term cannot be plugged into OOMMF directly and has to be expressed by two uniaxial anisotropies according to eq. (3.89).

6.5 Results and discussion

Hysteresis loops have been computed for various temperatures T. The resulting switching patterns can be divided into a low-temperature regime for $T \leq 300$ K, and a high-temperature regime for $T > 300$ K. Results for each regime are depicted in figure 6.8 on page 77, comprising of net hysteresis loops (upper row) and compound-specific hysteresis loops (lower row). Starting off with high applied field and almost saturated magnetisation, the net hysteresis loop for 200 K (a) shows an accelerated decline of the magnetisation, with a negative coercivity of 0.65 T. At $B_{\mathrm{app}} \approx -1$ T, the magnetisation curve turns almost flat. These are the characteristics of an exchange spring system: with decreasing applied field, the magnetically soft layers unwind until the system reaches an ordered ferrimagnetic state (transition from figure 5.5(b) to 5.5(a)). For $B_{\mathrm{app}} \leq -11$ T, the magnetisation drops to almost negative saturation when the hard layers irreversibly switch into the direction of the field. This is underlined by the compound specific hysteresis loop (c), showing the soft YFe_2 magnetisation $\mathbf{M}_{\mathrm{YFe2}}$ forming an exchange spring first at a small positive field, and the hard $DyFe_2$ magnetisation $\mathbf{M}_{\mathrm{DyFe2}}$ switching subsequently at a high reversed B_{app}.

For 350 K, the appearance of the hysteresis loop has changed drastically: the net hysteresis loop (b) shows a first irreversible step at $B_{\mathrm{app}} \approx +5$ T ($\Delta M \approx 0.7 \times 10^5$ A/m). Coercivity is positive (0.65 T), accompanied by a second irreversible step of $\Delta M \approx 5 \times 10^5$ A/m. A third irreversible step is at -7.6 T, with a similar appearance as the first step. The compound-specific hysteresis loop (d) gives further insight: it is the magnetically hard $DyFe_2$ layer to switch first into a direction opposing

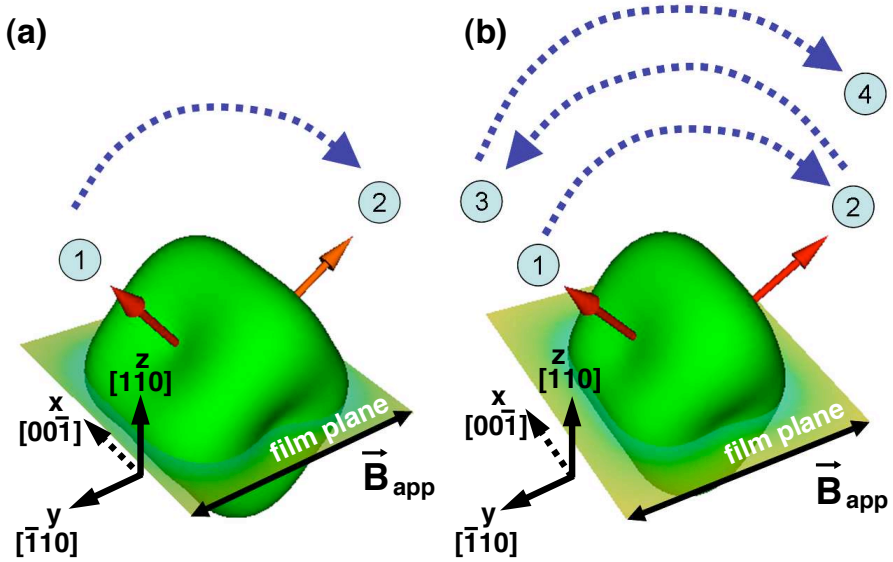

Figure 6.7: Normalised anisotropy energy surface (green) and average net magnetisation directions (red) for the $DyFe_2$ layers for 200 K (a) and 350 K (b). The dotted lines mark the irreversible switchings under a varied applied field. The spin states of the $DyFe_2$ layers are indicated by the circled numbers and can be looked up in figure 6.8 on the following page. The base directions x, y, z of the film coordinate system are depicted, showing the connection to the crystalline coordinate system $\langle 100 \rangle$.

$\boldsymbol{B}_{\text{app}}$. Both $\mathbf{M}_{\text{DyFe2}}$ and $\mathbf{M}_{\text{YFe2}}$ reverse at the second step, and $\mathbf{M}_{\text{DyFe2}}$ finally snaps towards $\boldsymbol{B}_{\text{app}}$ at the third step. A vanishing x magnetisation component for all simulations indicates that the reversal processes take place in the (001) plane.

For both 200 K and 350 K, the sequence of irreversible switchings is outlined by the average $\mathbf{M}_{\text{DyFe2}}$ in figure 6.7, represented by the arrows superimposed on the anisotropy surfaces. It rests in the energy minimum between the $[010]$ and $[\bar{1}10]$ direction or the equivalent zx mirrored energy minimum, and is slightly elongated from this position by the applied field and the exchange interaction of the $\mathbf{M}_{\text{YFe2}}$. For 200 K, the average $\mathbf{M}_{\text{DyFe2}}$ switches once, for 350 K three times.

The shape of the hysteresis loops for low and high temperatures obtained by micromagnetic simulations features all the characteristics of the experimental hysteresis loops (*Dumesnil et al.*, 2005, 2004). The quantitative differences can be accounted to the inability of the model to form complex magnetic structures in the xy plane and to the underestimation of demagnetising effects. However, the qualitative conformity of the hysteresis loops legitimates a further analysis of the simulation data for a better understanding of the interesting high-temperature switching behaviour.

In figure 6.9 on page 79, the high-temperature spin configurations are visualised with the resolution of the finite difference grid (1 nm), showing the transitions of

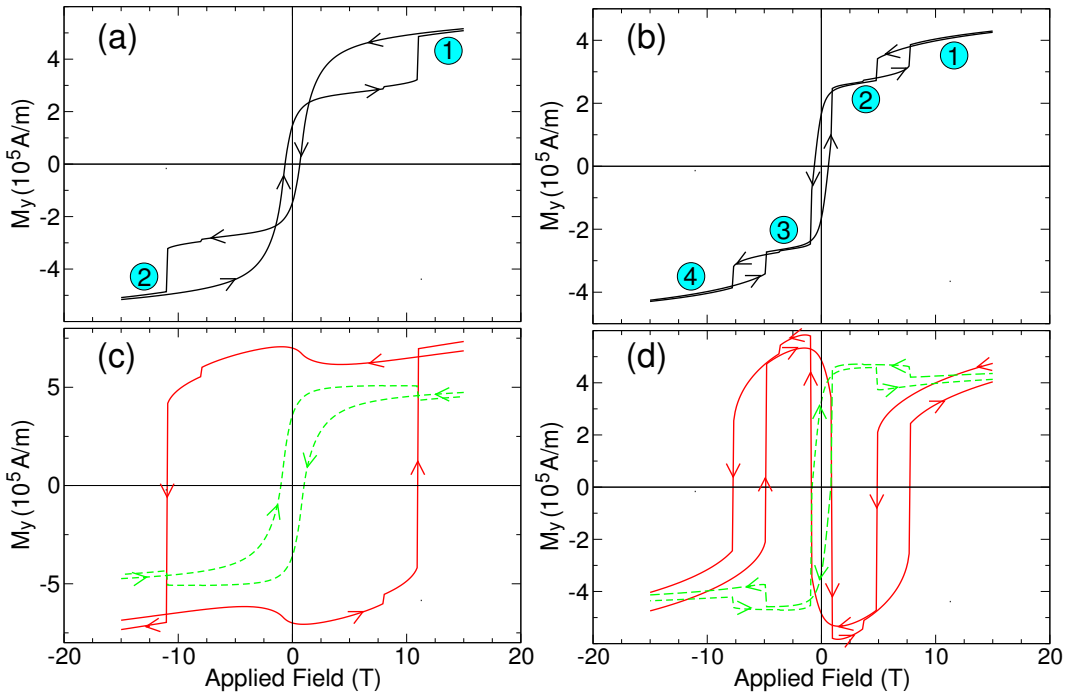

Figure 6.8: Hysteresis loops of the net (a,b) and compound-specific (c,d) magnetisation M_y as obtained by the simulations for 200 K (left) and 350 K (right). The solid (red) lines mark the y magnetisation of the $DyFe_2$ layers and the dashed (green) lines of the YFe_2 layers in (c,d). Circled numbers in (a, b) indicate the magnetisation states shown in figure 6.7 on the preceding page. For 350 K, spin configurations for states ① to ③ are depicted in figure 6.9 on page 79. These loops correspond to the experimental loops 6.5 on page 72. The lines are a guide to the eye.

spin states ① ② ③ of figure 6.8(b). Note that the magnetisation vectors do not rotate out of the yz plane, the plane of the graph. For high positive applied field (state ①), $\mathbf{M}_{\mathrm{YFe2}}$ is mostly aligned with the field (+y direction). $\mathbf{M}_{\mathrm{DyFe2}}$ is settled in the anisotropy dip close to $[010]$, towards $\boldsymbol{B}_{\mathrm{app}}$, but frustrating the exchange energy between the layers, giving a tight exchange spring. When the applied field is gradually reduced (①→②), the influence of exchange energy grows, turning $\mathbf{M}_{\mathrm{DyFe2}}$ towards a direction opposing $\mathbf{M}_{\mathrm{YFe2}}$ that is still mostly aligned with the field. Next, $\mathbf{M}_{\mathrm{DyFe2}}$ overcomes the anisotropy energy barrier and flips into the minimum close to $[100]$ (state ②): first irreversible step. In remanence state, $\mathbf{M}_{\mathrm{DyFe2}}$ rests in the latter anisotropy minimum, and the exchange energy keeps $\mathbf{M}_{\mathrm{YFe2}}$ in an opposing direction. Since the dominating $\mathbf{M}_{\mathrm{YFe2}}$ vectors still point in the direction of the applied field, the coercive field is positive. With $\boldsymbol{B}_{\mathrm{app}}$ reversing (②→③), $\mathbf{M}_{\mathrm{YFe2}}$ gradually rotates towards the -y direction. However, $\mathbf{M}_{\mathrm{DyFe2}}$ is still locked in the anisotropy dip, and exchange interaction keeps $\mathbf{M}_{\mathrm{YFe2}}$ from aligning with the new field direction. Consequently, a large interface wall is formed. The torque applied by the increasing reversed applied field acts on $\mathbf{M}_{\mathrm{YFe2}}$, which in turn drags $\mathbf{M}_{\mathrm{DyFe2}}$ back over the anisotropy energy barrier via the exchange interaction. $\mathbf{M}_{\mathrm{DyFe2}}$ returns to the anisotropy minimum close to $[010]$ and allows $\mathbf{M}_{\mathrm{YFe2}}$ to further rotate towards $\boldsymbol{B}_{\mathrm{app}}$. This is reflected in the second irreversible step to state ③, with a high magnetisation amplitude due to the synchronous reversal of both compounds. With further increasing negative applied field, another switching occurs, based on the same mechanism as the first switching (①→②).

The reason for the existence of the observed high temperature reversal process is apparent in the temperature dependence of the anisotropy barrier and the ratio of the net magnetisation of the two compounds (figure 6.6 on page 73): for high temperatures, the anisotropy barrier becomes sufficiently low to allow an isolated switching of $\mathbf{M}_{\mathrm{DyFe2}}$. Additionally, with the growing magnetic YFe_2 dominance for increasing temperatures, $\mathbf{M}_{\mathrm{YFe2}}$ stays closely aligned with $\boldsymbol{B}_{\mathrm{app}}$, and the exchange spring is formed by the winding of $\mathbf{M}_{\mathrm{DyFe2}}$.

6.6 Summary

Micromagnetic modelling of the $DyFe_2/YFe_2$ exchange spring system has proven its ability to reproduce hysteresis loops with characteristics matching those of experimental work. It enabled a thorough analysis of the high-temperature switching behaviour, explaining the unexpected magnetic reversal mechanism, with the magnetically hard $DyFe_2$ layers reversing before the magnetically soft YFe_2 layers. The strong thermal dependence of anisotropy plays a key role for the reversal processes, and the interplay with exchange and Zeeman energy is understood on a qualitative level.

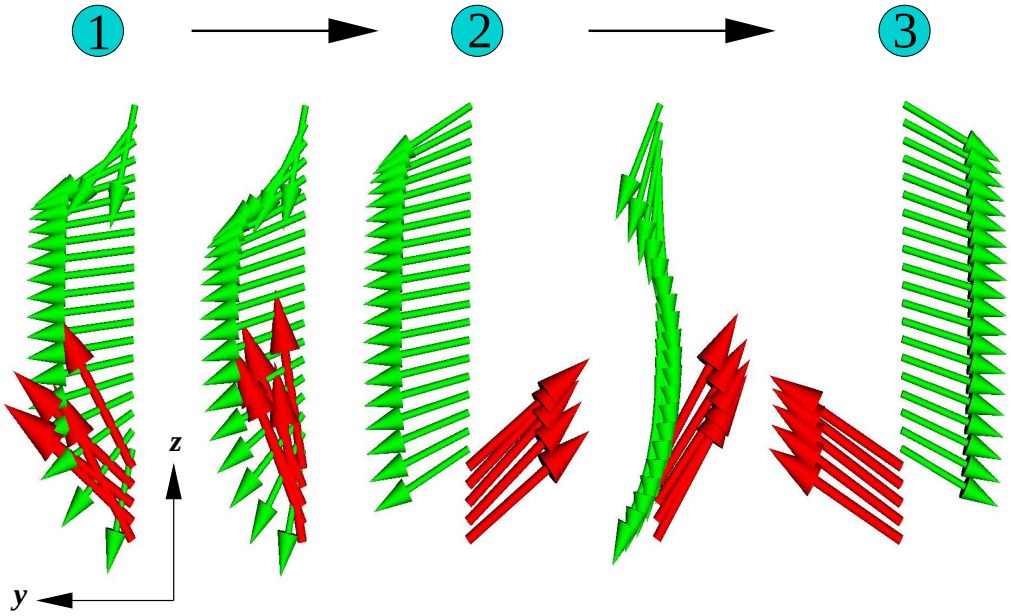

Figure 6.9: Spin configurations of an inward double-layer for 350 K for states ① to ③ as depicted in figure 6.8, and their transition states. The applied field points along the ±y direction. The $DyFe_2$ layer (red arrows) is located below the YFe_2 layer (green arrows), where the arrows indicate the net magnetisation vector per computational cell of 1 nm^3.

Chapter 7

Magnetic $ErFe_2/YFe_2$ exchange spring systems

The results of the work on $ErFe_2/YFe_2$ multilayers described in this chapter have been published in *Applied Physics Letters* (*Martin et al.*, 2006b). The experimental measurements were obtained by Kevin N. Martin of the School of Physics and Astronomy (University of Southampton).

7.1 Introduction

In this chapter, we use micromagnetic simulations to interpret the data obtained by magnetic measurements by Kevin N. Martin in Prof de Groot's team of a [110] [50Å$ErFe_2$/150ÅYFe_2]×20 Laves phase superlattice multilayer. The directions of easy magnetisation for the Er layers differ substantially from those of the Dy layers as described in chapter 6. We find three distinct switching patterns for different temperature regimes. For medium temperatures, we observe a spin flop mode where the average magnetisation in the $ErFe_2$ layers align in a nominally hard direction perpendicular to the field applied along [110]. The consideration of x, y, z components of the compound-specific average magnetisation sheds light on this unusual switching mode.

We start this chapter with a description of the basics of a vibrating sample magnetometer used for the magnetic measurements (section 7.2). Next, we outline the numerical model and the anisotropy characteristics of Er (section 7.3). In section 7.4, the results of the magnetic measurements and micromagnetic simulations are presented and discussed.

7.2 Vibrating sample magnetometer

The magnetic measurements were made by means of a vibrating sample magnetometer (VSM). The experimental technique of a VSM was invented in 1956 by

Figure 7.1: Vibrating sample magnetometer (VSM): the left photo of the complete set-up shows the actual VSM in the middle, with the transducer unit on the top and the cryostat vessel underneath. Adjacent are the helium containers required for the cooling of the cryostat. On the right photo, the vibration rod with the protruding sample holder can be seen on the top. On the bottom, the cryostat tail is visible that houses the sample holder during operation. The superconducting magnet has been removed.

Foner (1956, 1959). The basic idea is to mechanically vibrate a sample in a uniform magnetic field with a known frequency. Two pick-up coils are placed next to the sample. The movement of the magnetic sample creates a changing flux in the pick-up coils, and, by Faraday's law, an electrical signal is induced in the pick-up coils. The signal has the same frequency as the sample vibration, and its amplitude is proportional to the magnetic moment of the sample.

The VSM used here is an Aerosonic V.S.M. 3001 (figure 7.1). The sample is attached to a sample holder at the end of a carbon fibre rod in a transducer (*Martin*, 2007). The transducer generates vertical vibrations of approx. 60-100 Hz. The sample is inserted into the tail of an Oxford Instruments liquid helium cryostat, which is exposed to the magnetic field of a superconducting magnet of up to 12 T.

7.3 Method

As in the studies on $DyFe_2/YFe_2$ in chapter 6, OOMMF is used for the micromagnetic simulations. The direction of the applied field is different here ($\boldsymbol{B}_{\text{app}} \parallel [110]$), whereas parameters like cell size (1 nm^3), exchange length (3.4 nm), xy extension (1 cell), and antiferromagnetic coupling of Fe atoms (exchange coefficient $A = 1.46 \times 10^{-11}\ \text{J/m}$) are unchanged. Thermal effects are taken into account via

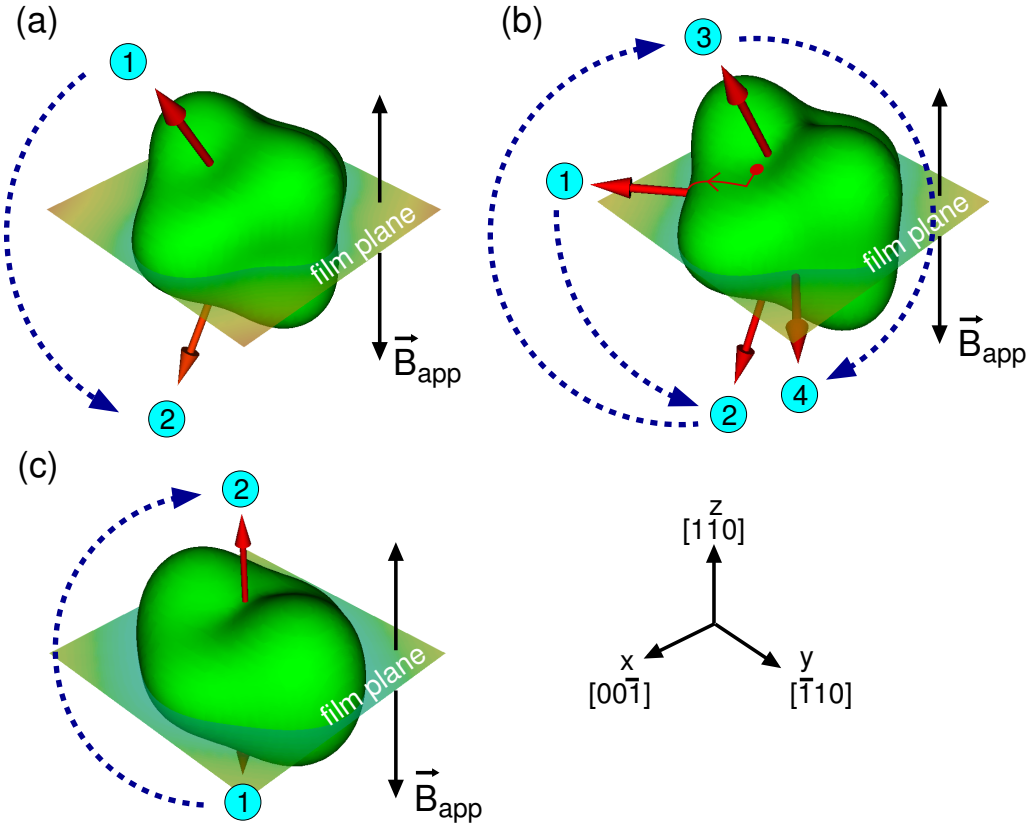

Figure 7.2: Normalised anisotropy energy surface (green) and average net magnetisation directions (red) for the $ErFe_2$ layers for 100 K (a), 200 K (b), and 350 K (c). Dotted lines and circled numbers are used in the same way as in figure 6.7 on page 76. The perspective has been rotated by $90°$ for better visibility. Three irreversible switchings occur in (b), in contrast to only one irreversible switching in (a) and (c). The trajectory in (b) marks the movement of the magnetisation for high reducing fields, before it settles in state ①.

temperature dependent magnetisation and anisotropy values as before (tables 6.1 and 6.2).

The anisotropy properties of Er are now discussed by means of figure 7.2. The cubic MC anisotropy of Er has easy axes along the body diagonals $\langle 111 \rangle$ of the crystal cell, in contrast to the Dy anisotropy favouring $\langle 001 \rangle$. This can be noticed by the opposite sign of the dominant K terms for the two materials in table 6.2 on page 75. The Er strain term prefers an out-of-film plane direction (negative sign of d_{xy}).

The strain term is almost negligible in comparison to the MC anisotropy for low temperatures. However, it decreases significantly slower than the MC anisotropy when temperatures rise. So the overall anisotropy is dominated by the MC contribution for low temperatures, whereas the strain contribution prevails for high temperatures, with a gradual transition for intermediate temperatures. In other words, at low temperatures we find eight equally deep minima of the anisotropy

energy in $\langle 111 \rangle$. When the temperature goes up and the strain term becomes important, the four easy axes pointing in out-of-film plane directions rotate towards $[110]$ and $[\bar{1}\bar{1}0]$, respectively; the four in-plane anisotropy minima gradually flatten and turn into saddle points. The characteristics can be followed in the plots of the overall anisotropy shape, figure 7.2 on the preceding page, when proceeding from 100 K (a) to 200 K (b), and finally to 350 K (c).

7.4 Results and discussion

Three different switching patterns are observed in the simulations, with a low-temperature (LT) regime for $T \leq 100$ K, a medium-temperature (MT) regime for 100 K $< T \leq 250$ K, and a high-temperature (HT) regime for $T > 250$ K. Figure 7.3 on the next page shows the hysteresis loops obtained by simulation (left) and experimental measurement (right). Temperatures of the corresponding experimental curves are lower, a phenomenon already discussed in section 6.5. However, for all three temperature regimes, there is a striking congruence of the hysteresis loops, obtained by experimental measurements and by simulations.

The LT hysteresis loop (a) suggests a typical exchange spring behaviour: starting from a large positive applied field, the magnetisation in the soft layers unwinds into negative coercivity; the magnetisation in the hard layers irreversibly switch at a negative applied field. The $ErFe_2$ magnetisation stays in close proximity to the easy axes of the anisotropy. These directions before and after the transition are outlined in figure 7.2a).

In the MT regime, the hysteresis loop (b) indicates a more complicated switching behaviour, showing three irreversible steps and positive coercivity. This interesting situation is analysed in detail later in this section.

Proceeding to higher temperatures, the MT triple switching scheme collapses into a simpler HT picture with one sharp transition and little hysteresis (c). This is well understood with our knowledge about the high-temperature anisotropy shape of Er, visualised in figure 7.2c): the only easy axes left are $[110]$ and $[\bar{1}\bar{1}0]$, and the $ErFe_2$ magnetisation switches between these two directions. The spin configuration stays in a ferrimagnetic state — the dominating magnetisation $\mathbf{M}_{\mathrm{YFe2}}$ of the YFe_2 compound aligned with the applied field, and the magnetisation $\mathbf{M}_{\mathrm{ErFe2}}$ of the $ErFe_2$ compound pointing the opposite way — up to very high fields $\boldsymbol{B}_{\mathrm{app}} > 10$ T, where $\mathbf{M}_{\mathrm{ErFe2}}$ starts winding towards the field.

The medium-temperature regime

In the MT regime, the spins do not stay in one plane, as it has been the case for the Dy multilayers. For this reason, we require all three spatial components of the magnetisation to obtain the full 3D picture of the reversal process (figure 7.4).

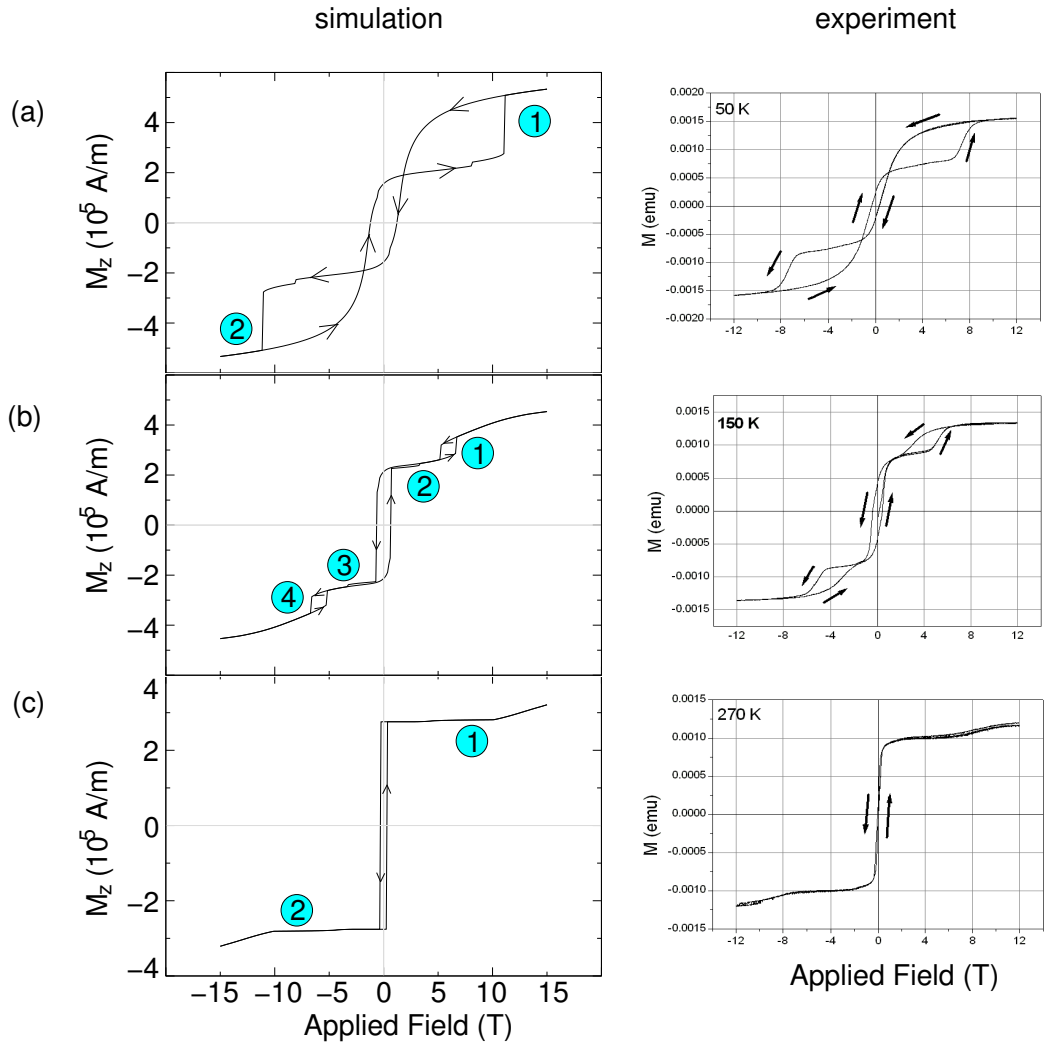

Figure 7.3: Hysteresis loops of the magnetisation in field direction [110], obtained by simulations (left) and measurements (right), for the low (a), medium (b), and high (c) temperature regime. The simulation temperatures were 100 K / 200 K / 350 K, compared to 50 K /150 K / 270 K in the experiments. Circled numbers correspond to the magnetisation states shown in figure 7.2 on page 82. The hysteresis loops of the individual magnetisation components for (b) are depicted in figure 7.4 on the following page.

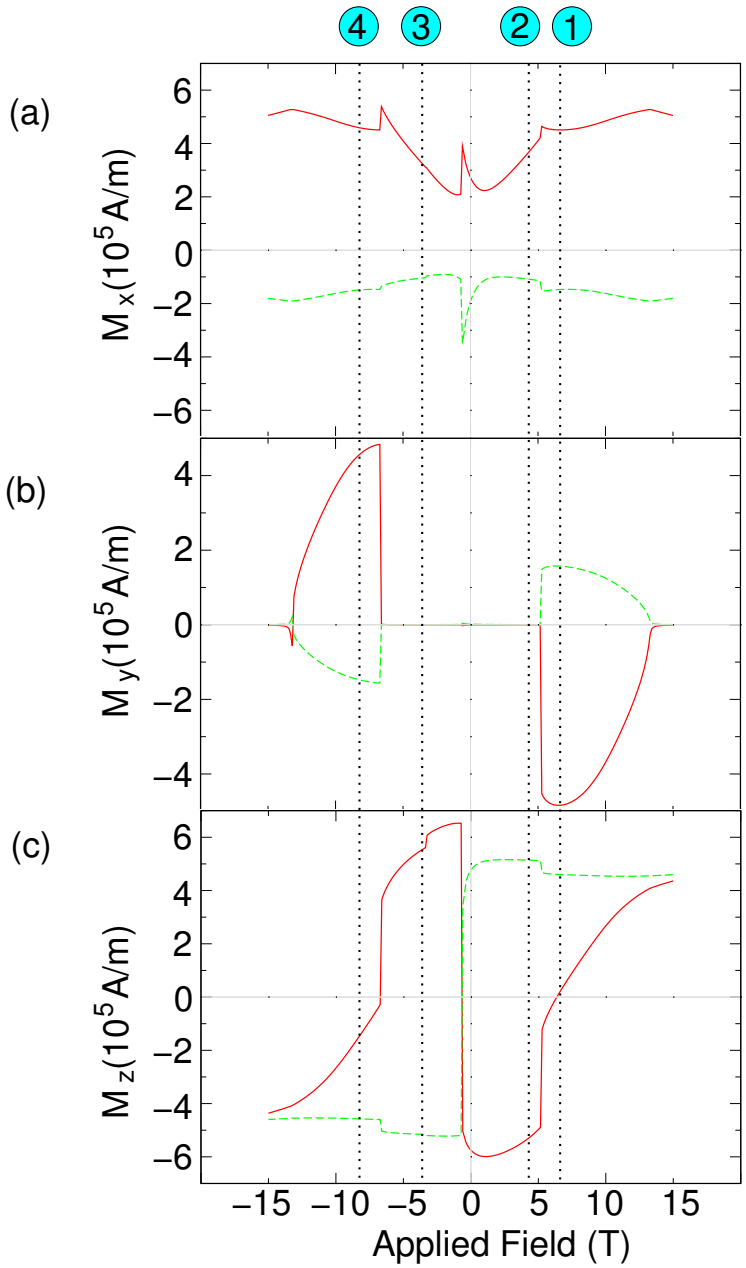

Figure 7.4: Medium-temperature regime, applied field acting along the z axis: graphs of the x (top), y (middle), z (bottom) component of the magnetisation, averaged per compound, as a result of the simulations. The solid line (red) represents the average magnetisation in the $ErFe_2$ compound, the dashed line (green) in the YFe_2 compound. For clarity reasons, the plots of the reverse field sweep are left out. The vertical dotted lines mark the applied fields corresponding to the respective spin states ① to ④, matching the spin state labels in figures 7.2(b) and 7.3(b).

The magnetisation graph of the z component 7.4c) and figure 6.8d) on page 77 are similar in appearance, suggesting that the hard layers switch earlier than the soft layers. The surprising part, however, is the y component of the magnetisation 7.4b). We follow the rotation of the Er magnetisation in figure 7.2b): very high fields (15 T) wind the Er magnetisation towards the applied field direction (the position is marked by a red dot on the green anisotropy surface). When gradually relaxing the applied field, the Er magnetisation first unwinds along a trajectory that lies in the xz plane. The trajectory is visualised by the red line starting at the red dot. Consistently, the y component of $\mathbf{M}_{\mathrm{ErFe2}}$ in 7.4b) is zero for applied fields of 15 T to 13.5 T. Then it becomes energetically favourable for the magnetisation to unwind sideways towards the $[1\bar{1}\bar{1}]$ direction in order to avoid the hard axis in $[00\bar{1}]$. So from 13.5 T on, the y component of the Er magnetisation decreases to negative values, reflecting the sideways movement. At 6.5 T, the Er magnetisation has reached its maximum y elongation in the configuration state ① of 7.2b). This is a spin flop state, visualised in figure 7.5 on the following page: the magnetisation in the $ErFe_2$ layers and in the adjoining parts of the YFe_2 layers point to directions perpendicular to the applied field. Nevertheless, the magnetisation in the interior of the YFe_2 layers, distant from the interfaces, bends towards the applied field, evident in a positive z component of YFe_2 in 7.4c).

When the applied field falls below 5.5 T, the pressure exerted by the dominating YFe_2 moments on the $ErFe_2$ moments via the antiferromagnetic coupling at the interfaces cannot be withstood by the now reduced Zeeman energy of the $ErFe_2$ moments and the Er anisotropy energy barrier. $ErFe_2$ switches into the $[\bar{1}\bar{1}\bar{1}]$ anisotropy minimum in the xz plane (state ② in 7.2b), where the y component of $\mathbf{M}_{\mathrm{ErFe2}}$ vanishes in 7.4b). After the applied field reversal, at -1 T, the magnetisation in all layers switches synchronously, with $\mathbf{M}_{\mathrm{ErFe2}}$ and $\mathbf{M}_{\mathrm{YFe2}}$ staying in diametrical opposition: the moments in the YFe_2 layers follow the new applied field direction, once more driving the $ErFe_2$ moments into a direction opposing the applied field via exchange interaction. State ③ in 7.2c) for an applied field of -3.5 T is a snapshot of this configuration. Under a further reducing negative field, the magnetisation in the $ErFe_2$ layers snaps into the spin flop state ④ at -6.5 T. Then it winds towards the applied field direction, first rotating into the xz plane, and then in the xz plane towards $[\bar{1}\bar{1}0]$.

A prerequisite for the interesting spin flop state is the existence of an anisotropy minimum $\langle 1\bar{1}\bar{1}\rangle$, halfway between the x and -y direction, to accommodate the $ErFe_2$ magnetisation. Due to the strain term and the changing topology of the anisotropy, both dependent on the temperature, this minimum disappears for temperatures exceeding 250 K. On the other hand, the anisotropy must not be overly strong to allow $\mathbf{M}_{\mathrm{ErFe2}}$ to slip into the spin flop direction without any blockage. The bottom line is that the spin flop state can only occur for medium temperatures.

Another factor for the occurrence of the spin flop state is the thickness of the

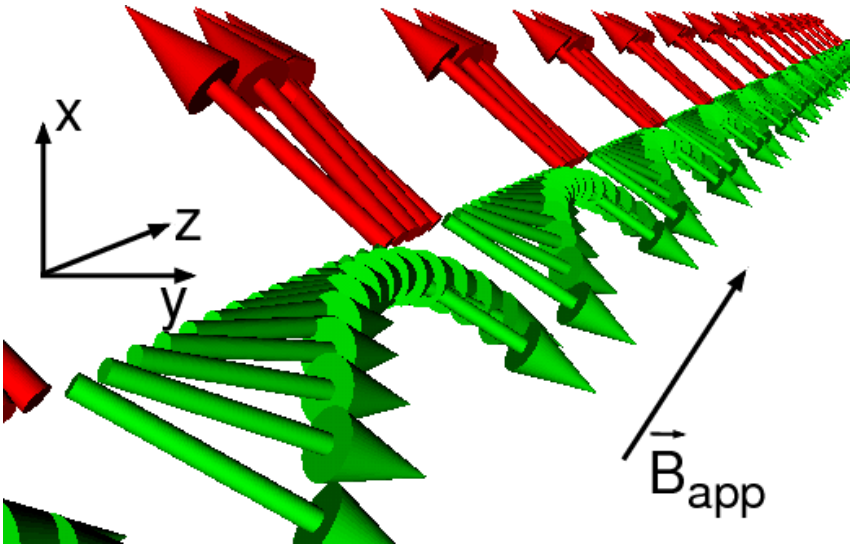

Figure 7.5: Medium-temperature regime: three-dimensional magnetic configuration in the $ErFe_2$ (upper left, red arrows), and YFe_2 (lower right, green arrows) layers for the spin flop state ① in figures 7.2b) and 7.4, for an applied field of 6.5 T. Directions of the film plane coordinate system and the applied field direction $\boldsymbol{B}_{\text{app}}$ are indicated.

composite layers which determines the ratio of YFe_2 moments in proximity to the interface to YFe_2 moments in the interior of the layer. This has not been investigated yet.

7.5 Summary

The simulation results explain the observed spin switchings and predict the existence of a quasi spin flop state. Future work — both on $DyFe_2/YFe_2$ and $ErFe_2/YFe_2$ models — will focus on an improved quantitative comprehension of the interacting parameters, by means of three-dimensional modelling and by varying the layer geometry. The success of the simulations so far allows us to proceed to systems with intertwined $DyFe_2/YFe_2$ and $ErFe_2/YFe_2$ multilayers with two hard magnetic materials and competing anisotropies.

Chapter 8

Magnetic $ErFe_2/YFe_2/DyFe_2/YFe_2$ exchange spring systems

The work on $ErFe_2/YFe_2/DyFe_2/YFe_2$ exchange spring simulations described in this chapter has been submitted to *Physical Review B* (*Zimmermann et al.*, 2007). The experimental measurements were obtained by Kevin N. Martin of the School of Physics and Astronomy (University of Southampton), using samples manufactured by Dr Roger C. C. Ward of Clarendon Laboratory (University of Oxford).

8.1 Introduction

In this chapter, we investigate the magnetisation reversal processes of exchange spring systems with two different magnetically hard materials for varied thicknesses of the soft layers. Exemplarily, we focus on antiferromagnetically coupled [10nm $ErFe_2/n$ YFe_2/4nm $DyFe_2/n$ YFe_2] exchange spring multilayers, harvesting on the previous studies of the individual $DyFe_2/YFe_2$ (chapter 6) and $ErFe_2/YFe_2$ (chapter 7) systems. These Laves phase superlattices can be epitaxially grown in a well-controlled and reproducible way, facilitating the production of samples with varied layer thicknesses n, but otherwise epitaxially identical. The range of n from 2 nm to 40 nm corresponds to the typical length scales of exchange spring structures. The two RE compounds, $ErFe_2$ and $DyFe_2$, are among the materials with the highest magnetic anisotropies. The YFe_2 compound bears negligible magnetic anisotropy. The thickness of the $ErFe_2$ layers (10 nm) is set larger than that of the $DyFe_2$ (4 nm) layers to approximately compensate for the higher effective magnetisation of $DyFe_2$ described later, giving the $ErFe_2$ and $DyFe_2$ compounds comparable magnetic weight.

The Fe in either of the YFe_2, $ErFe_2$, $DyFe_2$ compounds is responsible for the exchange interaction within and across the layers, and the exchange stiffness is widely homogeneous throughout the sample. Consequently, the ratio of the layer thicknesses of hard and soft compounds represents a parameter which allows us to

tune the impact of the RE anisotropy on the magnetic switching states independent of intricacies imposed by the exchange interaction.

Another main aspect of the investigated system is the pre-strung magnetisation configuration of the soft YFe_2 compound: since the YFe_2 layers are sandwiched between two different magnetically hard layers $ErFe_2$ and $DyFe_2$ with differing anisotropy properties, a built-in domain wall is present in the intermediate YFe_2 layer even in the remanent state. For simpler systems with one hard compound as descibed in chapters 6 and 7, the magnetisation in the soft compound is completely relaxed in the remanence state.

In the following section 8.2, the numerical model (8.2.1) and the material parameters (8.2.2) used for the simulations are stated. In section 8.3, we present magnetisation measurements along the [110] direction of a sample with $n = 20$ nm for a set of temperatures T between 10 K and 300 K. They are compared to the results of micromagnetic simulations with OOMMF in section 8.4, and the observed switching modes with their respective spin configurations are explained on the basis of the simulation data in section 8.5. In section 8.6, the thickness layer n is varied: graphs of the direction cosines of the compound-specific magnetisations suggest a quantifiable definition of the switching modes (8.6.1). The switching modes are analysed and their regimes are mapped with regard to T and n (8.6.2). The boundaries of the regimes are understood by energy considerations.

8.2 Method

8.2.1 Numerical model

We use the OOMMF code for our simulations, with extensions for higher order anisotropy energy terms (*Computational Engineering and Design Group, University of Southampton*, 2004). For the time evolution, the Landau-Lifschitz-Gilbert equation is employed, determining quasi-static magnetisation configuration states by a damped precession of the magnetisation.

For the underlying numerical model, we assume a homogeneous magnetisation in the (110) film plane, allowing us to represent the system by a 1d chain of computational cells along $[110]$, according to the model used in chapters 6 and 7. The computational cell size of 1 nm^3 is sufficiently smaller than the exchange length of either compound material. The spins of the RE and Fe atoms couple to an effective magnetic moment $\boldsymbol{m}_{\text{eff}}$, as described in section 6.2: we draw on the ferrimagnetism of the $REFe_2$ materials and assume a rigid exchange coupling of the magnetic moments of the 8 RE and the 16 iron atoms inside a lattice cell (figure 8.1 on the next page). As the magnetic moments of Er and Dy outweigh that of Fe by at least a factor of 2, the effective moments of $ErFe_2$ and $DyFe_2$ oppose the moment of the atomic Fe.

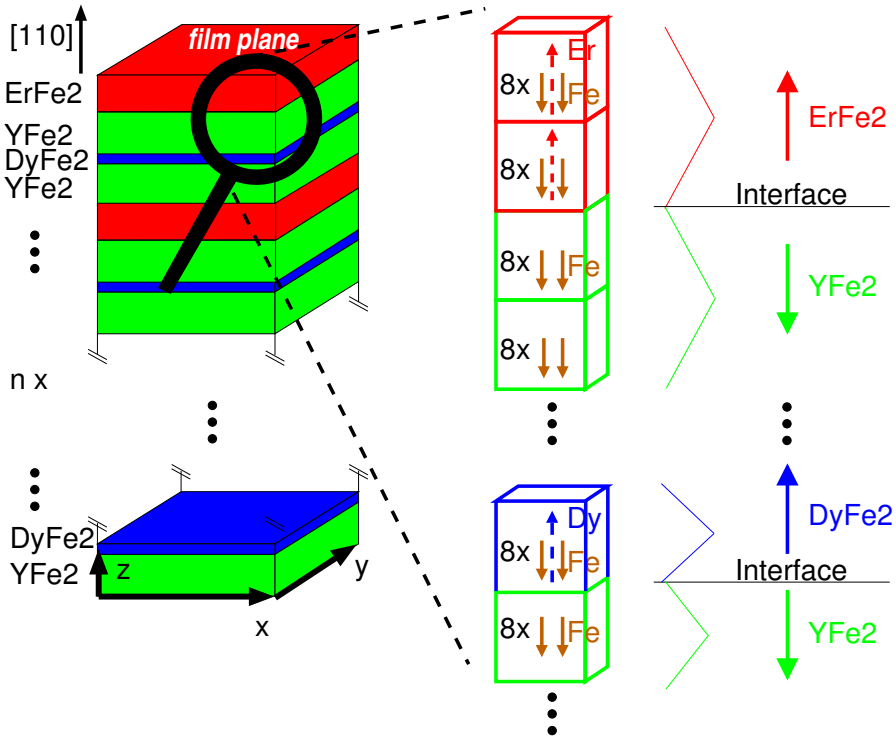

Figure 8.1: Sketch of the underlying numerical model, showing the layers of $ErFe_2/YFe_2/DyFe_2/YFe_2$ compounds (left), and the rigid coupling of the atomic moments to an effective magnetisation for each compound (right). The arrows representing the atomic moments reflect the relative antiferromagnetic alignment of RE and Fe inside a crystal cell and the relative ferromagnetic alignment of Fe across the cells, not the real magnetisation directions.

Across crystal cells, we only consider the ferromagnetic coupling of the Fe atoms, with a positive intra-layer exchange coupling A_{i} for all compounds, a negative across-layer exchange coupling $A_{\mathrm{a(RE\text{-}Y)}}$ between the effective $REFe_2$ and YFe_2 moments, and a positive across-layer exchange coupling $A_{\mathrm{a(RE\text{-}RE)}}$ between the effective $ErFe_2$ and $DyFe_2$ moments. Magnetostatic effects are taken into account in form of the approximation for the demagnetising energy density

$$\varepsilon_{\mathrm{d},i} = \frac{1}{2}\,\mu_0\,(\boldsymbol{M}_i \cdot \hat{\boldsymbol{e}}_\perp)^2 \tag{8.1}$$

for homogeneously magnetised thin film slabs i with a magnetisation $\boldsymbol{M}_i$ and an out-of-film plane unit vector $\hat{\boldsymbol{e}}_\perp$, as explained in subsection 3.4.4. In our model, each computational cell in the 1d chain represents one film slab, and $\hat{\boldsymbol{e}}_\perp$ is the [110] direction.

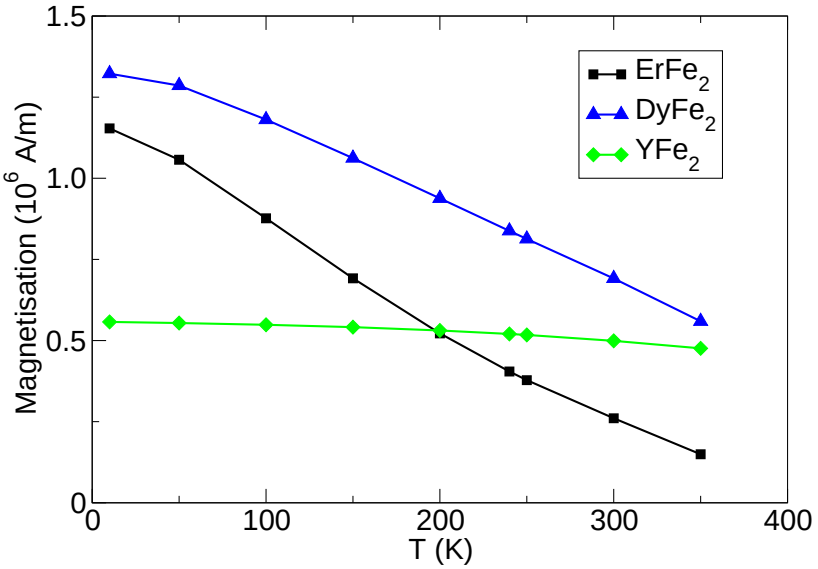

Figure 8.2: Effective magnetisations of $ErFe_2$ (black squares), $DyFe_2$ (blue triangles), and YFe_2 (green diamonds) as a function of temperature.

8.2.2 Material parameters

The exchange constants for the compound materials $A_{\text{a(RE-RE)}} = -A_{\text{a(RE-Y)}} = A_{\text{i}} = 1.46 \times 10^{-11}$ as stated in subsection 6.2.2 are used. The effective magnetisations of the compound materials consist of the atomic magnetic moments of Er, Dy, and Fe according to subsection 6.2.1, with values stated in appendix A.1. The result can be seen in figure 8.2: for low temperatures $\lesssim 200$ K, $DyFe_2$ and $ErFe_2$ magnetisations prevail, whereas for temperatures $\gtrsim 200$ K YFe_2 starts dominating over $ErFe_2$ and increasingly catches up with $DyFe_2$. For all temperatures considered, the magnetisation of $DyFe_2$ exceeds that of $ErFe_2$.

The orientation of the lattice cell with its basis vectors [100], [010], [001] in the lab system x,y,z for the crystal growth direction [110] is outlined in figure 6.2 on page 69. The RE magnetocrystalline (MC) anisotropy of the bulk is described by the phenomenological parameters K_1, K_2, K_3 of the cubic anisotropy energy density as defined in eq. (6.3). The K_1, K_2, K_3 values are taken from calculations extending the Callen-Callen model to second order (*Martin et al.*, 2006a), the results of which are given in appendix A.2.

Additionally, a shear strain ϵ_{xy} is present due to the [110] MBE growth direction of the films (*Mougin et al.*, 2000), incorporated in the strain energy density ε_{me} (eq. (3.86)). ε_{me} is approximated in terms of the strain coefficients $\tilde{K}_2'$ and $\tilde{K}_{242}''$; the values from *Bowden et al.* (2006) are listed in appendix A.3. The strain term generally attenuates slower with rising temperature than the MC contribution. Con-

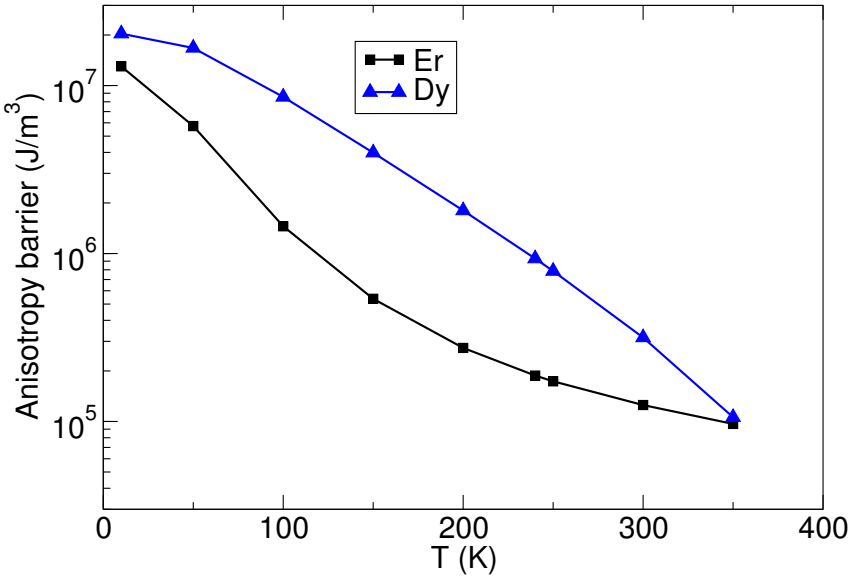

Figure 8.3: Anisotropy energy barriers (logarithmic scales) of Er (black squares) and Dy (blue triangles) as a function of temperature. The energy barriers are visualised in figure 8.4.

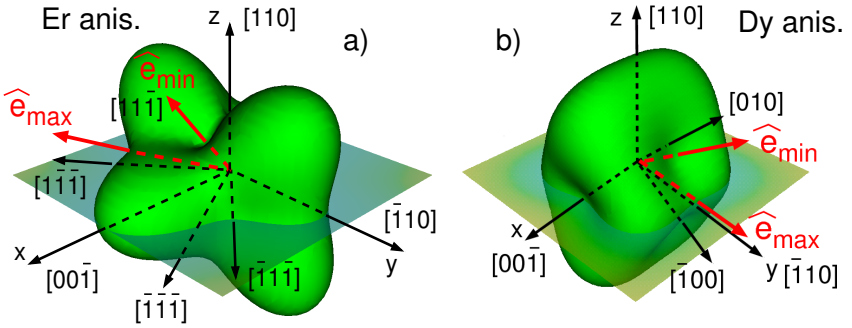

Figure 8.4: Graphical presentation of the energy barriers for Er (a) and Dy (b). Each energy barrier is the difference of the anisotropy energy densities with regard to a maximum direction ($\hat{e}_{max}$) and a minimum direction ($\hat{e}_{min}$).

sequently, the total anisotropy as a sum of MC anisotropy and strain term shows temperature dependent characteristics (anisotropy directions as shown in figure 6.2 on page 69 and figure 8.4 on the previous page): $ErFe_2$ has easy magnetisation directions along the body diagonals of the lattice cell $\langle 11\bar{1} \rangle$ for low temperatures (i.e. 10 K). For increasing temperatures, the out-of-plane easy axes move from $[111]$ and $[11\bar{1}]$ towards $[110]$, the in-plane easy axes from $[1\bar{1}\bar{1}]$ and $[\bar{1}1\bar{1}]$ towards $[00\bar{1}]$ due to the strain term becoming more pronounced. For $DyFe_2$, the out-of-plane easy axes gradually rotate from $[\bar{1}00]$ and $[010]$ towards $[\bar{1}10]$ under rising temperature, and the $[00\bar{1}]$ easy axis eventually turns into a hard axis. *Zhukov et al.* (2004) measured an out-of-film plane angle of the easy directions $\theta \approx 14^\circ$ at 290 K. For our simulations, we adjust the $DyFe_2$ anisotropy parameters to take this into account: the $\tilde{K}_2'$ of *Bowden et al.* (2006) seems to underestimate the strain. This is apparent in an excessive θ determined by simulations of pure $DyFe_2$ where the applied field in [110] is gradually relaxed, and the magnetisation settles in the out-of-plane anisotropy minimum. After multiplying the $\tilde{K}_2'$ values with a factor of 2.5 we are able to replicate the findings of *Zhukov et al.* (2004)

We analytically determine the relevant anisotropy energy barriers for Er and Dy (figure 8.3 on the preceding page). Both barriers fade with rising temperature, facilitating switching processes.

The magnetisation characteristics of specific $DyFe_2/YFe_2$ and $ErFe_2/YFe_2$ systems have been described earlier. We will now focus on generalised [10nm $ErFe_2/n$ YFe_2/4nm $DyFe_2/n$ YFe_2] systems with different n, and start with $n = 20$ nm.

8.3 Experimental data: the $n = 20nm$ sample

A [10nm $ErFe_2/n$ YFe_2/4nm $DyFe_2/n$ YFe_2] superlattice with $n = 20$ nm is grown by molecular beam epitaxy (MBE). The $[110]$ growth direction of the Laves phase materials is in accordance with the strain term contribution to the anisotropy of the numerical model (eq. (3.86)). The samples are magnetically characterised along the $[110]$ direction by the use of a vibrating sample magnetometer VSM (section 7.2).

The resulting hysteresis loops for the total magnetisation are presented in the left column of figure 8.5 on the next page for four temperatures (a to d). For 10 K (8.5a) the loop features a typical exchange spring appearance insofar as the magnetisation smoothly slopes when the applied field relaxes from a maximum positive value — the unwinding of the soft YFe_2 magnetisation into a ferrimagnetic alignment. Whereas an exchange spring system with one magnetically hard material shows one step-down indicating the switching of the hard compound, here we see one larger drop at an applied field B_{S1} of -6 T, and a smaller one at an applied field B_{S2} of -8 T. It seems obvious to identify the former with the switching of the $ErFe_2$ compound into the applied field direction, the latter with that of $DyFe_2$: in the case

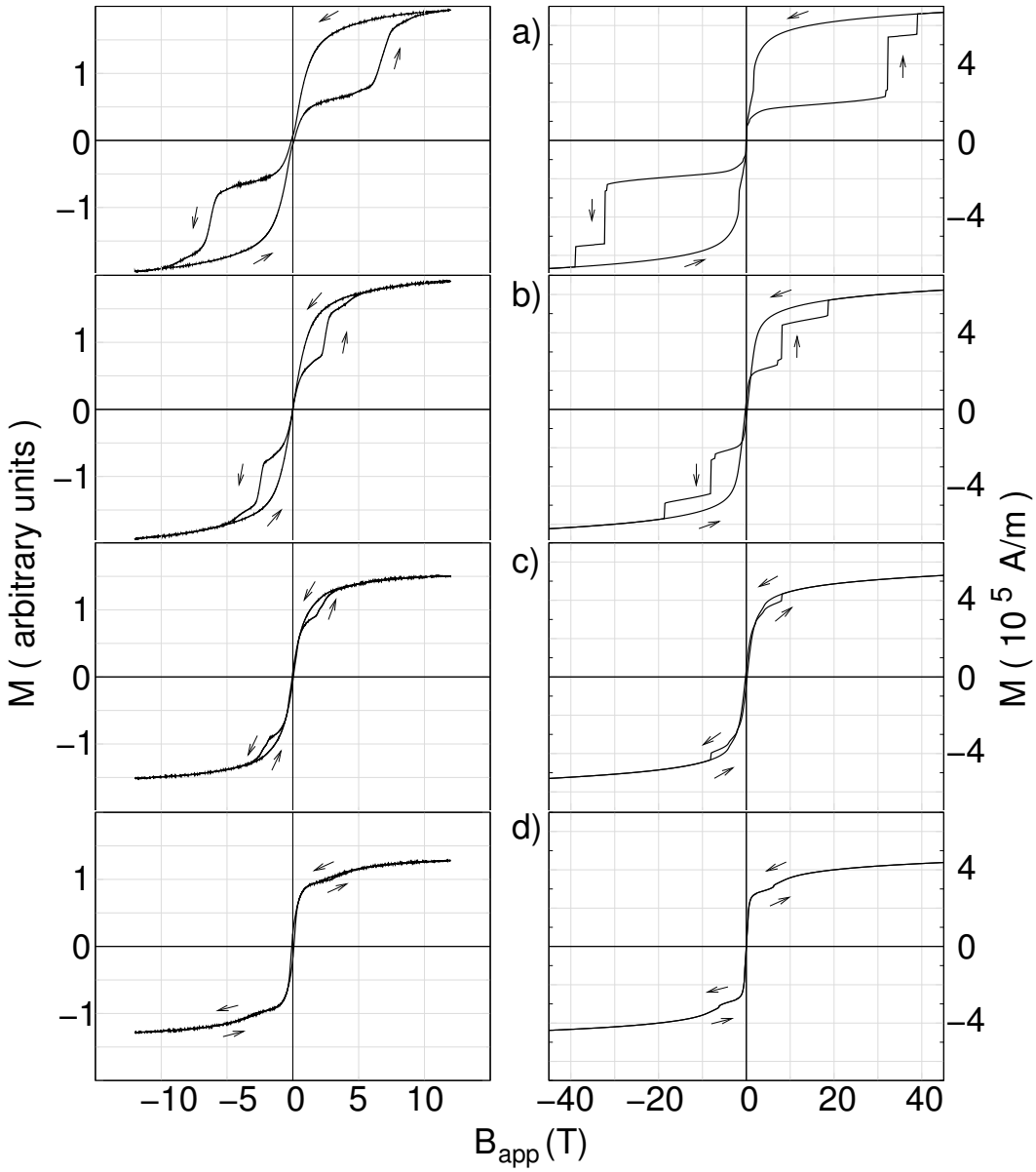

Figure 8.5: Hysteresis loops as a result of measurements (left column) and simulations (right column) for different temperatures with a separation layer thickness 20 nm. The temperatures are 10 K (exp.) and 10 K (sim.) (a), 95 K (exp.) and 100 K (sim.) (b), 200 K (exp.) and 200 K (sim.) (c), 290 K (exp.) and 300 K (sim.) (d). The arrows indicate the sweep direction of the applied field.

of $DyFe_2$, higher anisotropy energy barriers have to be overcome before the switching takes place (figure 8.3). Furthermore, the different step amplitudes correspond to the ratio of the RE layer thicknesses (4 nm:10 nm).

For 95 K (8.5b), the characteristics of the hysteresis loop are widely unchanged, but the switching fields are substantially decreased, with B_{S1} around -2.5 T and B_{S2} around -4 T. In the hysteresis loop for 200 K (8.5c), the large drop attributed to the $ErFe_2$ switching has disappeared, with only the small $DyFe_2$ switching step left at B_{S2} of -2 T. At 295 K (8.5d), the hysteresis loop presents a small kink at a field B_K of approximately -3 T. Otherwise, the curve is smooth.

For all four temperatures, the coercive field is basically zero. This leaves us with three different hysteresis loop appearances of the $n = 20$ sample: one for 10 K and 95 K, another for 200 K, and a third for 290 K.

8.4 Modelling of hysteresis loops

In order to gain further insight into the detailed spin configurations, we run micromagnetic simulations based on the numerical model outlined in section 8.2. The applied field is swept along the $[110]$ axis perpendicular to the film plane from +60 T to -60 T, and back to +60 T with a resolution of 160 mT. Hysteresis loops are generated in order to compare them to the measurements and to confirm the numerical model. The resulting hysteresis loops (10 K, 100 K, 200 K, 300 K) are placed next to the experimental loops with the same or very similar temperatures on the right column of figure 8.5 on the preceding page. For all four temperatures, the shapes of the magnetisation curves of the simulations bear a striking resemblance to those of the measurements, featuring all the characteristics described in section 8.3 on page 93.

The modelled switching fields, however, are too large by a factor of 2 to 5. This is a consequence of the 1d model that is unable to cope with nucleation processes – a fact known as Brown's paradox (*Aharoni*, 1962, *Brown*, 1963, *Hubert and Schäfer*, 1998, 2000). In spite of this inherent problem, the qualitative agreement of the simulation and measurement loops for $n = 20$ nm is formidable and justifies further interpretation of the numerical data. Similar results are found for $n = 10$ nm.

The reversibility of selected sections of the hysteresis loop for a temperature of 100 K is elucidated in figure 8.6 on the following page in the case of the simulations: the applied field is swept to a specific target value just beyond the section of interest, and the field sweep direction is reversed. Irreversibilities are then recognisable when the curves for the two different sweep directions are not congruent.

The exchange spring unwinding (figure 8.6a) turns out to be reversible, the two steps for negative applied fields irreversible (figure 8.6bc), underpinning the interpretation of the experimental hysteresis loops. The two hard compounds $ErFe_2$ and

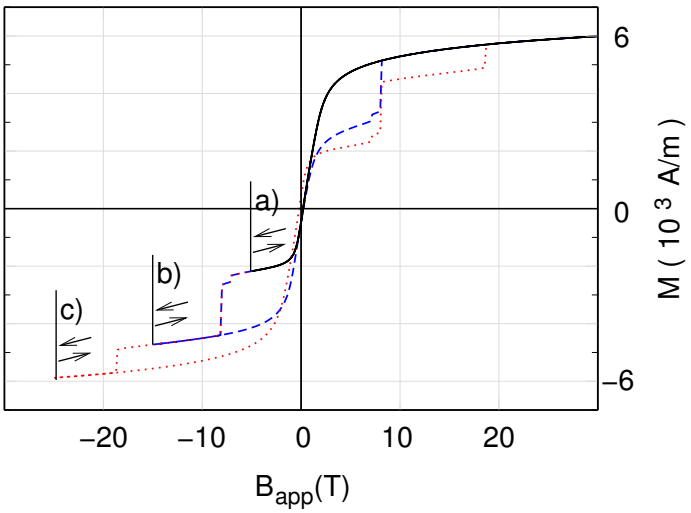

Figure 8.6: Overall hysteresis loop for an YFe_2 layer thickness of 20 nm at T=100 K for different applied field sweeps. The applied field is varied from +30 T to -5 T (solid black line, a), or to -15 T (dashed blue line, b), or to -25 T (red dotted line, c), then back to +30 T to check the reversibility of the corresponding hysteresis loop parts.

$DyFe_2$ switch independently of each other.

8.5 Switching modes

We now explain the different magnetic reorientation processes underlying the three appearances of the hysteresis loops. For this, we calculate the compound-specific magnetisations, which are the magnetisations of each of the $DyFe_2$, $ErFe_2$, YFe_2 compounds separately. Each numerical cell is represented by one magnetisation vector, and the numerical compound-specific magnetisation is determined by averaging the magnetisation vectors over all layers containing this compound.

The result is depicted in figure 8.7 on the next page. For each of the three overall hysteresis loop appearances of figure 8.5 on page 94, one representative is illustrated (100 K, 200 K, 300 K). Additionally, the compound-specific details for 350 K (8.7d) are given. The overall hysteresis loop for 350 K has the same appearance as that of 300 K (8.5d). Each of the four graphs shows the compound-specific magnetisation curves in the upper section. In the lower section, the Er and Dy anisotropy energies are plotted. To the right, the characteristic switching states for the specific $ErFe_2$ and $DyFe_2$ magnetisation are visualised as 3d vectors on top of the anisotropy energy surfaces of Er and Dy.

For 100 K (figure 8.7a), the compound-specific magnetisation loops confirm the interpretation given in subsection 8.3 suggesting individual switching of the RE compounds and the exchange spring unwinding of the soft YFe_2 compound. For positive applied fields ($\Rightarrow$ state ①), the RE moments are located in their respective

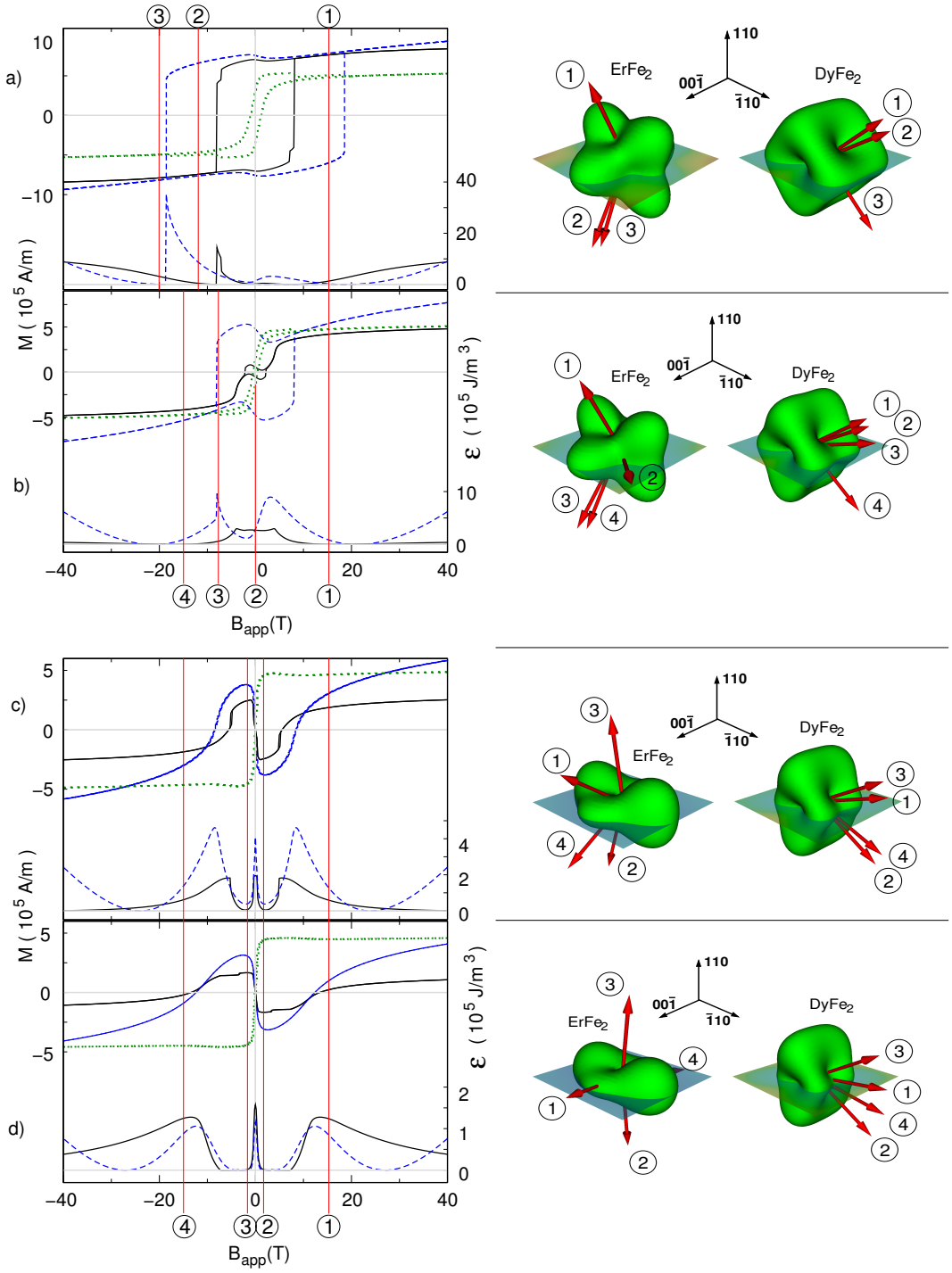

Figure 8.7: Compound-specific magnetisation curves and switching states for the temperatures 100 K (a), 200 K (b), 300 K (c), 350 K (d), and for an YFe_2 separation layer thickness 20 nm. In the upper section of each graph, the compound-specific magnetisation curves in the direction of the applied field [110] (solid black line for $ErFe_2$, dashed blue line for $DyFe_2$, dotted green line for YFe_2) are shown as obtained by simulations. In the lower section of the graphs, the corresponding anisotropy energy densities for the RE compounds (same colour and line coding) are depicted. In the insets, characteristic switching states are visualised ($ErFe_2$ on the left, $DyFe_2$ on the right): the magnetisation of a compound is specified by a red arrow on the green anisotropy surface. Each state is labelled with a number referring to an applied field that is marked by a numbered red horizontal line.

anisotropy energy dips — $ErFe_2$ at $[11\bar{1}]$, $DyFe_2$ at [010]. The YFe_2 moments, antiferromagnetically coupled to the RE moments, oppose the applied field direction $\boldsymbol{B}_{\text{app}}$ at the interfaces, and wind towards $\boldsymbol{B}_{\text{app}}$ in the interior. At state ①, the majority of the YFe_2 moments is aligned with the strong field, and its magnetisation is positive. When the field abates, the YFe_2 moments gradually unwind and their magnetisation reverses at positive applied fields. In the remanent state, the YFe_2 moments are antiferromagnetically aligned at the interfaces, pre-strung towards $[0\bar{1}0]$ at the $DyFe_2$ side, and $[\bar{1}\bar{1}1]$ at the $ErFe_2$ side, and uniformly swerve in between. Under a field rising in the reversed direction, the RE moments are gradually dragged out of their anisotropy dips, recognisable from the ascent in the anisotropy energy plots of the compounds. $ErFe_2$ is the first to switch at -8 T (⇒ state ②) , followed by $DyFe_2$ at -18 T (⇒ state ③). Each time, YFe_2 stays aligned with the applied field direction. Both switchings are accompanied by a sharp drop in the corresponding anisotropy energy. We define this the **independent switching mode**, referring to the independent RE switchings.

A new mode applies for 200 K (figure 8.7b). $ErFe_2$ now reverses via the spin flop direction $[\bar{1}1\bar{1}]$, embodied in the extra state ②. The $ErFe_2$ moments rotate into the spin flop state at a positive applied field of around 3 T. The process can be understood by magnetic energy considerations. At high applied fields, both the majority of YFe_2 moments and $ErFe_2$ moments are aligned with the field direction, with a domain wall around their mutual interface. Exchange coupling tries to push one compound into an antiferromagnetic alignment, but is outbalanced by the large Zeeman energies. When the applied field is sufficiently reduced, the YFe_2 moments at some point start to unwind. If beforehand the effect of the exchange interaction acting on $ErFe_2$ exceeds the Zeeman energy of $ErFe_2$ plus the Er anisotropy barrier, then the $ErFe_2$ moments rotate against the applied field direction into the spin flop state. Whether this condition is fulfilled, depends on the temperature: for rising temperatures the magnetic moment of $ErFe_2$ decays sharply (figure 8.2 on page 91), and with it the corresponding Zeeman energy. Additionally, the Er anisotropy energy barrier decreases exponentially as a function of increasing temperature (figure 8.3 on page 92). Both effects together cause the energy condition to be fulfilled above a critical temperature $T_{\text{crit,Er}}$; a spin flop state is achieved for the $ErFe_2$ moments. Analysis of the anisotropy energy function shows that there is a distinct minimum around $[\bar{1}1\bar{1}]$ for temperatures of around 200 K or lower, allowing the $ErFe_2$ moments to settle in this direction. When the field is increased in the opposite direction to -3 T, $ErFe_2$ is finally dragged out of the spin flop state into state ③ by Zeeman interaction. The $DyFe_2$ magnetisation stays in the [010] direction until it switches into state ④ at $[\bar{1}00]$ for -8 T. We define this the **$ErFe_2$ spin flop mode**, found in simpler $ErFe_2/YFe_2$ systems by *Martin et al.* (2006b), and described in chapter 7.

Under a further increase of the temperature to 300 K (figure 8.7c), the $DyFe_2$ (at

8 T) and $ErFe_2$ (at 5 T) moments reverse for positive fields ($\Rightarrow$ state ②). Whereas the $ErFe_2$ moments reside in the spin flop state $[\bar{1}1\bar{1}]$ for 200K, they now rotate further into $[\bar{1}\bar{1}\bar{1}]$, off the applied field direction. When the applied field is reversed, both the YFe_2 and the RE compounds switch ($\Rightarrow$ state ③): the $REFe_2$ moments keep opposing the applied field, the YFe_2 moments stay aligned with the applied field. Under a further decreasing applied field, the RE compounds switch a third time towards the applied field direction ($\Rightarrow$ state ④).

The reason why the $ErFe_2$ moments do not settle in the spin flop direction is that the anisotropy energy surface of Er has changed for 300K due to the strain term, and the $[\bar{1}1\bar{1}]$ direction is now a saddle point. The new triple switching of $DyFe_2$ can be explained by energy considerations similar to those for $ErFe_2$ at 200K, but unlike that case, the anisotropy barrier obstructing access to the spin flop direction ($[00\bar{1}]$ for $DyFe_2$) stays impregnable, and it is energetically favourable for $DyFe_2$ to reverse into $[\bar{1}00]$ over the more viable $[\bar{1}10]$ barrier. The critical temperature for the $DyFe_2$ triple switching $T_{\mathrm{crit,Dy}}$ is higher than $T_{\mathrm{crit,Er}}$ because of the generally stronger Dy anisotropy. The spin flop mode is observed for $T_{\mathrm{crit,Er}} < T < T_{\mathrm{crit,Dy}}$, and for $T > T_{\mathrm{crit,Dy}}$ the new mode applies. We call this the **YFe_2 dominated switching mode**. The name derives from the dominance of the YFe_2 moments and their respective Zeeman energy over the anisotropy energy barriers of the RE compounds, similar to the high temperature $DyFe_2/YFe_2$ behaviour observed by *Dumesnil et al.* (2004).

It has to be emphasised that the YFe_2 dominated switching mode is an extension of the $ErFe_2$ spin flop mode in a way that the $ErFe_2$ moments still transit the spin flop direction on their reversals.

Another example of the YFe_2 dominated switching mode is given for 350K, with displaced $ErFe_2$ spin directions: in the states ② and ③, the $ErFe_2$ moments are largely pointing to the opposite field directions $[\bar{1}\bar{1}0]$ and [110]; a ferrimagnetic spin configuration with the prevailing YFe_2. Furthermore, these directions are now energetically favourable with regard to the Er anisotropy, due to the increased importance of the strain term contribution.

8.6 YFe_2 thickness dependence

So far, we have observed three switching modes for a sample with $n = 20$ nm. The complex underlying reorientation processes were interpreted by micromagnetic modelling. We now take this further and run simulations with a varied n in order to establish a map of switching modes. The corresponding parameter space is composed of a temperature range from 10 K to 400 K with a step resolution of 10 K, and a separation layer thickness range $n \in \{2, 5, 7, 10, 12, 15, 17, 20, 22, 25, 27, 30, 32, 35, 37, 40\}$ nm. The total number of simulations carried out is therefore $40 \times 16 = 640$.

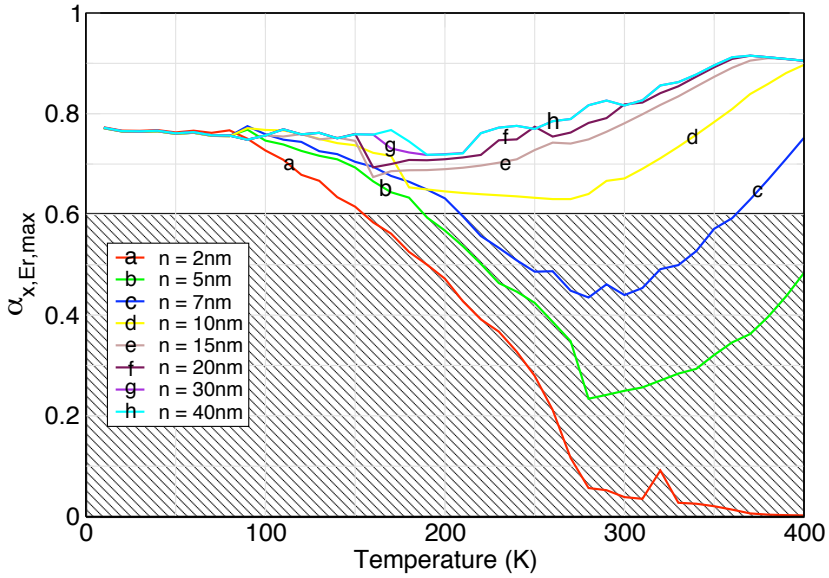

Figure 8.8: Maximum direction cosine $\alpha_{x,Er,max}$ in $[00\bar{1}]$ of the $ErFe_2$ magnetisation as a function of the temperature for different YFe_2 layer thicknesses. The YFe_2 layer thickness for each curve can be looked up in the legend. The hatched area indicates an $\alpha_{x,Er,max}$ smaller 0.6, signifying a distortion of the $ErFe_2$ magnetisation toward the $DyFe_2$ moments.

8.6.1 Identification of switching states

As we investigate magnetisation curves on a large scale, we require quantitative measures to efficiently identify magnetic switching states. The straightforward option is to analyse the compound-specific RE magnetisations, fixed by their direction cosines $\alpha_{x,RE}$, $\alpha_{y,RE}$, and $\alpha_{z,RE}$ with respect to the basis vectors $[00\bar{1}]$, $[\bar{1}10]$, and $[110]$ of the lab system. Per magnetisation curve, the maxima $\alpha_{x,RE,max}$ and $\alpha_{y,RE,max}$ of each of the compound-specific direction cosines are determined — a measure for the range of the magnetisation trajectories of the compounds. We focus on $\alpha_{x,RE,max}$ and $\alpha_{y,RE,max}$ as they provide suitable information about possible spin flop configurations. Plots of these observables as a function of T for a selection of n are given in figures 8.8 and 8.10 to 8.12.

In figure 8.8, $\alpha_{x,Er,max}$ is shown, where high values indicate orientation of the $ErFe_2$ magnetisation towards the $[00\bar{1}]$ direction, a hard axis of the Er anisotropy. The value at 10 K is around 0.8, independent of n. The huge anisotropy for very low temperatures is the sole crucial factor here to keep the $ErFe_2$ moment $\arccos(0.8) \approx 37°$ off from $[00\bar{1}]$.

For intermediate temperatures between 100 K and 250 K, $\alpha_{x,Er,max}$ generally drops, with a larger gradient for smaller n, and barely notable for n of 15 nm or more. As the anisotropy decreases with temperature, the exchange interaction of the RE compounds becomes more important, amplified for thin YFe_2 separation

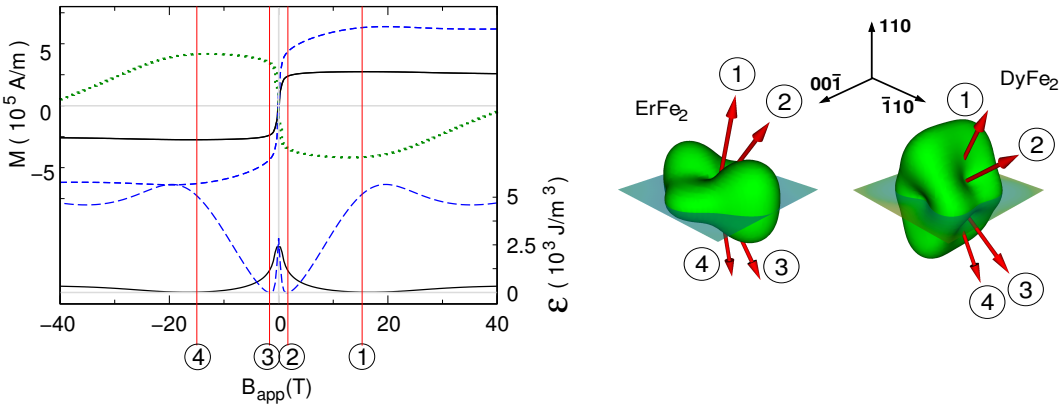

Figure 8.9: Coupled switching mode: compound-specific magnetisation curves and switching states for an YFe_2 separation layer thicknesses of 2 nm and a temperature of 290 K, The explanation of the graphs follows figure 8.7 on page 97.

layers: the $ErFe_2$ moments are attracted by the $DyFe_2$ moments toward the $(00\bar{1})$ plane perpendicular to the $[00\bar{1}]$ direction.

For $\alpha_{x,Er,max}$ smaller than $0.6 \approx \cos(57°)$, the $ErFe_2$ moments are distorted beyond the direction of its in-plane anisotropy minimum in $[\bar{1}1\bar{1}]$. We define this the **coupled switching mode**, as the $ErFe_2$ moments are now significantly coupled to the $DyFe_2$ moments. This mode is not observed in the $n = 20$ nm sample investigated in section 8.3 on page 93 due to the thick magnetic separation layer. An illustration is given in figure 8.9 for a sample with $n = 2$ nm: the exchange interaction between the RE compounds is strong enough to force the $ErFe_2$ moments to reverse from state ② to state ③ via the $[\bar{1}10]$ direction that is unfavourable with regard to the Er anisotropy.

The maximum direction cosines of samples with $n \geq 10$ nm converge to 0.9 for T reaching 400 K, and the $n = 5$ and 7 nm samples show a sharp increase towards this value (unlike the $n = 2$ nm sample). The reason for this behaviour is the dominance of YFe_2 under a diminishing Er anisotropy (discussed earlier in section 8.5) that causes $ErFe_2$ to increasingly unwind toward the unfavourable $[00\bar{1}]$ direction. YFe_2 starts prevailing at lower T when its layer gets thicker. For $n = 2$ nm, however, YFe_2 never prevails, and $\alpha_{x,Er,max}$ stays around zero up to 400 K.

Figure 8.10 on the following page pinpoints the spin flop states of the $ErFe_2$ compound by depicting the maximum direction cosine $\alpha_{y,Er,max}$ of the $ErFe_2$ magnetisation with respect to $[\bar{1}10]$. Low values of $\alpha_{y,Er,max}$ correlate with $ErFe_2$ moments staying in the $(\bar{1}10)$ plane during the complete magnetisation cycle. High values suggest a spin flop state for at least one point in the hysteresis loop. For temperatures below 100 K, the $ErFe_2$ moments of all samples clearly do not feature a spin flop state. When the temperature surpasses a critical value $T_{crit,Er}$, the $\alpha_{y,Er,max}$ sharply ascend to values of over 0.6, marked by the hatched area in the

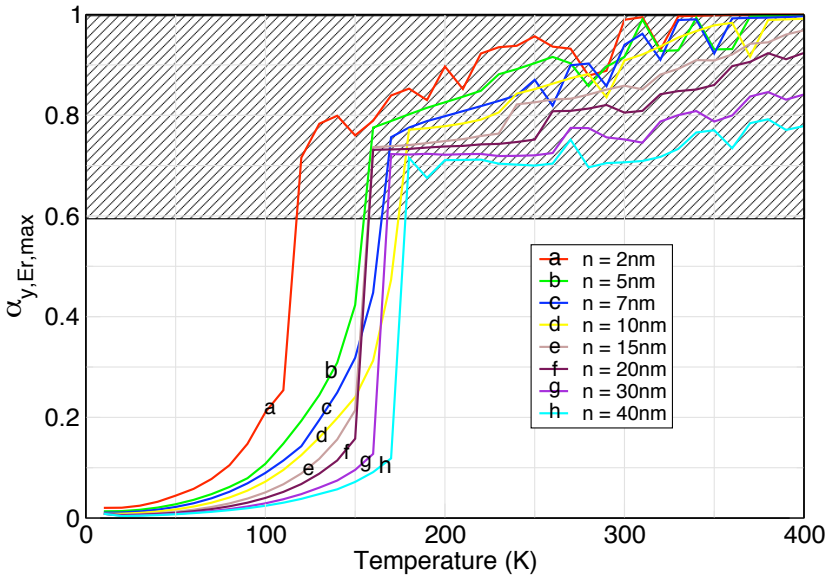

Figure 8.10: Maximum direction cosine $\alpha_{y,Er,max}$ in $[\bar{1}10]$ of the $ErFe_2$ magnetisation as a function of the temperature for different YFe_2 layer thicknesses. The YFe_2 layer thickness for each curve can be looked up in the legend. The hatched area indicates an $\alpha_{y,Er,max}$ larger 0.6, signifying a spin flop state of the $ErFe_2$ magnetisation.

graph, prevailing up to the maximum temperature of 400 K. This ledge confines the regime of the $ErFe_2$ spin flop mode at the low T side, whereas the boundary to the YFe_2 dominated switching mode at the high T side still has to be defined. Interestingly, $T_{crit,Er}$ is considerably smaller for $n = 2$ nm than for larger n values: the thin YFe_2 separation layer transmits the exchange interaction between the RE compounds. The $DyFe_2$ moments attract the $ErFe_2$ moments and assist $ErFe_2$ in switching into the $[\bar{1}1\bar{1}]$ spin flop state.

The occurrence of spin flop states for $DyFe_2$ follows from plots of the maximum direction cosine $\alpha_{x,Dy,max}$ of the $DyFe_2$ magnetisation with respect to $[00\bar{1}]$ in figure 8.11 on the next page. The $n = 2$ nm sample shows a solitary **$DyFe_2$ spin flop mode** for $T = 70$ K: the plot intrudes into the hatched area of magnetisation directions that are elongated from the $(00\bar{1})$ plane by more than $57°$. We presume this solitary data point is an artifact. It occurs for the lowest n value, 2 nm, where the different anisotropies of the RE compounds clash with little YFe_2 between them — a stress situation for the model and its assumption of rigid antiferromagnetic Fe-RE coupling. Apart from this isolated case, no $DyFe_2$ spin flop states are observed. The Dy anisotropy energy barrier blocks access to the in-plane spin flop minimum.

Figure 8.12 on the following page with its plots of the maximum direction cosine $\alpha_{y,Dy,max}$ of the $DyFe_2$ magnetisation with respect to $[\bar{1}10]$ suggests that the $DyFe_2$ moments cannot be forced out of their natural $(00\bar{1})$ plane by exchange coupling

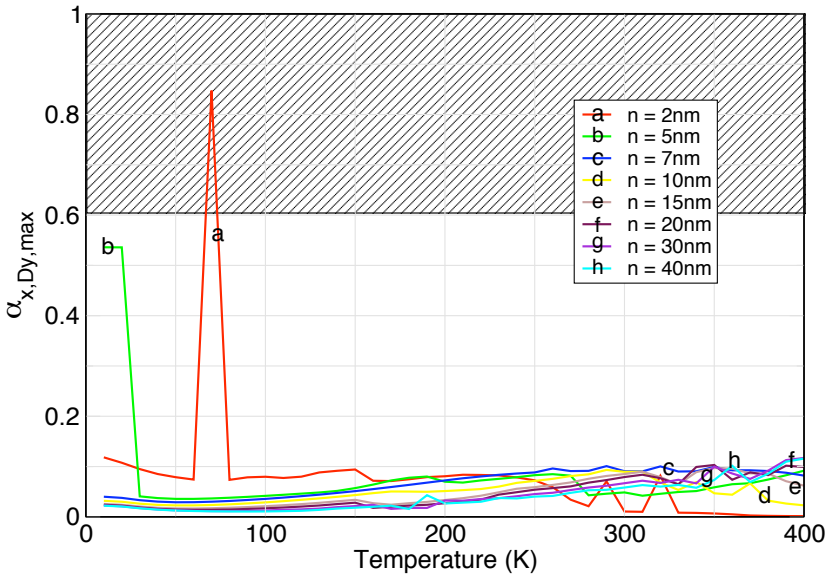

Figure 8.11: Maximum direction cosine $\alpha_{x,Dy,max}$ in $[00\bar{1}]$ of the $DyFe_2$ magnetisation as a function of the temperature for different YFe_2 layer thicknesses. The corresponding YFe_2 layer thickness for each curve can be looked up in the legend. The hatched area indicates an $\alpha_{x,Dy,max}$ larger 0.6, signifying a spin flop state of the $DyFe_2$ magnetisation.

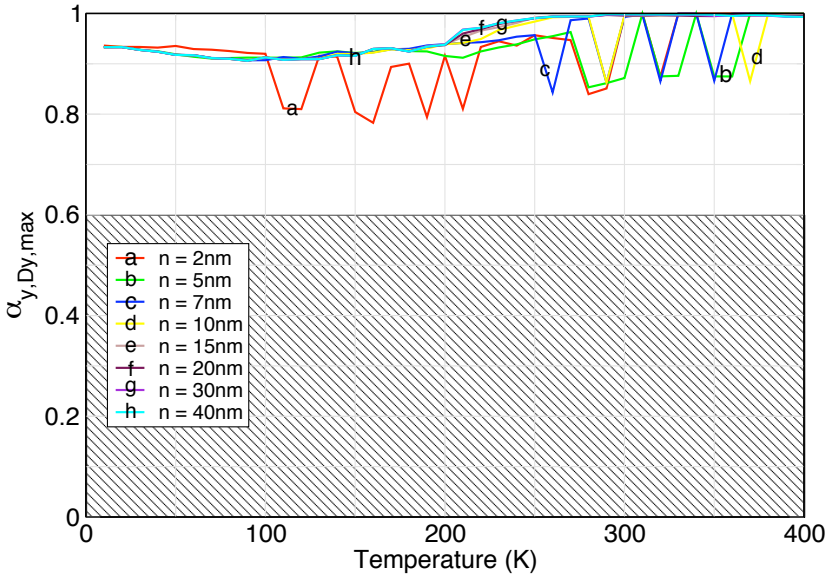

Figure 8.12: Maximum direction cosine $\alpha_{y,Dy,max}$ in $[\bar{1}10]$ of the $DyFe_2$ magnetisation as a function of the temperature for different YFe_2 layer thicknesses. The corresponding YFe_2 layer thickness for each curve can be looked up in the legend. The hatched area indicates an $\alpha_{y,Dy,max}$ smaller 0.6, signifying a distortion of the $DyFe_2$ magnetisation toward the $ErFe_2$ moments.

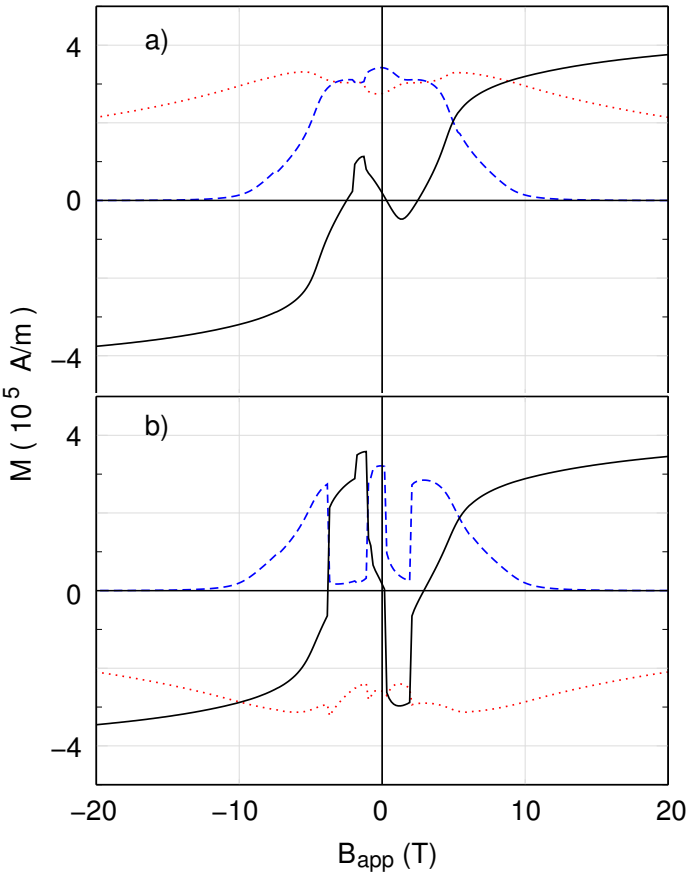

Figure 8.13: $ErFe_2$ magnetisation components in $[110]$ (solid black line), $[\bar{1}10]$ (dashed blue line), $[00\bar{1}]$ (dotted red line) direction for 220 K (a) and 230 K (b): the snapping of the $ErFe_2$ magnetisation in the case of 230 K is indicated by the drop of the $[\bar{1}10]$ component for about 1.5 T applied field.

with $ErFe_2$. No plot intrudes into the hatched area of the graph marking the range where the magnetisation resides in the vicinity of the $(\bar{1}10)$ plane throughout the hysteresis cycle. With relevant exchange interaction of the RE compounds, $DyFe_2$ takes control over $ErFe_2$ (and not vice versa).

Finally, an unambiguous criterion is required to identify the YFe_2 dominated switching mode. Following the definition of this mode in chapter 8.5, both RE compounds are required to switch against the applied field direction. This is easily recognised for $DyFe_2$ – a change of sign of the [110] magnetisation component for positive B_{app}. However, this condition is not sufficient in the case of $ErFe_2$. In the proximity of the in-plane spin flop state $[\bar{1}1\bar{1}]$, the [110] magnetisation component of $ErFe_2$ can change sign without switching. Figure 8.13 shows all three magnetisation components of the $ErFe_2$ compound for $T = 220$ K (a, $ErFe_2$ spin flop mode) and $T = 230$ K (b, YFe_2 dominated switching mode). While the [110] component changes sign at $B_{\text{app}} \approx 2.5$ T for both 220 and 230 K, the $[\bar{1}10]$ component drops

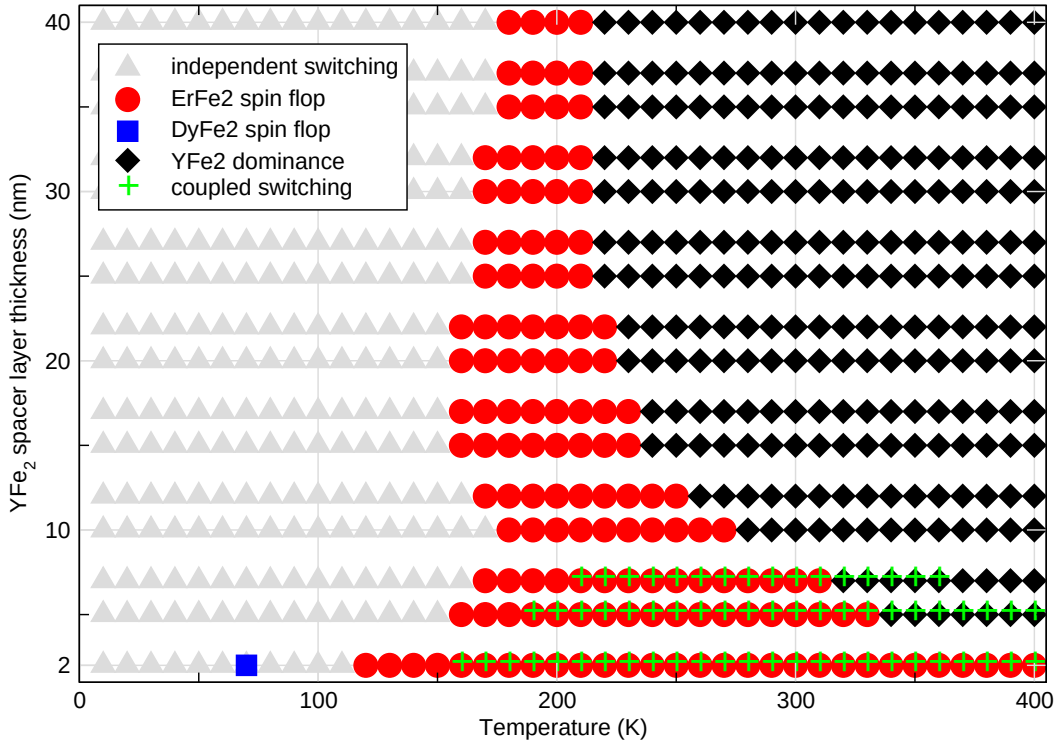

Figure 8.14: Switching modes for different temperatures and YFe_2 separation layer thicknesses as a result of simulations using the numerical model given in figure 8.1 on page 90. The grey triangles represent the independent switching mode, where the magnetisations of both RE compounds hysteretically switch into the direction of the applied field. The red circles indicate the $ErFe_2$ spin flop mode. The black diamonds signify the YFe_2 dominance mode with RE unwinding against the applied field direction. Superimposed green crosses refer to a distortion of the $ErFe_2$ moments toward the $DyFe_2$ switching plane $(00\bar{1})$, the coupled switching mode. The solitary $DyFe_2$ spin flop state is denoted by a blue square.

only for $T = 230$ K when the $ErFe_2$ moments snap into the $[\bar{1}\bar{1}\bar{1}]$ direction. Thus, the magnetisation decline in $[\bar{1}10]$ in combination with the sign change in $[110]$ marks the $ErFe_2$ reversal against the applied field.

8.6.2 Map of switching modes

We can now map the regimes of different switching modes on a T–n landscape (figure 8.14). In a nutshell, the regime of the independent switching mode is in the lower T half, the regime of the YFe_2 dominance mode in the high T high n corner, with the regime of the $ErFe_2$ spin flop mode stretching between the two. The regime of the coupled switching mode is located in the high T section of the low n edge. It is not an independent mode but rather an extension to either the

$ErFe_2$ spin flop mode or the YFe_2 dominance mode. We ignore the solitary $DyFe_2$ spin flop mode at 70 K for $n = 2$ nm believed to be an artifact.

The divide between the independent switching regime and $ErFe_2$ spin flop regime runs along a roughly vertical line with temperatures around 150 to 170 K for $n > 2$ nm. The increasing mutual RE exchange coupling for smaller YFe_2 separation assists the $ErFe_2$ moments in reversing via the spin flop mode, and the $ErFe_2$ spin flop regime stretches further out to 120 K for the smallest value of n, 2 nm.

The conditions for the YFe_2 dominance are a sufficiently high temperature in order to truncate the anisotropy barriers, and adequately thick YFe_2 layers to outweigh the RE compounds. Consistently, the regime is found in the high T high n corner, in a segment-like area delimited to $T = 220$ K for maximum n, and $n = 5$ nm for maximum T.

The regime where the $ErFe_2$ moments tend to couple to the $DyFe_2$ moments is located in the low n area where the magnetic separation barely impedes the mutual RE exchange coupling. It extends to a peak $n = 7$ nm between $T = 210$ K and $T = 360$ K. The decay of the Er anisotropy under a rising temperature facilitates the distortion of the $ErFe_2$ moments by exchange coupling with the $DyFe_2$ moments; this is reflected in the curved low T border of the coupled switching regime that extends further to $T = 160$ K for $n = 2$ nm, compared to $T = 210$ K for $n = 7$ nm.

Complementary details on switching processes are given in attachment B, traversing through the n/T parameter space by variations of T (figure B.1 on page 115), and by variations of n (figure B.2 on page 116).

8.7 Conclusion

Pre-strung exchange biased spring structures have potential for application in data storage media. Their complex magnetic behaviour opens up a rich tapestry of switching functionality. We have elucidated the switching modes for a specific system in which the exchange spring in the soft YFe_2 layer is pre-twisted by hard layers of $DyFe_2$ and $ErFe_2$ with competing anisotropy properties. Consequently, an exchange spring is present in this system even for zero applied field.

We have performed magnetic measurements of a [10nm $ErFe_2$/20nm YFe_2/4nm $DyFe_2$/20nm YFe_2] system, revealing the diversity of switching modes evident in the temperature dependent characteristics of the hysteresis loops. Micromagnetic simulations have reproduced the experimental results, giving insight into the detailed spin configurations. The simulation results were used to map the switching modes of a configurable system with a variable YFe_2 layer thickness. We have found an independent switching mode for low temperatures, an YFe_2 dominated switching mode for high temperatures and sufficiently thick YFe_2 layers, and an $ErFe_2$ spin flop mode for intermediate temperatures, or high temperatures

with little YFe_2 separation. In addition, we have discovered a coupled switching mode. This mode becomes manifest for small n values when the $DyFe_2$ and $ErFe_2$ moments mutually attract each other by exchange interaction that is transmitted through the sandwiched YFe_2 layers. The boundaries of the respective switching modes on the map of temperature and YFe_2 layer thickness have been explained by considerations of the relevant magnetic energies.

Understanding the manifold switching states present in this accurately reproducible and configurable exchange spring system provides the foundation for the design of next generation magnetic devices.

Chapter 9

Summary and outlook

9.1 Summary

Micromagnetic simulations play an important role in magnetic research, helping to interpret and understand experimental data and to optimise the design of novel devices. An improved knowledge of magnetic processes in nanostructures is the basis for the advent of new computer storage technologies and a diversity of applications in areas ranging from automobile industry to medical diagnostics.

We have investigated the magnetic properties of three representatives of a class of nanostructures known as magnetic exchange spring systems. Using micromagnetic simulations, we have reproduced the hysteresis loops that were obtained from measurements. With this justification, we have evaluated the spatially resolved spin configuration for the three systems considered.

Exchange spring systems owe their name to the magnetic configuration where the magnetisation of the soft magnetic layers winds into the direction of the applied field like a torsion spring. We have seen this switching behaviour in the studied systems for low temperatures. With increasing temperatures, we have observed a transition to different magnetic switching modes. The transition was attributed to the particular temperature dependence of the rare earth anisotropies and of the atomic magnetic moments in the compound materials.

For $DyFe_2/YFe_2$ multilayers, we have observed a remarkable reversal mode where the hard layers switch against the direction of the applied field. For the multilayers of $ErFe_2/YFe_2$, the 3D characteristics of the Er anisotropy cause a spin flop mode where the magnetisation points to a direction perpendicular to the applied field.

The magnetic switching behaviour of the two samples is governed by the energy barrier heights and positions of the Er and Dy anisotropy. The shape of the Er and Dy anisotropy energy in turn depends on the relative weight of the magnetocrystalline and strain anisotropy contributions, which shift with temperature. The predictive power of the numerical model validates the underlying anisotropy

energy constants on the basis of ab-initio calculations.

We have further studied a system of intertwined layers of $ErFe_2/YFe_2$ and $DyFe_2/YFe_2$. The differing anisotropy characteristics of the hard $ErFe_2$ and $DyFe_2$ compounds produce a pre-strung domain wall in the intermediate soft YFe_2 layers. The YFe_2 layer thickness represents a suitable control to adjust the magnetic tension between the hard layers and to regulate the mutual interference of the switching patterns of $ErFe_2$ and $DyFe_2$. We have fathomed the transition from individual to coupled switching modes for a range of temperatures and mapped the results as a prerequisite for future utilisation.

We overall conclude that our numerical model is a powerful and reliable instrument that helps accelerating progress in the field of rare earth based magnetic microstructures. Using the results of our micromagnetic simulations, experimenters can reduce the costly fabrication and evaluation cycles of specimens designed to provide specific magnetic properties.

We further conclude that exchange biased spring structures have potential for application particularly in data storage media. We have delivered a new set of building blocks in form of unique controllable magnetic switching modes, and hand over the baton to the electronic design engineers to assemble the building blocks into novel devices.

9.2 Outlook

In a continuation of this work, the following aspects would be highly interesting to study next:

- one assumption of our numerical model is the infinite exchange coupling of RE and Fe magnetic moments to an effective moment in a computational cell. The model could be enhanced to account for the magnetic moments of RE and Fe separately.
- the simulations have so far considered thermal effects by using the temperature-dependent magnetisation values and anisotropy energy constants. This could be improved by taking the thermal activation into account directly in form of the Langevin equation.
- the computational domain could be extended to cope with nucleation processes in the film plane.
- another challenge to tackle in future is the research into current induced spin-torque interaction. Under the influence of external currents, a supplementary torque acts on the spin configuration, which in turn affects the electric resistance.

We would require enhancements to the numerical model and the simulation code to face these issues. One approach might be the use of the alternative micromagnetic simulation code *nmag*. Nmag is currently developed by the Computational Nanomagnetism Group of Dr Fangohr at the University of Southampton. Based on the method of finite elements, it is devised for high flexibility and implements sophisticated micromagnetic algorithms. Some of the the required enhancements to the simulation code are projected to be readily available with nmag.

Appendix A

Material parameters

The magnetisation, magnetocrystalline anisotropy, and strain parameters for Dy, Er, Fe, and Y are taken from *Bowden* (2005), *Bowden et al.* (2006), *Martin et al.* (2006a). There, the values are obtained by first-principles calculations. Regarding the anisotropy values, an extension of the Callen-Callen model to second order was applied.

A.1 Magnetisation

The magnetisation M_{REFe2} of a compound is calculated with equation (6.1). As an input, we require the magnetic moments $m_{\mathrm{Fe}}(T)$, $m_{\mathrm{RE}}(T)$, $m_{\mathrm{Y}}(T)$ per formula unit (f.u.) for a given temperature. These values are obtained using

$$m(T) = m_0\, r_T(T), \tag{A.1}$$

where the temperature normalisation value $r_T(T)$ is looked up in tables A.1 and A.2, and the zero Kelvin magnetic moment m_0 is stated in table 6.1. The magnetic moment of Y is negligible.

A.2 Magnetocrystalline anisotropy

In tables A.1 and A.2, the values for $\tilde{A}_l$ (in K/f.u.) with $l \in \{4, 6, 8\}$ are stated. These parameters are required to calculate the phenomenological parameters K_1, K_2, K_3 by eq. (3.78) in section 3.3.4. The values $\tilde{K}_l$ are obtained by

$$\tilde{K}_l = 8\, k_{\mathrm{B}}\, \tilde{A}_l / V_{\mathrm{cell}}, \tag{A.2}$$

with the Boltzmann constant k_{B} and the lattice cell volume V_{cell} as stated in 6.2.1. The factor 8 reflects the number of RE atoms in a lattice cell. The magnetocrystalline anisotropy of Fe and Y are negligible.

A.3 Strain term

Similar to the considerations for the magnetocrystalline anisotropy, the magnetoelastic strain energy density $\varepsilon_{\mathrm{me}}$ as introduced in section 3.3.6 can be expressed by a decomposition with regard to the spherical harmonics Y_m^n (*Bowden et al.*, 2006). The values of the most relevant coefficients, $\tilde{K}_2'$ and $\tilde{K}_{242}''$, are obtained in units of J/m^3 by eq. A.2 with $l \in \{2, 242\}$ and $\tilde{A}_l$ (in K/f.u.) from tables A.1 and A.2. $\tilde{A}_{264}$ is stated for completeness. The strain terms of Fe and Y are negligible.

T [K]	$r_{T,\mathrm{Fe}}$ []	$r_{T,\mathrm{Er}}$ []	$\tilde{A}_4$ [K/f.u.]	$\tilde{A}_6$ [K/f.u.]	$\tilde{A}_8$ [K/f.u.]	$\tilde{A}_2$ [K/f.u.]	$\tilde{A}_{242}$ [K/f.u.]	$\tilde{A}_{264}$ [K/f.u.]
10	0.999103	0.999667	42.6036	-8.14857	4.29576	-1.40962	-0.321229	-0.0254644
20	0.997708	0.992963	41.0442	-7.62078	3.12186	-1.40922	-0.318772	-0.032212
30	0.996254	0.978949	36.0685	-6.04978	1.89705	-1.40475	-0.299256	-0.0343365
40	0.994729	0.961312	29.9688	-4.36759	1.11472	-1.39238	-0.270522	-0.0319587
50	0.993124	0.941848	24.2658	-3.02012	0.654709	-1.37225	-0.239666	-0.0277924
60	0.991426	0.921341	19.4392	-2.05313	0.386611	-1.34618	-0.210027	-0.0233198
70	0.989626	0.900169	15.5219	-1.39079	0.229846	-1.31593	-0.182968	-0.0191805
80	0.987712	0.878536	12.4007	-0.945569	0.13772	-1.28287	-0.158926	-0.0155982
90	0.985673	0.856568	9.93288	-0.647724	0.0832605	-1.24795	-0.137864	-0.0126059
100	0.983499	0.834367	7.98577	-0.447943	0.0508375	-1.21188	-0.119606	-0.0101565
110	0.981179	0.812023	6.44817	-0.313035	0.0313722	-1.17513	-0.103857	-0.00817503
120	0.978702	0.78963	5.23082	-0.221118	0.0195752	-1.13806	-0.0903133	-0.00658294
130	0.976057	0.767284	4.26352	-0.157861	0.0123523	-1.10092	-0.0786828	-0.00530825
140	0.973233	0.745078	3.49167	-0.113869	0.0078824	-1.06392	-0.0686976	-0.00428912
150	0.970219	0.723098	2.87295	-0.0829514	0.00508573	-1.0272	-0.0601195	-0.0034743
160	0.967005	0.701424	2.37462	-0.0609966	0.00331665	-0.990867	-0.0527411	-0.0028221
170	0.963579	0.680123	1.9713	-0.0452493	0.00218537	-0.955021	-0.0463835	-0.00229914
180	0.959931	0.659251	1.64331	-0.0338452	0.00145422	-0.919731	-0.0408942	-0.00187881
190	0.956049	0.63885	1.3753	-0.0255104	0.0	-0.885051	-0.0361435	-0.00154005
200	0.951924	0.618953	1.15527	-0.0193657	0.0	-0.851029	-0.0320218	-0.00126624
210	0.947544	0.599579	0.97382	-0.0147981	0.0	-0.817699	-0.0284364	-0.00104421
220	0.942898	0.580742	0.823524	-0.0113767	0.0	-0.78509	-0.0253091	0.0
230	0.937975	0.562446	0.698508	-0.00879506	0.0	-0.753224	-0.0225739	0.0
240	0.932764	0.544687	0.594098	-0.00683385	0.0	-0.722115	-0.0201752	0.0
250	0.927256	0.527459	0.506561	-0.00533448	0.0	-0.691776	-0.0180658	0.0
260	0.921438	0.510751	0.432902	-0.00418142	0.0	-0.662213	-0.0162059	0.0
270	0.915299	0.494547	0.370706	-0.00328981	0.0	-0.633428	-0.0145616	0.0
280	0.90883	0.478832	0.318016	-0.00259687	0.0	-0.605422	-0.0131043	0.0
290	0.902019	0.463586	0.273243	-0.00205582	0.0	-0.578192	-0.0118095	0.0
300	0.894855	0.44879	0.235088	-0.00163156	0.0	-0.551732	-0.0106562	0.0
310	0.887328	0.434424	0.202487	-0.00129758	0.0	-0.526034	-0.00962663	0.0
320	0.879426	0.420468	0.174561	-0.00103375	0.0	-0.501091	-0.00870545	0.0
330	0.871139	0.406901	0.150587	0.0	0.0	-0.476891	-0.00787948	0.0
340	0.862455	0.393703	0.129963	0.0	0.0	-0.453423	-0.00713734	0.0
350	0.853365	0.380856	0.112188	0.0	0.0	-0.430675	-0.00646922	0.0
360	0.843856	0.368339	0.0968425	0.0	0.0	-0.408634	-0.00586662	0.0
370	0.833919	0.356135	0.0835763	0.0	0.0	-0.387287	-0.00532216	0.0
380	0.823542	0.344225	0.0720932	0.0	0.0	-0.366622	-0.0048294	0.0
390	0.812714	0.332593	0.0621435	0.0	0.0	-0.346625	-0.00438273	0.0
400	0.801425	0.321222	0.0535157	0.0	0.0	-0.327283	-0.00397725	0.0

Table A.1: Parameter values for the magnetic moment, magnetocrystalline anisotropy, and strain term of $ErFe_2$ as a function of the temperature T.

T [K]	$r_{T,\mathrm{Fe}}$ []	$r_{T,\mathrm{Dy}}$ []	$\check{A}_4$ [K/f.u.]	$\check{A}_6$ [K/f.u.]	$\check{A}_8$ [K/f.u.]	$\check{A}_2$ [K/f.u.]	$\check{A}_{242}$ [K/f.u.]	$\check{A}_{264}$ [K/f.u.]
10	0.999103	0.999994	-64.46	-4.991	9.73415	6.35385	-0.88468	-0.0674954
20	0.997708	0.999085	-64.2228	-4.91386	9.20145	6.33655	-0.889326	-0.0737
30	0.996254	0.995003	-62.3579	-4.54491	7.62462	6.25923	-0.886601	-0.0858471
40	0.994729	0.987904	-58.5894	-3.94972	5.80686	6.12639	-0.864955	-0.0935648
50	0.993124	0.978796	-53.6975	-3.29716	4.24531	5.95897	-0.827931	-0.0950557
60	0.991426	0.9684	-48.401	-2.68749	3.04424	5.772	-0.781845	-0.0920265
70	0.989626	0.957146	-43.1502	-2.16016	2.16375	5.5746	-0.731504	-0.0863248
80	0.987712	0.945291	-38.1896	-1.7225	1.53272	5.37224	-0.680029	-0.0792854
90	0.985673	0.93299	-33.6354	-1.36769	1.08533	5.16834	-0.629336	-0.0717692
100	0.983499	0.920341	-29.5291	-1.08397	0.769622	4.96511	-0.580560	-0.0643007
110	0.981179	0.907406	-25.8703	-0.858871	0.547118	4.76403	-0.534338	-0.0571827
120	0.978702	0.894226	-22.6361	-0.68105	0.390174	4.56614	-0.490992	-0.050576
130	0.976057	0.880829	-19.7927	-0.540837	0.279242	4.37216	-0.450642	-0.044552
140	0.973233	0.867235	-17.302	-0.430309	0.200606	4.18265	-0.413283	-0.0391272
150	0.970219	0.853459	-15.1255	-0.343114	0.144673	3.998	-0.378828	-0.0342856
160	0.967005	0.839514	-13.2264	-0.274222	0.10474	3.81851	-0.347142	-0.0299924
170	0.963579	0.825414	-11.5707	-0.219684	0.07612	3.6444	-0.318065	-0.0262039
180	0.959931	0.811171	-10.1276	-0.176409	0.055526	3.4758	-0.291424	-0.0228726
190	0.956049	0.7968	-8.8697	-0.141986	0.0406484	3.31281	-0.267039	-0.0199511
200	0.951924	0.782316	-7.7728	-0.114534	0.0298581	3.15548	-0.244736	-0.0173939
210	0.947544	0.767733	-6.81575	-0.0925844	0.0220024	3.00381	-0.224346	-0.0151589
220	0.942898	0.753067	-5.98007	-0.0749879	0.0162619	2.85776	-0.205707	-0.0132072
230	0.937975	0.738335	-5.24975	-0.0608455	0.0120522	2.71726	-0.18867	-0.0115043
240	0.932764	0.723552	-4.6109	-0.0494511	0.00895462	2.58224	-0.173093	-0.010019
250	0.927256	0.708733	-4.05152	-0.0402489	0.00666815	2.45257	-0.158846	-0.00872392
260	0.921438	0.693891	-3.56123	-0.0328006	0.00497536	2.32813	-0.145812	-0.00759476
270	0.915299	0.679042	-3.13106	-0.0267592	0.00371865	2.20877	-0.13388	-0.00661029
280	0.90883	0.664196	-2.75328	-0.0218493	0.00278334	2.09433	-0.122952	-0.0057519
290	0.902019	0.649364	-2.42119	-0.0178519	0.00208565	1.98466	-0.112936	-0.00500337
300	0.894855	0.634557	-2.12901	-0.0145921	0.00156416	1.8796	-0.10375	-0.00435055
310	0.887328	0.619782	-1.87172	-0.01193	0.00117368	1.77896	-0.0953205	-0.0037811
320	0.879426	0.605046	-1.64499	-0.00975336	0.0	1.68259	-0.0875785	-0.00328433
330	0.871139	0.590357	-1.44507	-0.0079717	0.0	1.59032	-0.0804631	-0.00285091
340	0.862455	0.575717	-1.26867	-0.00651216	0.0	1.50199	-0.073919	-0.00247273
350	0.853365	0.561131	-1.11295	-0.00531576	0.0	1.41743	-0.0678959	-0.00214277
360	0.843856	0.546602	-0.975458	-0.00433468	0.0	1.33649	-0.0623486	-0.00185489
370	0.833919	0.532132	-0.854018	-0.00353004	0.0	1.25902	-0.0572361	-0.00160376
380	0.823542	0.517721	-0.746752	-0.00287018	0.0	1.18488	-0.0525211	-0.00138476
390	0.812714	0.50337	-0.652009	-0.00232925	0.0	1.11393	-0.0481703	-0.00119383
400	0.801425	0.489078	-0.568346	-0.00188608	0.0	1.04604	-0.0441531	-0.00102747

Table A.2: Parameter values for the magnetic moment, magnetocrystalline anisotropy, and strain term of $DyFe_2$ as a function of the temperature T.

Appendix B

Additional reversal diagrams for (10nm $ErFe_2/n$ YFe_2/4nm $DyFe_2/n$ YFe_2) samples

The [10nm $ErFe_2/n$ YFe_2/4nm $DyFe_2/n$ YFe_2] exchange spring systems have been discussed in chapter 8 already. Here, we list additional details on the reversal modes for a horizontal and a vertical cross section of the parameter space of the switching mode mapping. This is illustrates how small isolated changes of temperature (constant layer thickness, fig. B.1) or changes of layer thickness (constant temperature, fig. B.2) influence the switching behaviour.

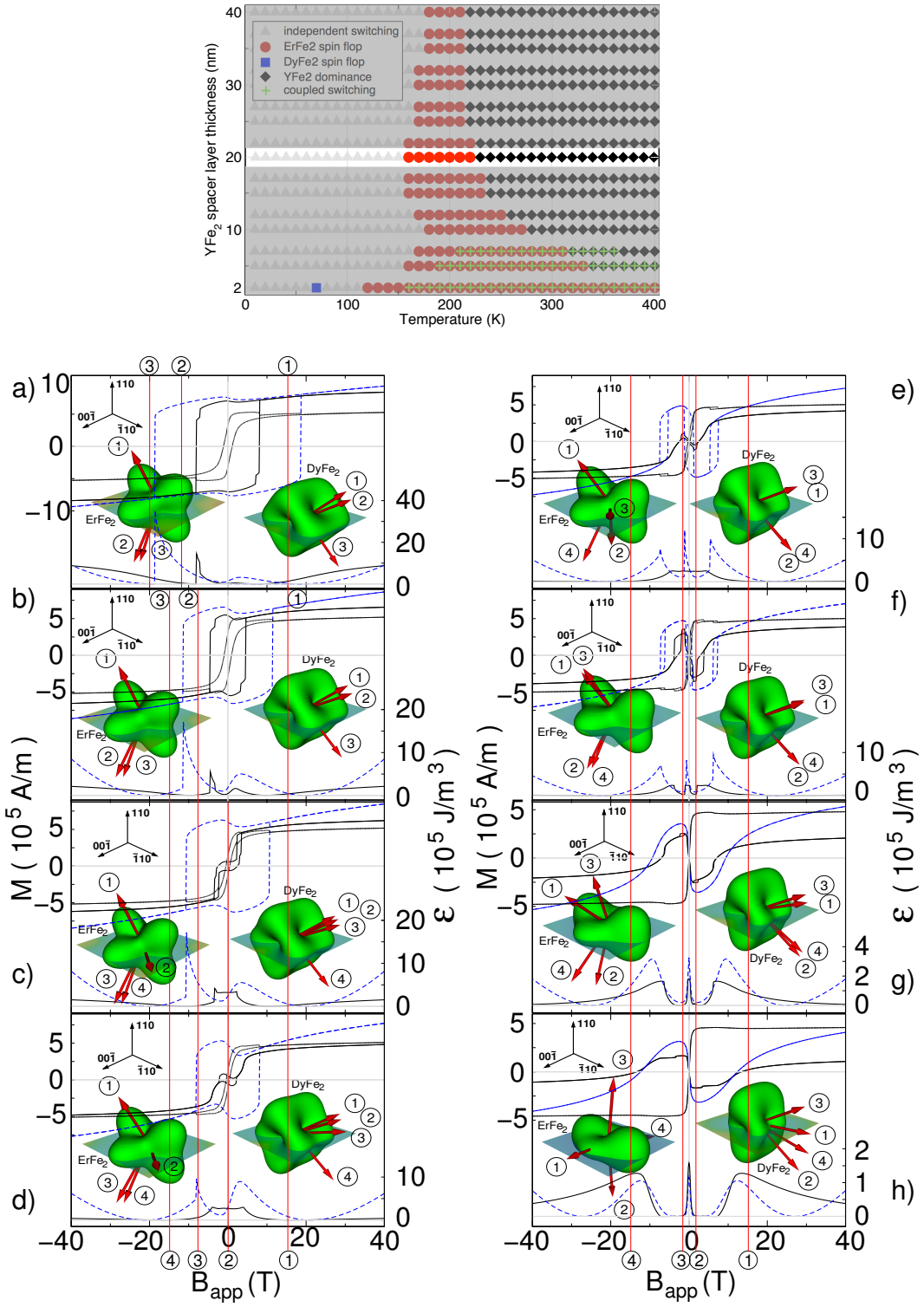

Figure B.1:]
Compound specific magnetisation curves and switching states for a set of different temperatures and an YFe_2 separation layer thickness 20 nm. The explanation of the graphs follows FIG. 8.7. The temperatures are 100 K (a) / 150 K (b) / 160 K (c) / 200 K (d) / 220 K (e) / 230 K (f) / 280 K (g) / 350 K (h). The parameter space is visualised by a horizontal slot on the switching mode mapping table in the first row.

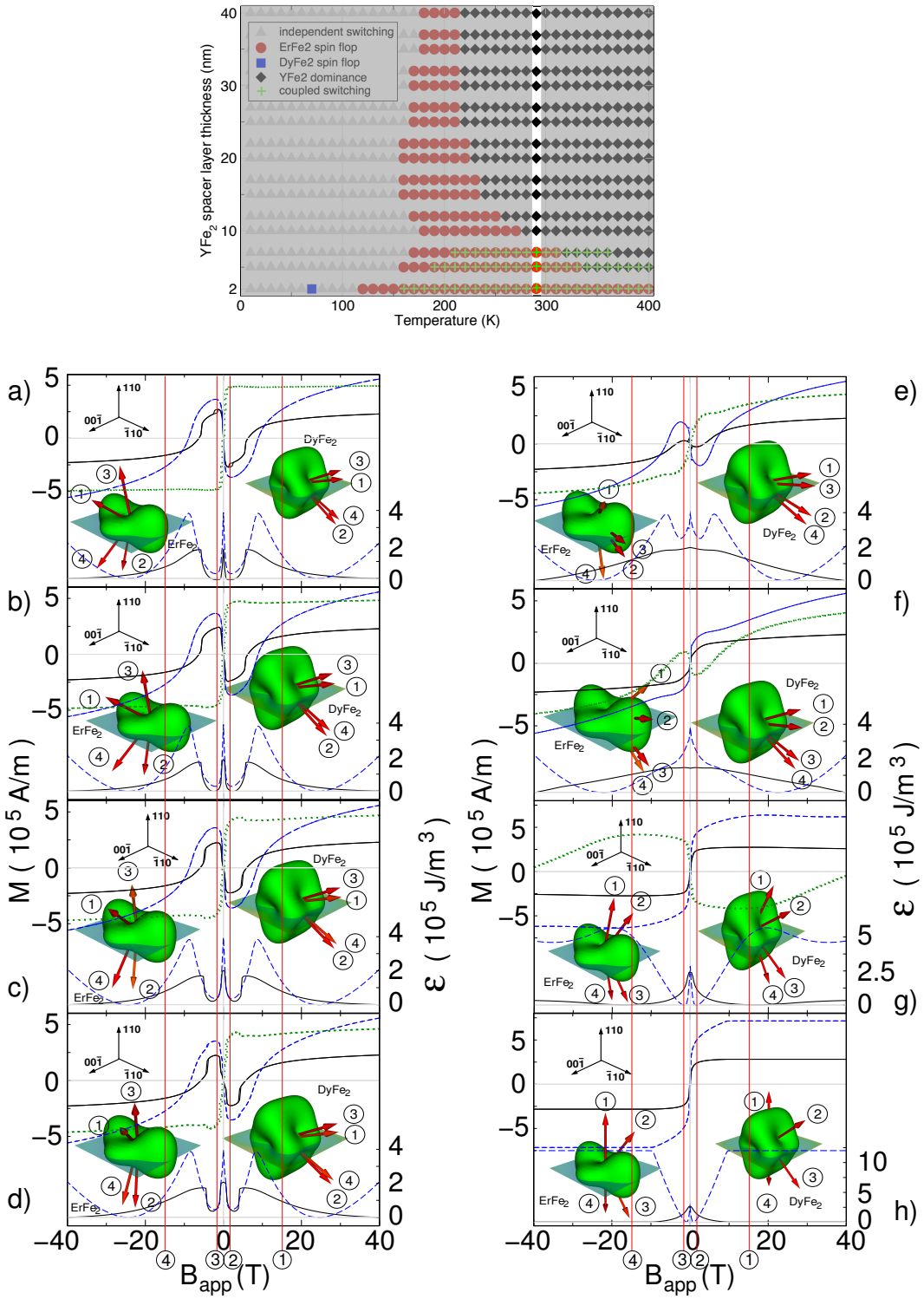

Figure B.2:]
Compound specific magnetisation curves and switching states for a set of different YFe_2 separation layer thicknesses and a temperature of 290 K. The explanation of the graphs follows FIG. 8.7. The separation layer thicknesses are 40 nm (a) / 20 nm (b) / 12 nm (c) / 10 nm (d) / 7 nm (e) / 5 nm (f) / 2 nm (g) / 0 nm (h). The parameter space is visualised by a vertical slot on the switching mode mapping in the first row. The 0 nm sample is not set on the map.

Bibliography

Aharoni A. Theoretical search for domain nucleation. *Review of Modern Physics*, **34**(2), 227–238 (1962).

Aharoni A. Demagnetizing factors for rectangular ferromagnetic prisms. *Journal of Applied Physics*, **83**(6), 3432–3434 (1998).

Aharoni A. *Introduction to the theory of Ferromagnetism*. Oxford Science Publications, 2nd edition (2000).

Albrecht M, Thiele JU and Moser A. Terabit-Speicher - bald Realität oder nur Fiktion? *Physik Journal*, **2**(10), 25–31 (2003).

Ando T and Nishihara T. Triple-layer perpendicular recording media for high SN ratio and signal stability. *IEEE Transactions on Magnetics*, **33**(5), 2983–2985 (1997).

Asti G, Ghidini M, Pellicelli R, Pernechele C, Solzi M, Albertini F, Casoli F, Fabbrici S and Pareti L. Magnetic phase diagram and demagnetization processes in perpendicular exchange-spring multilayers. *Physical Review B*, **73**, 094406 (2006).

Asti G, Solzi M, Ghidini M and Neri FM. Micromagnetic analysis of exchange-coupled hard-soft planar nanocomposites. *Physical Review B*, **69**, 174401 (2004).

Atzmony U and Dariel MP. Nonmajor cubic symmetry axes of easy magnetization in rare-earth iron laves compounds. *Physical Review B*, **13**(9), 4006–4014 (1976).

Baibich MN, Broto JM, Fert A, van Dau FN, Petroff F, Etienne P, Creuzet G, Friederich A and Chazelas J. Giant magnetoresistance of (001)Fe/(001)Cr magnetic superlattices. *Physical Review Letters*, **61**, 2472–2475 (1988).

Beaujour JML, Bowden GJ, Gordeev S, de Groot PAJ, Rainford BD, Ward RCC and Wells MR. Exchange springs in YFe_2 dominated $DyFe_2$–YFe_2 superlattices. *Journal of Magnetism and Magnetic Materials*, **226-230**, 1870–1872 (2001a).

Beaujour JML, Gordeev SN, Bowden GJ, de Groot PAJ, Rainford BD, Ward RCC and Wells MR. Negative coercivity in epitaxially grown (110) $DyFe_2/YFe_2$ superlattices. *Applied Physics Letters*, **78**(7), 964–966 (2001b).

Bentall MJ and R. C. C. Ward E. J. Grier MRW. Structure of $DyFe_2/YFe_2$ laves phase superlattices grown by molecular beam epitaxy. *Journal of Physics: Condensed Matter*, **15**, 6493–6512 (2003).

Binasch G, Grünberg P, Saurenbach F and Zinn W. Enhanced magnetoresistance in layered magnetic structures with antiferromagnetic interlayer exchange. *Physical Review B*, **39**(7), 4828–4830 (1989).

Binnig G and Rohrer H. Scanning Tunneling Microscopy. *Helvetica Physica Acta*, **55**, 726–735 (1982).

Binnig G and Rohrer H. Scanning tunneling microscopy - from birth to adolescence. *Reviews of Modern Physics*, **59**(3), 615–625 (1987).

Bleaney B, Bowden GJ, Cadogan JM, Day RK and Dunlop JB. A Mössbauer study of the cubic laves phase intermetallic compound $TmFe_2$. *Journal of Physics F: Metal Physics*, **12**(4), 795–811 (1982).

Blundell S. *Magnetism in Condensed Matter*. Oxford University Press, 1st edition (2001).

Bowden GJ. Private communication (2005).

Bowden GJ, Beaujour JML, Gordeev S, de Groot PAJ, Rainford BD and Sawicki M. Discrete exchange-springs in magnetic multilayer samples. *Journal of Physics: Condensed Matter*, **12**, 9335–9346 (2000).

Bowden GJ, Bunbury DSP, Giumaraes AP and Snyder RE. Mössbauer studies of the cubic laves iron-rare-earth intermetallic compounds. *Journal of Physics C*, **1**, 1376–1387 (1968).

Bowden GJ, de Groot PAJ, Rainford BD, Wang K, Martin KN, Zimmermann JP and Fangohr H. Magnetic anisotropy terms in [110] MBE grown $REFe_2$ films involving the strain term ε_{xy}. *Journal of Physics: Condensed Matter*, **18**, 5861–5871 (2006).

Bronstein IN and Semendjajew KA. *Taschenbuch der Mathematik*. Verlag Harri Deutsch, Thun (1989).

Brown Jr. WF. *Micromagnetics*. Wiley Interscience, New York (1963).

Buschow KHJ. Intermetallic compounds of rare-earth and 3d transition metals. *Reports on Progress in Physics*, **40**, 1179–1256 (1977).

Callen E and Callen HB. Magnetostriction, forced magnetostriction, and anomalous thermal expansion in ferromagnets. *Physical Review*, **139**(2A), A455–A471 (1965).

Callen HB and Callen E. The present status of the temperature dependence of magnetocrystalline anisotropy, and the l(l+1)/2 power law. *Journal of Physics and Chemistry of Solids*, **27**(8), 1271–1285 (1966).

Chabay R, Scherer D and Sherwood B. The visual module of vpython. http://vpython.org/webdoc/visual/index.html (2005).

Coehoorn R, de Mooij DB, Duchateau J and Buschow KHJ. Novel permanent magnetic materials made by rapid quenching. *Journal de Physique. Colloques*, **49**(8), 669–670 (1988).

Computational Engineering and Design Group, University of Southampton. Oxs Extension Module: CED_UniaxialAnisotropy. `http://math.nist.gov/oommf/contrib/oxsext/ced_soton/ced_uniaxialanisotropy.html` (2004).

Cugat O, Delamare J and Reyne G. Magnetic Micro–Actuators and Systems (MAGMAS). *IEEE Transactions on Magnetics*, **39**(5), 3607–3612 (2003).

Dehmelt H. Less is more: Experiments with an individual atomic particle at rest in free space. *American Journal of Physics*, **58**(1), 17–27 (1989).

Donahue M and Porter D. Object Oriented Micro-Magnetic Framework (OOMMF) (2003). `www.nist.gov`.

Donahue MJ and Porter DG. *OOMMF User's Guide*. National Institute of Standards and Technology, Gaithersburg, MD (1999). Interagency Report NISTIR 6376.

Donahue MJ and Porter DG. Exchange energy formulations for 3d micromagnetics. *Physica B*, **343**, 177–183 (2004).

Dumesnil K, Dufour C, Mangin P, Rogalev A and Wilhelm F. Temperature dependence in the magnetization reversal process of $DyFe_2/YFe_2$ exchange-coupled superlattices. *Journal of Physics: Condensed Matter*, **17**(21), L215–L222 (2005).

Dumesnil K, Dufour C, Mangin P, Wilhelm F and Rogalev A. Thermal dependence of magnetic springs location in a $DyFe_2/YFe_2$ superlattice. *Journal of Applied Physics*, **95**(11), 6843–6845 (2004).

Eigler DM and Schweizer EK. Positioning single atoms with a scanning tunnelling microscope. *Nature*, **344**, 524–526 (1990).

Feynman R. There's Plenty of Room at the Bottom. *Journal of Microelectromechanical Systems*, **1**(1), 60–66 (1992).

Fischer R, Leineweber T and Kronmüller H. Fundamental magnetization processes in nanoscaled composite permanent magnets. *Physical Review B*, **57**(17), 10723–0732 (1998).

Foner S. Vibrating Sample Magnetometer. *Review of Scientific Instruments*, **27**, 548 (1956).

Foner S. Versatile and Sensitive Vibrating-Sample Magnetometer. *Review of Scientific Instruments*, **30**(7), 548–557 (1959).

Fredkin DR and Koehler TR. Hybrid method for computing demagnetizing fields. *IEEE Transactions on Magnetics*, **26**, 415–417 (1990).

Fullerton EE, Jiang JS and Bader SD. Hard/soft magnetic heterostructures: model exchange-spring magnets. *Journal of Magnetism and Magnetic Materials*, **200**, 392–404 (1999).

Fullerton EE, Jiang JS, Grimsditch M, Sowers CH and Bader SD. Exchange-spring behaviour in epitaxial hard/soft magnetic bilayers. *Physical Review B*, **58**(18), 12193–12200 (1998).

Gibbs MRJ, Hill EW and Wright PJ. Magnetic materials for MEMS applications. *Journal of Physics D: Applied Physics*, **37**(5), R237–R244 (2004).

Gilbert TL. A Lagrangian formulation of gyromagnetic equation of the magnetization field. *Physical Review*, **100**, 1243 (1955).

Gordeev SN, Beaujour JML, Bowden GJ, de Groot PAJ, Rainford BD, Ward RCC and Wells MR. Spin configurations and negative coercivity in epitaxially grown $DyFe_2/YFe_2$ superlattices. *Journal of Applied Physics*, **89**(11), 6828–6830 (2001a).

Gordeev SN, Beaujour JML, Bowden GJ, de Groot PAJ, Rainford BD, Ward RCC, Wells MR and Jansen AGM. Giant magnetoresistance by exchange springs in $DyFe_2/YFe_2$ superlattices. *Physical Review Letters*, **87**(18), 186808.1–186808.4 (2001b).

Goto E, Hayashi N, Miyashita T and Nakagawa K. Magnetization and Switching Characteristics of Composite Thin Magnetic Films. *Journal of Applied Physics*, **36**(9), 2951–2958 (1965).

Haken H and Wolf HC. *Atom- und Quantenphysik*. Springer, 4th edition (1990).

Herring C. Direct exchange between well-separated atoms. *Magnetism*, **II b**, 1–181 (1963).

Hindmarsh AC and Petzold LR. Algorithms and software for ordinary differential equations and differential-algebraic equations, part ii: Higher-order methods and software-packages. *Computers in Physics*, **9**, 148–155 (1995).

Hubert A and Schäfer R. *Magnetic Domains*. Springer - Verlag Berlin Heidelberg (1998, 2000).

Iijima S. Helical microtubules of graphitic carbon. *Nature*, **354**, 56–58 (1991).

Jackson JD. *Classical Electrodynamics*. Wiley, 3rd edition (1999).

Kiselev SI, Sankey JC, Krivorotov IN, Emley NC, Schoelkopf RJ, Buhrman RA and Ralph DC. Microwave oscillations of a nanomagnet driven by a spin-polarized current. *Nature*, **425**, 380–383 (2003).

Kittel C. *Introduction to Solid State Physics*. John Wiley and Sons, Inc., 7th edition (1996).

Kneller EF and Hawig R. The exchange-spring magnet: a new material principle for permanent magnets. *IEEE Transactions on Magnetics*, **27**(4), 3588–3600 (1991).

Koltsov DK and Perry M. Magnets and nanometres: mutual attraction. *Physics World*, pages 31–35 (2004).

Kronmüller H and Fähnle M. *Micromagnetism and the Microstructure of Ferromagnetic Solids*. Cambridge University Press, 1st edition (2003).

Kroto HW, Heath JR, O'Brien SC, Curl RF and Smalley RE. C60: Buckminsterfullerene. *Nature*, **318**, 162–163 (1985).

Landau LD and Lifshitz EM. On the theory of the dispersion of magnetic permeability in ferromagnetic bodies. *Physikalische Zeitschrift der Sowjetunion*, **8**(2), 153–169 (1935).

Laves F. *Theory of Alloy Phases*. American Society for Metals, Cleveland, Ohio (1956).

Leineweber T and Kronmüller H. Micromagnetic examination of exchange coupled ferromagnetic nanolayers. *Journal of Magnetism and Magnetic Materials*, **176**, 145–154 (1997).

Long GJ and Grandjean F. *Supermagnets, Hard Magnetic Materials*. Kluwer Academic Publishers Dordrecht, 1st edition (1991).

Martin KN. Private communication (2007).

Martin KN, de Groot PAJ, Rainford BD, Wang K, Bowden GJ, Zimmermann JP and Fangohr H. Magnetic anisotropy in the cubic Laves $REFe_2$ intermetallic compounds. *Journal of Physics: Condensed Matter*, **18**, 459–478 (2006a).

Martin KN, Wang K, Bowden GJ, Zhukov AA, de Groot PAJ, Zimmermann JP, Fangohr H and Ward RCC. Exchange spring driven spin flop transition in erfe2/yfe2 multilayers. *Applied Physics Letters*, **89**, 132511 (2006b).

Mortimer CE. *Chemie*. Georg Thieme Verlag Stuttgart New York, 5th edition (1987).

Mougin A, Dufour C, Dumesnil K and Mangin P. Strain-induced magnetic anisotropy in single-crystal rFe$_2$(110) thin films (r=Dy, Er, Tb, Dy$_{0.7}$Tb$_{0.3}$, Sm, Y). *Physical Review B*, **62**(14), 9517–9531 (2000).

Newell AJ, Williams W and Dunlop DJ. A generalization of the demagnetizing tensor for nonuniform magnetization. *Journal of Geophysical Research*, **98**(17), 9551–9555 (1993).

Niarchos D. Magnetic MEMS: key issues and some applications. *Sensors and Actuators, A*, **109**, 166–173 (2003).

O'Handley RC. *Modern Magnetic Materials: Principles and Applications*. John Wiley and Sons, Inc. (1999).

Parkin SSP. Shiftable magnetic shift register and method of using the same (2004). United States Patent 6834005.

Python community. Python website (2007). `http://www.python.org`.

Ramachandran P. MayaVi: a free tool for CFD data visualisation. In *4th Annual CFD Symposium, Aeronautical Society of India* (2001).

Ridley PHW. *Finite element simulation of the micromagnetic behaviour of nanoelements*. Ph.D. thesis, School of Informatics, University of Wales, Bangor (2000).

Sabiryanov RF and Jaswal SS. Magnetic properties of hard/soft composites: SmCo$_5$/Co$_{1-x}$Fe$_x$. *Physical Review B*, **58**(18), 12071–12074 (1998).

Sawicki M, Bowden GJ, de Groot PAJ, Rainford BD, Beaujour JML, Ward RCC and Wells MR. Engineering coercivity in epitaxially grown (110) films of DyFe$_2$–YFe$_2$ superlattices. *Applied Physics Letters*, **77**(4), 573–575 (2000a).

Sawicki M, Bowden GJ, de Groot PAJ, Rainford BD, Beaujour JML, Ward RCC and Wells MR. Exchange springs in antiferromagnetically coupled DyFe$_2$–YFe$_2$ superlattices. *Physical Review B*, **62**(9), 5817–5820 (2000b).

Sawicki M, Bowden GJ, de Groot PAJ, Rainford BD, Ward RCC and Wells MR. Magnetic properties of epitaxial (110) multilayer films of DyFe$_2$ and YFe$_2$. *Journal of Applied Physics*, **87**(9), 6839–6841 (2000c).

Scholz W. *Scalable parallel micromagnetic solvers for magnetic nanostructures*. Ph.D. thesis, Fakultät für Naturwissenschaften und Informatik, Technische Universität Wien (2003).

Schroeder WJ, Martin KM and Lorensen WE. The design and implementation of an object-oriented toolkit for 3D graphics and visualization. In R Yagel and GM Nielson, editors, *IEEE Visualization '96*, pages 93–100 (1996).

SciPy community. SciPy website (2007). http://www.scipy.org/SciPy.

Skomski R and Coey JMD. Giant energy product in nanostructured two-phase magnets. *Physical Review B*, **48**(21), 15812–15816 (1993).

Spargo AW. *Finite element analysis of magnetisation reversal in granular thin films*. Ph.D. thesis, School of Informatics, University of Wales, Bangor (2002).

Stroscio JA and Celotta RJ. Controlling the Dynamics of a Single Atom in Lateral Atom Manipulation. *Science*, **306**, 242–247 (2004).

Suess D, Dahlgren M, Schrefl T, Grössinger R and Fidler J. Micromagnetic analysis of remanence and coercivity of nanocrystalline pr–fe–b magnets. *Journal of Applied Physics*, **87**(9), 6573–6575 (2000).

Suess D, Schrefl T, Dittrich R, Kirschner M, Dorfbauer F, Hrkac G and Fidler J. Exchange spring recording media for areal densities up to 10 Tbit/in^2. *IEEE Transactions on Magnetics*, **290-291**, 551–554 (2005a).

Suess D, Schrefl T, Fähler S, Kirschner M, Hrkac G, Dorfbauer F and Fidler J. Exchange spring media for perpendicular recording. *Applied Physics Letters*, **87**, 012504 (2005b).

Thiele JU, Maat S and Fullerton EE. Ferh/fept exchange spring films for thermally assisted magnetic recording media. *Applied Physics Letters*, **82**(17), 2859–2861 (2003).

Toshiba Corporation. Toshiba press release. http://www.toshiba.co.jp/about/press/2007_09/pr0601.htm (2007).

van Rossum G and Drake FL. *Python Reference Manual*. PythonLabs, Virginia, USA (2001).

Victora RH and Shen X. Exchange Coupled Composite Media for Perpendicular Magnetic Recording. *IEEE Transactions on Magnetics*, **41**(10), 2828–2833 (2005).

Xi H, Gao KZ and Shi Y. Spin-current induced high-frequency magnetisation rotations and microwave oscillations in magnetic nanodevices. *IEE Proceedings – Circuits, Devices and Systems*, **152**(4), 301–306 (2005).

Young R, Ward J and Scire F. The Topografiner: An Instrument for Measuring Surface Microtopography. *Review of Scientific Instruments*, **43**(7), 999–1011 (1972).

Zhang S, Levy PM and Fert A. Mechanisms of Spin–Polarized Current–Driven Magnetization Switching. *Physical Review Letters*, **88**(23), 236601 (2002).

Zhukov AA, Bowden GJ, Beaujour JML, Rainford BD, de Groot PAJ, Ward RCC, Wells MR and Küpfer H. Vector magnetometer studies of the easy magnetisation direction in epitaxially grown $DyFe_2$ film. *Journal of Magnetism and Magnetic Materials*, **270**, 312–320 (2004).

Zimmermann JP, Martin KN, Bordignon G, Boardman RP, Fischbacher T, Bowden GJ, Zhukov AA, Fangohr H and de Groot PAJ. Micromagnetic simulation of the magnetic exchange spring system $DyFe_2/YFe_2$. *Journal of Applied Physics*, **99**, 08B904 (2006).

Zimmermann JP, Martin KN, Bordignon G, Franchin M, Ward RCC, Bowden GJ, de Groot PAJ and Fangohr H. Magnetic switching modes for exchange spring systems $DyFe_2/YFe_2/ErFe_2/YFe_2$ with competing anisotropies: experiments and simulations . *Physical Review B* (2007). Submitted.